

基于烷基苯的慢液闪在中微子探测器原型机上的实验研究

(申请清华大学理学博士学位论文)

培养单位：工程物理系

学 科：物理学

研 究 生：郭子溢

指导教师：陈少敏教授

二〇二〇年五月

Experimental Studies on LAB-based Slow Liquid Scintillator Neutrino Detector Prototypes

Dissertation Submitted to
Tsinghua University
in partial fulfillment of the requirement
for the degree of
Doctor of Philosophy
in
Physics
by
Guo Ziyi

Dissertation Supervisor : Professor Chen Shaomin

May, 2020

关于学位论文使用授权的说明

本人完全了解清华大学有关保留、使用学位论文的规定，即：

清华大学拥有在著作权法规定范围内学位论文的使用权，其中包括：（1）已获学位的研究生必须按学校规定提交学位论文，学校可以采用影印、缩印或其他复制手段保存研究生上交的学位论文；（2）为教学和科研目的，学校可以将公开的学位论文作为资料在图书馆、资料室等场所供校内师生阅读，或在校园网上供校内师生浏览部分内容；（3）根据《中华人民共和国学位条例暂行实施办法》，向国家图书馆报送可以公开的学位论文。

本人保证遵守上述规定。

（保密的论文在解密后应遵守此规定）

作者签名： 郭子溢

日 期： 2020年7月21日

导师签名： 陈少敏

日 期： 2020年7月21日

摘要

中微子可以作为研究太阳与地球内部的独特探针，连接着粒子物理、地球物理、天体物理和宇宙学的若干中心问题。中国锦屏地下实验（CJPL）凭借其埋深世界最大和离商业核电站最远的优势，在研究诸如太阳、地球和超新星这些兆电子伏中微子方面，是具有国际竞争力的理想场所。对这些中微子的实验研究灵敏度依赖于对事例精确的能量、位置与方向的重建。然而，现有的液体闪烁体探测器却难以提供方向的重建信息，而可提供方向测量的水切伦科夫探测器又受限于较高的探测阈值与较差的能量分辨率。因此，研发可提供良好方向和能量测量的中微子探测器，对于未来兆电子伏中微子实验意义重大。针对上述实验需求，本论文对基于性线性烷基苯（LAB）这种具有慢荧光发光特性的液体闪烁体开展了预先研究。主要工作和创新点如下：

1. 在实验室搭建了一个 20 升小模型，测量了基于线性烷基苯的慢液闪的光产额和衰减时间。结果显示，在低浓度（LAB+0.07 g/L PPO+13 mg/L bis-MSB）下，光产额约为 4000 光子每 MeV 能量沉积，衰减时间约为 26 ns，为常规液闪的 3 至 4 倍，在保留一定的能量分辨率的同时还获得了对切伦科夫光和闪烁光的分辨能力，进而用于方向的重建。扫描了不同浓度的结果，对此进行了物理建模研究，给出的理论预言曲线与数据相符，为慢液闪技术在兆电子伏能区的应用提供了理论依据。

2. 基于高能物理分析软件包 ROOT 和 Geant4，开发了适用于慢液闪中微子实验的通用蒙特卡洛模拟和分析框架。在该框架中，探测器几何与靶物质构成的可扩展性强，便于对不同几何约束下的实验灵敏度进行定量估计；使用流式触发流程，便于模拟放射性本底、暗噪声等因素对实验的影响。这一框架目前在慢液闪探测器研发及锦屏中微子实验的预先研究中发挥着重要作用，已经应用在不同靶质量条件下探测器的效率修正、本底水平估计、重建算法等研究中。

3. 参与建造了一吨慢液闪原型机，利用该原型机进行了锦屏一期地下实验室宇宙线缪子通量的测量，结果为 $(3.53 \pm 0.22(\text{stat.}) \pm 0.07(\text{sys.})) \times 10^{-10} \text{ cm}^{-2}\text{s}^{-1}$ ，误差小于现有测量结果。分析了地下实验室全立体角的宇宙线缪子角分布，并利用卫星图像对山体地理构造进行了建模，发现了锦屏地下实验室宇宙线泄漏的主要方向，测量结果与模拟结果相符。同时也比较了山体屏蔽型实验与地下竖井型实验在宇宙线屏蔽方面的特点，该研究为地下中微子实验对宇宙线本底的主动与被屏蔽提供了设计依据。

关键词：中微子；液体闪烁体；模拟研究；切伦科夫光；宇宙线通量

Abstract

Neutrinos are unique probes to study the Sun and the Earth's interior, connecting several central issues of particle physics, geophysics, astrophysics, and cosmology. China JinPing underground Laboratory (CJPL) has distinct international competitive advantages by its deepest overburden in the world and the farthest from commercial nuclear power plants. These features let CJPL be ideal for studies of MeV-scale neutrinos, including solar-, geo-, and supernova neutrinos. Experimental sensitivity to these neutrinos depends on the precise reconstruction of the energy, position, and direction. However, the existing liquid scintillator detectors are challenging to provide directional reconstruction information. The water Čerenkov detectors that can provide directional measurements are limited by high detection threshold and poor energy resolution. Therefore, the development of neutrino detectors that can provide proper direction and energy measurements is of considerable significance to the future MeV-scale neutrino experiments. Given the above experimental requirements, this thesis carried out an R&D study on liquid scintillator based on linear alkyl-benzene (LAB) with slow fluorescence characteristics. The main contents of this thesis include:

A 20 L prototype was built to measure the scintillation light yield and decay time constant of LAB-based slow liquid scintillator. The results showed that at a low concentration (LAB+0.07 g/L PPO+13 mg/L bis-MSB), the light yield was 4000 photons/MeV and the decay time constant was 26 ns, 3 to 4 times that of the conventional liquid scintillator. Besides retaining a certain energy resolution, the ability to distinguish Čerenkov light and scintillation light was also obtained and then used to reconstruct the direction. Scanning various concentrations allowed a study of physical modeling. The prediction was consistent with the data, providing a theoretical basis for the slow liquid scintillator's application in the MeV-scale region.

Based on ROOT and Geant4, a general Monte Carlo simulation framework was developed for slow liquid scintillator neutrino experiments. In this framework, the detector geometry and the target material are highly expandable, convenient for the quantitative estimation of the experimental sensitivity under different geometric constraints. Using a streamed trigger algorithm facilitates the simulation of the impact of radioactive backgrounds and dark noise. This framework plays an essential role in the R&D study of the

Jinping Neutrino Experiment. It has been applied to the study of detector efficiency correction, background level estimation, and reconstruction algorithm under different target mass conditions.

A 1-ton prototype based on the slow liquid scintillator was constructed, providing a measurement of the cosmic-ray muon flux to be $(3.53 \pm 0.22(\text{stat.}) \pm 0.07(\text{sys.})) \times 10^{-10} \text{ cm}^{-2}\text{s}^{-1}$ at CJPL-I. The uncertainty is better than the published result. By reconstructing the angular distribution and utilizing satellite images to model the mountain terrain, the study identified the main direction of cosmic ray leakage at CJPL-I. The measurement results are consistent with the simulation results. Underground laboratories below mountains and down mine shafts were also compared in terms of cosmic-ray shielding. This study helps to design the active and passive shield of cosmic-ray background for the underground neutrino experiments.

Key Words: neutrino; liquid scintillator; simulation study; Čerenkov light; cosmic-ray flux

Contents

Chapter 1	Introduction	1
1.1	Neutrino properties	1
1.1.1	History	1
1.1.2	Neutrinos in the Standard Model	2
1.1.3	Neutrino oscillation.....	2
1.2	Open issues in MeV-scale neutrino physics	6
1.2.1	Dirac- or Majorana-type neutrinos.....	6
1.2.2	Neutrino mass and hierarchy	7
1.2.3	Sterile neutrinos	7
1.2.4	Solar neutrinos	7
1.2.5	Geo-neutrinos.....	8
1.2.6	Supernova neutrinos	9
1.3	The neutrino detection techniques	9
1.3.1	Water Čerenkov detector	9
1.3.2	Liquid scintillator detector	10
1.4	Low energy backgrounds in MeV-scale neutrino detection.....	11
1.5	China Jinping Underground Laboratory	12
1.6	Physics prospects of the MeV-scale neutrino experiment at CJPL	13
1.6.1	Jinping sensitivity for solar neutrinos	14
1.6.2	Jinping sensitivity for geo-neutrinos.....	18
1.6.3	Jinping sensitivity for supernova relic neutrinos.....	19
1.7	Slow liquid Scintillator	21
1.8	Organization of this thesis	25
Chapter 2	Studies of Slow Liquid Scintillator	26
2.1	The 20 L Detector.....	26
2.1.1	Detector layout.....	26
2.1.2	Detector simulation	28
2.1.3	Event selection.....	30
2.1.4	PMT gain calibration	31
2.2	Time profile measurement.....	32

2.3	Light yield measurement	35
2.4	Scanning of light yield and scintillation time.....	36
2.5	Emission spectrum	40
2.6	Optical transmission of acrylic	41
2.7	Attenuation length measurement.....	43
2.8	Performance evaluation for kiloton scale neutrino detector	45
2.9	Summary	46
Chapter 3 Development of Simulation Framework		48
3.1	Overview of simulation.....	49
3.2	Detector definition	50
3.2.1	Introduction of GDML	50
3.2.2	Detector hierarchy in JSAP	51
3.2.3	Materials	52
3.2.4	PMT	52
3.2.5	GDML parser	54
3.3	Physics processes	55
3.3.1	Optical processes	55
3.3.2	Neutron physics.....	56
3.4	Generator	56
3.5	Simulation and trigger process	59
3.5.1	Detector simulation.....	60
3.5.2	Electronics simulation	60
3.6	Output file format.....	63
3.7	Summary	64
Chapter 4 Design and Construction of the 1-ton Prototype		65
4.1	Detector structure	65
4.1.1	Structural design.....	65
4.1.2	Photomultiplier tube.....	67
4.1.3	Pure water circulation system.....	70
4.1.4	Nitrogen gas system	70
4.1.5	Slow control system	70
4.1.6	Installation process	72
4.2	Electronics trigger	73

4.2.1	Electronics boards	73
4.2.2	Trigger logic	75
4.2.3	Synchronization.....	76
4.3	Data acquisition system	82
4.3.1	Hardware system	82
4.3.2	Software system	82
4.3.3	Real-time event display	83
4.3.4	Readout file format	84
4.4	Summary	85
Chapter 5 Performance of the 1-ton Prototype Detector		87
5.1	Run status	87
5.2	PMT gain calibration	87
5.2.1	Parametrization of single photoelectron waveform	87
5.2.2	Peak search.....	91
5.2.3	PMT charge response model	92
5.2.4	RollingGain on the dark noise	95
5.2.5	RollingGain on the low energy events.....	103
5.3	Time calibration.....	105
5.3.1	First PE time distribution.....	107
5.3.2	Event selection.....	110
5.3.3	An example of calibration result	112
5.4	Vertex reconstruction	112
5.5	Energy scale calibration	114
5.6	Čerenkov light search.....	118
5.6.1	Analysis method	118
5.6.2	Statistical separation between lights	119
5.7	Summary	122
Chapter 6 Muon Flux Measurement at CJPL		123
6.1	Simulation of underground muon spectrum and spatial profile	123
6.1.1	Import the terrain data to Geant4	123
6.1.2	Muon generator	125
6.1.3	Simulation result.....	128
6.2	Detector simulation	128

Contents

6.2.1 Muon rate of a volume	128
6.2.2 Detector simulation	134
6.3 Event selection	136
6.4 Direction reconstruction	139
6.5 Flux and angular distribution result	141
6.5.1 Live time	141
6.5.2 Uncertainties	142
6.5.3 Muon flux measurement result.....	143
6.6 Summary	145
Chapter 7 Conclusions and Outlook	146
7.1 Conclusions	146
7.2 Outlook	147
Reference	149
Acknowledgments	155
Declaration	156
Resume, Publications and Research Achievements.....	157

Chapter 1 Introduction

In this chapter, we introduce neutrino properties and present unresolved issues in MeV-scale neutrino physics and neutrino detection techniques. Then we describe the China Jinping Underground Laboratory (CJPL) and the physics prospects of the Jinping Neutrino Experiment, including the detection of solar neutrinos, geo-neutrinos, and supernova neutrinos. Finally, we introduce our studies on the slow liquid scintillator based on linear alkyl-benzene (LAB).

1.1 Neutrino properties

1.1.1 History

In the 1910s, the nuclear beta decay experiments observed a continuous beta energy spectrum. However, at that time, the beta decay was assumed as a two-body process. The emitted beta (electron) energy should be monochromatic due to the law of energy conservation. The contradiction had been puzzling physicists for many years.

In 1930, Wolfgang Pauli hypothesized that an undetected neutral particle goes along with a recoiled nucleus and an electron in beta decay to ensure the energy, momentum, and angular momentum conservations. He called the particle as “neutron”, which means neutral particle. In 1932, James Chadwick discovered a massive neutral nuclear particle and also named it “neutron”. The name of “neutrino” was coined by Edoardo Amaldi during a conversation with Enrico Fermi to distinguish these two particle^[1]. Fermi later used the new name during a conference in Paris in July 1932, and the word “neutrino” entered the scientific vocabulary since then.

In 1956, Clyde Cowan and Frederick Reines confirmed Pauli’s hypothesis by the discovery of the electron anti-neutrinos produced in a nuclear reactor. The reaction process is that a neutrino interacts with a proton in the target material, it will go through an inverse beta decay (IBD) process



The positron produces a prompt signal, and the neutron is thermalized and then captured by hydrogen, emitting a delayed 2.2 MeV γ -ray signal. Nowadays, the detection method

based on the inverse beta decay reaction chain is still an import approach in neutrino experiments.

1.1.2 Neutrinos in the Standard Model

In the Standard Model, neutrinos are massless, left-handed neutral fermions. They interact with matter via the weak interaction only. There are three generations of neutrinos: ν_e, ν_μ, ν_τ , each corresponds to its charged lepton partner $e, \mu, \text{ or } \tau$, respectively. These three generations of neutrinos are also referred to as active neutrinos to distinguish from sterile neutrinos, which is a hypothesis based on recent anomalies observed in the short base-line neutrino experiments and the latest astrophysical data^[2-4].

The weak interaction is mediated by three vector bosons: W^\pm and Z^0 . In the context of current-current interaction, the W^\pm boson mediates the charged current (CC), while Z^0 mediates the neutral current (NC). For example,

$$\text{CC: } \bar{\nu}_e + p \rightarrow n + e^+ \quad (1-2)$$

$$\text{NC: } \nu_\mu + e^- \rightarrow \nu_\mu + e^- \quad (1-3)$$

1.1.3 Neutrino oscillation

Theoretically, neutrinos can not interchange among the three generations or flavors. However, if neutrinos have mass, their identities can vary when they travel, leading to an oscillation from one to another. The neutrino oscillation is evidence of existing physics beyond the Standard Model. Understanding this phenomenon plays an essential role in modern neutrino physics study.

1.1.3.1 Vacuum oscillation

In the three-generation mixing framework, neutrino oscillation indicates that the neutrino mass eigenstates ν_1, ν_2, ν_3 should not be flavor eigenstates ν_e, ν_μ, ν_τ . Neutrinos are generated via the weak interaction in the flavor eigenstates and propagate in the mass eigenstates. In quantum mechanics, each flavor eigenstate can be written as a superposi-

tion of mass eigenstates,

$$\begin{pmatrix} \nu_e \\ \nu_\mu \\ \nu_\tau \end{pmatrix} = \begin{pmatrix} U_{e1} & U_{e2} & U_{e3} \\ U_{\mu1} & U_{\mu2} & U_{\mu3} \\ U_{\tau1} & U_{\tau2} & U_{\tau3} \end{pmatrix} \begin{pmatrix} \nu_1 \\ \nu_2 \\ \nu_3 \end{pmatrix} \quad (1-4)$$

The transformation matrix U is called the PMNS (Pontecorvo–Maki–Nakagawa–Sakata) matrix or neutrino mixing matrix, which can be described by three mixing angles ($\theta_{12}, \theta_{23}, \theta_{13}$), one CP phase angle δ , and two Majorana phase angles ϕ_1, ϕ_2

$$U = \begin{pmatrix} 1 & 0 & 0 \\ 0 & c_{23} & s_{23} \\ 0 & -s_{23} & c_{23} \end{pmatrix} \times \begin{pmatrix} c_{13} & 0 & s_{13}e^{-i\delta} \\ 0 & 1 & 0 \\ -s_{13}e^{i\delta} & 0 & c_{13} \end{pmatrix} \times \begin{pmatrix} c_{12} & s_{12} & 0 \\ -s_{12} & c_{12} & 0 \\ 0 & 0 & 1 \end{pmatrix} \times \begin{pmatrix} e^{i\phi_1} & 0 & 0 \\ 0 & e^{i\phi_2} & 0 \\ 0 & 0 & 1 \end{pmatrix} \quad (1-5)$$

where s_{ij} and c_{ij} are used to denote $\sin \theta_{ij}$ and $\cos \theta_{ij}$, respectively. Majorana phase angles cannot be observed in neutrino oscillation experiments. The present mixing angles are^[5]

$$\begin{aligned} \sin^2 \theta_{12} &= 0.307_{-0.012}^{+0.013} & \theta_{12} &= 33.6^\circ \\ \sin^2 \theta_{23} &= 0.417_{-0.028}^{+0.025} & \theta_{23} &= 40.2^\circ \\ \sin^2 \theta_{13} &= 0.0212 \pm 0.0008 & \theta_{13} &= 8.37^\circ \end{aligned} \quad (1-6)$$

After a propagation of time T at a distance L in vacuum, an arbitrary neutrino state with a flavor α can be described by a plane wave,

$$|\nu_\alpha(L, T)\rangle = \exp(-i\hat{E}t + i\hat{p}L) |\nu_\alpha\rangle \quad (1-7)$$

where \hat{E} and \hat{p} are the energy and momentum operators, respectively. For ultrarelativistic neutrinos in mass eigenstates $|\nu_i\rangle$, we have an approximation,

$$Et - pL = \left(E - \sqrt{E^2 - m_i^2} \right) L \approx \frac{m_i^2}{2E} L \quad (1-8)$$

The probability of an initial state $|\nu_\alpha\rangle$ oscillating to $|\nu_\beta\rangle$ can be written as

$$P(\nu_\alpha \rightarrow \nu_\beta) = |\langle \nu_\beta | \nu_\alpha(L, T) \rangle|^2 = \sum_i \sum_j U_{\beta j}^* U_{\alpha j} U_{\beta i} U_{\alpha i}^* e^{-i\Delta m_{ij}^2 L/2E} \quad (1-9)$$

where E is the neutrino energy, L is the neutrino propagation length (baseline), $\Delta m_{ij}^2 = m_i^2 - m_j^2$ is the squared difference of neutrino mass eigenvalues. In the situation of $\nu_\alpha = \nu_\beta = \nu_e$, $P(\nu_e \rightarrow \nu_e)$ is the survival probability of electron neutrino and can be simplified

as^[6]

$$\begin{aligned}
 P(\nu_e \rightarrow \nu_e) = & 1 - \sin^2 2\theta_{13} \left[\cos^2 \theta_{12} \sin^2 \left(\frac{\Delta m_{31}^2 L}{4E} \right) + \sin^2 \theta_{12} \sin^2 \left(\frac{\Delta m_{32}^2 L}{4E} \right) \right] \\
 & - \sin^2 2\theta_{12} \cos^4 \theta_{13} \sin^2 \left(\frac{\Delta m_{21}^2 L}{4E} \right)
 \end{aligned} \tag{1-10}$$

Given the fact that $\Delta m_{31}^2 \gg \Delta m_{21}^2$, $\Delta m_{31}^2 \approx \Delta m_{32}^2$, the survival probability Eq. (1-10) can be further simplified for neutrinos with energy $E \sim 1$ MeV and a baseline $L \sim 1$ km,

$$P(\nu_e \rightarrow \nu_e) \approx 1 - \sin^2 2\theta_{13} \sin^2 \left(\frac{\Delta m_{31}^2 L}{4E} \right) - \sin^2 2\theta_{12} \cos^4 \theta_{13} \sin^2 \left(\frac{\Delta m_{21}^2 L}{4E} \right) \tag{1-11}$$

Similarly, the probability for electron neutrino appearance in a muon neutrino beam with energy $E \sim 1$ GeV and a baseline $L \sim 100$ km is dominated by^[7]

$$P(\nu_\mu \rightarrow \nu_e) \approx \sin^2 \theta_{23} \sin^2 2\theta_{13} \sin^2 \left(\frac{\Delta m_{32}^2 L}{4E} \right) \tag{1-12}$$

Solar neutrino experiments and medium baseline reactor neutrino experiments can measure the neutrino mixing angle θ_{12} , atmosphere neutrino experiments, and long-baseline accelerator neutrino experiments can measure θ_{23} , while short-baseline reactor neutrino experiments and long-baseline accelerator neutrino experiments can measure θ_{13} .

1.1.3.2 Matter effect

The MSW (Mikheyev–Smirnov–Wolfenstein) effect, or matter effect, acts to modify neutrino oscillations in matter^[8-9]. Although the interaction between neutrinos and the propagating medium is weak, the neutrino oscillation pattern may change when the neutrino energy or the electron density of the medium is high, for example, in the core of the Sun. In this case, the Hamiltonian of the neutrino system in matter H_m can be written as the sum of the Hamiltonian in vacuum H_0 and interaction term H_{int} ,

$$H_m = H_0 + H_{\text{int}} \tag{1-13}$$

with

$$H_0 |\nu_i\rangle = E |\nu_i\rangle, \quad E = \sqrt{p^2 + m_i^2}, \quad i = 1, 2, 3 \tag{1-14}$$

$$H_{\text{int}} |\nu_\alpha\rangle = V_\alpha |\nu_\alpha\rangle \tag{1-15}$$

where E is the neutrino energy, p is the neutrino momentum, V_α is the effective potential felt by the active flavor neutrino ν_α , $\alpha = e, \mu, \tau$. Figure 1.1 shows the Feynman diagrams of coherent forward elastic scattering processes in matter.

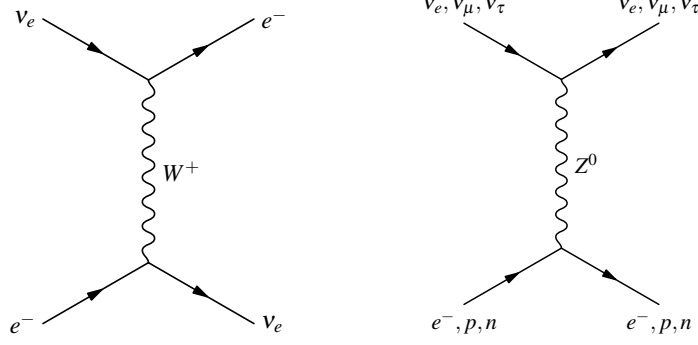


Figure 1.1 Feynman diagrams of the coherent forward elastic scattering processes that generate the CC potential V_{CC} through W exchange (left) and the NC potential V_{NC} through Z exchange (right).

We can write the potential as the sum of CC potential V_{CC} and NC potential V_{NC} ^[10],

$$V_\alpha = V_{CC}\delta_{\alpha e} + V_{NC} \quad (1-16)$$

$$V_{CC} = \sqrt{2}G_F n_e, \quad V_{NC} = -\frac{\sqrt{2}}{2}G_F n_n \quad (1-17)$$

where G_F is the Fermi coupling constant, n_e and n_n are the electron and neutron number densities, respectively. The CC potential V_{CC} is felt only by the electron neutrino. Since the NC potentials due to scattering on electrons and protons are equal and with opposite signs, they cancel each other. Only the NC potential due to scattering on neutrons contributes to V_{NC} .

The Hamiltonian in Eq. (1-13) can be written in matrix form as

$$H_m = \frac{1}{2E} (UMU^\dagger + A) \quad (1-18)$$

where

$$M = \begin{pmatrix} m_1^2 & 0 & 0 \\ 0 & m_2^2 & 0 \\ 0 & 0 & m_3^2 \end{pmatrix}, \quad A = \begin{pmatrix} A_{CC} + A_{NC} & 0 & 0 \\ 0 & A_{NC} & 0 \\ 0 & 0 & A_{NC} \end{pmatrix} \quad (1-19)$$

$$A_{CC} = 2EV_{CC} = 2\sqrt{2}EG_F n_e \quad (1-20)$$

$$A_{\text{NC}} = 2EV_{\text{NC}} = -\sqrt{2}EG_F n_n \quad (1-21)$$

Eq. (1-18) can be diagonalized,

$$H_m = \frac{1}{2E}U_m \tilde{M} U_m^\dagger \quad (1-22)$$

U_m can be parametrized like Eq. (1-5). We can define the effective neutrino mix angle in matter θ_m ,

$$\sin 2\theta_m = \frac{\tan 2\theta}{\sqrt{(1 - n_e/n_e^R)^2 + \tan^2 2\theta}} \quad (1-23)$$

where n_e is the electron density, n_e^R is the resonance density^[8],

$$n_e^R = \frac{\Delta m^2 \cos 2\theta}{2\sqrt{2}EG_F} \quad (1-24)$$

1.2 Open issues in MeV-scale neutrino physics

The neutrino energy of natural or artificial sources is from sub-MeV to hundreds of GeV. There are many open issues in MeV-scale neutrino physics, i.e., neutrino energy below a few tens of MeV. Neutrinos can also act as unique probes for studying the Sun, the Earth, and the supernovae's interior due to their extremely rare interactions with matter. Unlike optical photons, gammas, protons, or other particles, neutrinos can easily reach the detector without being interrupted by the matter along their path. The origin status, including energy and direction, is therefore maintained. We can access the primary information as long as we take into account the neutrino oscillation effect. This feature opens a new era of multi-messenger astrophysics and geophysics.

1.2.1 Dirac- or Majorana-type neutrinos

In the Standard Model, neutrinos are assumed to obey the Dirac equation, but we do not have any experimental evidence. Like a neutral boson, as the gamma or the Z^0 , completely neutral fermions do not have any charge or lepton number. These fermions are described by the Majorana equation, rather than the Dirac equation. We have no idea whether neutrinos are Dirac- or Majorana-type particles. One way to test the Majorana nature of neutrino is to search for $0\nu\beta\beta$ decay events, which is the double-beta decay without the emission of neutrinos.

1.2.2 Neutrino mass and hierarchy

Although neutrino oscillations indicate non-zero neutrino mass, the absolute value of neutrino mass remains unknown so far. Cosmological observations are sensitive to the sum of neutrino masses,

$$\Sigma = m_1 + m_2 + m_3 \quad (1-25)$$

Neutrinoless double beta decay ($0\nu\beta\beta$) experiments are sensitive to the square of the effective Majorana mass,

$$m_{\beta\beta} = \left| \sum_i U_{ei}^2 m_i \right| \quad (1-26)$$

where U_{ei} is the matrix element of the neutrino mixing matrix. These two types of observations provide an indirect and model-dependent access to the absolute neutrino mass scale, whereas the measurements of low-energy beta decay spectra are the most direct approach^[11], giving the upper limit of the effective neutrino mass m_β ,

$$m_\beta = \sqrt{\sum_i |U_{ei}|^2 m_i^2} \quad (1-27)$$

as low as ~ 1 eV level^[12].

In addition to neutrino mass, the mass order of three-generation neutrinos are still unknown. The normal hierarchy $m_1 < m_2 < m_3$ and the inverted hierarchy $m_3 < m_1 < m_2$ need to be tested. The present global fit using neutrino oscillation data indicates normal hierarchy. Further observation is expected from JUNO^[13], T2K^[14], and DUNE^[15].

1.2.3 Sterile neutrinos

There are some experimental hints for the hypothesis of sterile neutrinos^[2-4] besides the three generations of neutrinos. Sterile neutrinos do not react via the weak interaction. The three generations of neutrinos may oscillate to sterile neutrinos.

1.2.4 Solar neutrinos

The Sun and other stars have similar life cycles. The study of solar neutrinos can test the Standard Solar Model (SSM) and models of stellar evolution and neutrino oscillation. The discrepancy was first observed in the mid-1960s and finally resolved by

the SNO's measurement around 2002. There are still some open issues about the solar neutrino properties and SSM^[16], including but not limited to:

Some components of solar neutrinos, for example, the CNO cycle neutrinos with energy around a few MeVs, have not been observed yet. The flux of the CNO cycle neutrinos is relatively small, while the background in this energy range is relatively high. The constraint on the solar model can be tighter with the help of more precise measurements of all the solar neutrino components.

The metallicity problem. In astronomy, metallicity is defined as the abundance of elements that are heavier than hydrogen and helium. An improved solar model AGS09 gives a 30% lower photospheric abundance of metals than the earlier model GS98^[17-18]. Several neutrino components have lower fluxes in the low metallicity assumption than the prediction based on the high metallicity assumption. A precise measurement of the flux of these components, especially the flux of CNO neutrinos due to the direct dependence on the metal abundance^[19], plays a key role in solving the metallicity problem.

The full picture of the MSW effect in the solar electron neutrino oscillation has not been completed. The measurement of the MSW effect in the solar electron neutrino oscillation has an incomplete transition region, especially from 1 to 5 MeV. For low-energy (< 1 MeV) solar electron neutrinos, the MSW effect is not significant, and the oscillation occurs like in vacuum. The MSW effect becomes dominant as the neutrino energy increases because the electron density of the Sun's interior is very high, and the oscillation of electron neutrinos will eventually reach a maximum. However, current experiments poorly constrain the transition region from vacuum to matter^[20-23]. Studies show that the oscillation behavior in the transition region is also sensitive to physics beyond the Standard Model, e.g. sterile neutrino or non-standard interactions.

1.2.5 Geo-neutrinos

Geo-neutrinos are produced by radioactive decays in the Earth's interior, from the crust to the mantle. The measurement of geo-neutrino flux and energy spectrum can help us understand the dynamics inside the Earth. In geology, the geo-energy budget is one of the fundamental questions. Currently, the total heat flow of is estimated to be (47 ± 2) TW^[24]. One of which comes from the decay of radiogenic isotopes (mainly K, Th, and U, >99%^[25]). Three models estimate the radiogenic heat production by the previous cosmochemical, geochemical and geodynamical study^[25]: low Q (10~15 TW of power),

medium Q (17 ~ 22 TW), and high Q (>25 TW).

Only the neutrinos from ^{232}Th and ^{238}U decay chains are detectable via the inverse beta decay reaction chain because of the 1.8 MeV threshold. Measurements of these geo-neutrinos will place limits on the radiogenic power models. Thanks to the development of large underground neutrino detectors KamLAND and Borexino, neutrino geophysics became practical. Existing measurements of geo-neutrinos^[26-27] reveal the total amount of uranium and thorium in the Earth. However, the ratio between the two elements has not been measured due to the substantial reactor neutrino background and low statistics of signal. The present precision is also far from sufficient to test the models.

1.2.6 Supernova neutrinos

Supernova neutrinos include burst and relic ones with energy below a few tens of MeV. The event of SN1987a-like supernova burst neutrinos is rare, at a rate of 1-3 per century. Supernova relic neutrinos (SRNs), also known as the Diffuse Supernova Neutrino Background (DSNB), are accumulated neutrinos emitted from past core-collapse supernovae and form a continuum background. These neutrinos can play critical ingredients in understanding the stellar evolution in the universe. Although some searches have been carried out by Super-Kamiokande^[28-30], KamLAND^[31], Borexino^[32], and SNO^[33], no SRN signal has been found yet.

1.3 The neutrino detection techniques

The MeV-scale neutrino experiments mainly consist of two types of detectors: water Čerenkov and liquid scintillator detectors with target mass from hundreds to thousands of tons. Other techniques, such as time projection chamber (TPC) used in GeV-scale accelerator neutrino experiments, will not be discussed in this thesis.

1.3.1 Water Čerenkov detector

Super-Kamiokande and SNO are representative of water (or heavy water) Čerenkov detectors. When a charged particle passes moves faster than the speed of light in medium, Čerenkov radiation emits photons along the path with a light cone angle θ_C ,

$$\cos \theta_C = \frac{1}{n(\lambda)\beta} \quad (1-28)$$

where $n(\lambda)$ is the refractive index of the medium, as a function of wavelength λ , $\beta = v/c$ is the relativistic speed of the charged particle. When $\beta \rightarrow 1$, the Čerenkov angle reaches its maximum $\theta_{\max} = \arccos(1/n)$. The energy thresholds for different particles in water ($n = 1.33$, $\theta_{\max} = 41.2^\circ$) and liquid scintillator ($n = 1.5$, $\theta_{\max} = 48.2^\circ$) is listed in Table 1.1.

Table 1.1 The energy thresholds for different particles in water and liquid scintillator.

Particle	Mass /MeV	Water /MeV	LS /MeV
Electron	0.511	0.775	0.686
Muon	106	161	142
Proton	938	1422	1258

The number of Čerenkov photons N radiated with energies in the interval dE by a particle of charge z in track length dx is given by

$$\frac{d^2 N}{dE dx} = \frac{\alpha z^2}{\hbar c} \left(1 - \frac{1}{\beta^2 n^2} \right) \quad (1-29)$$

or

$$\frac{d^2 N}{d\lambda dx} = \frac{2\pi\alpha z^2}{\lambda^2} \left(1 - \frac{1}{\beta^2 n^2} \right) \quad (1-30)$$

where α is the fine structure constant, λ is the wavelength of Čerenkov photons. Integrating λ over 400 nm to 700 nm (the detectable wavelength range), we get the Čerenkov light yield N for an electron with path-length L ,

$$\frac{N}{L} \approx 490 \sin \theta \text{ photons/cm} \quad (1-31)$$

In the case of $n = 1.5$, $\beta = 1$, $dE/dx = 2 \text{ MeV/cm}$, the Čerenkov light yield can be estimated to 180 photons/MeV. The shorter path-length, the less light yield. The Čerenkov light cone can be used to reconstruct the direction of a charged particle. It is expected that insufficient Čerenkov photons will significantly affect the energy resolution for the study of neutrinos with energy about a few of MeVs.

1.3.2 Liquid scintillator detector

Organic liquid scintillators (LS) have been applied for detecting MeV-scale neutrinos in KamLAND, Borexino, and Dayabay experiments. A liquid scintillator is actually a “cocktail” containing a solvent and small amounts of other additive fluors and wavelength

shifters. Charged particles transfer kinetic energy to the solvent molecules. The captured energy is transferred between solvent and fluor molecules. The wavelength shifter absorbs the energy of the fluor and re-emits light at a longer wavelength. The typical light yield for a conventional LS is $\sim 10^4$ photons/MeV. The emitted scintillation photons are isotropic and much more intensive than the Čerenkov photons. As a consequence, the later becomes indistinguishable and loses the directional information in the light measurement. It is noted that unlike LAB, some organic LS may have potential environmental problems^[34].

1.4 Low energy backgrounds in MeV-scale neutrino detection

The event rate of MeV-scale neutrino is quite low. The neutrino spectrum unfolding and flux measurement are even tricky under the influence of intrinsic radioactive backgrounds and cosmic-ray muon induced backgrounds in the laboratory or detector material. The purification of detector material is a key procedure for low background neutrino experiments. It is noted that the background above 6 MeV mainly comes from the cosmic-ray spallation background, while below is from detector material and cosmogenic background.

Figure 1.2 shows the fit of the energy spectrum in Borexino^[35]. Cosmogenic ^{11}C background is produced when a cosmic muon interacts with ^{12}C ,



^{11}C decays to $^{11}_5\text{B}$ via β^+ decay,



The Q -value is 0.96 MeV, and the visible energy of the positron is 1.02 \sim 1.98 MeV. It is not easy to distinguish this positron signal and CNO neutrino signal. Suppression of this background strongly relies on the effective cosmic-ray shielding, i.e. the depth of overburden.

Reactor neutrinos are signals in many neutrino oscillation experiments. While for geo-neutrinos, those from reactors are the main background. The detector should be far away from any reactor to suppress this background.

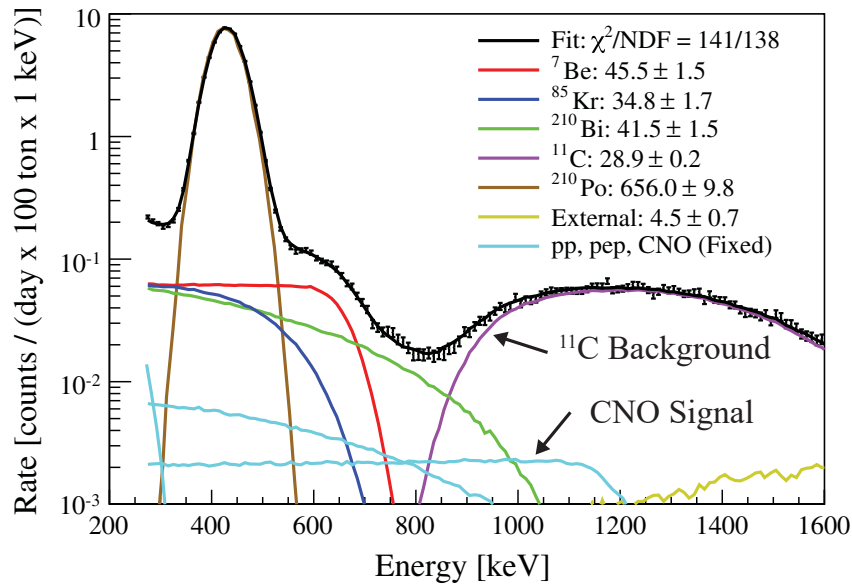


Figure 1.2 Fit of the energy spectrum in Borexino, including solar neutrino components and radioactive backgrounds.

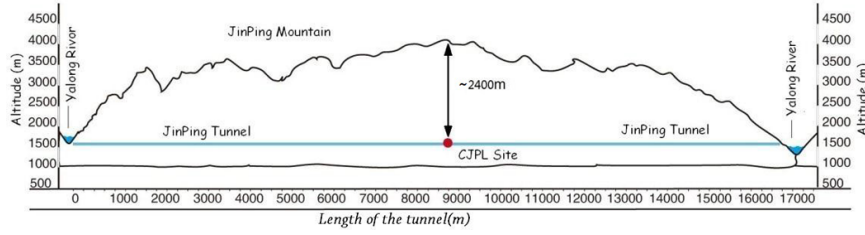
1.5 China Jinping Underground Laboratory

The China Jinping Underground Laboratory (CJPL)^[36], located in Sichuan province, China, is one of the ideal sites for low background experiments. The location of CJPL is shown in Figure 1.3. As shown in Figure 1.4, Jinping Tunnel measures about 17 km long, Jinping Mountain measures about 4100 m high, and the elevation of the laboratory is about 1600 m. The deepest overburden is about 2400 m, or 6720 meter-water-equivalent assuming a constant rock density of 2.8 g/cm^3 .



Figure 1.3 The location of CJPL. The position of Jinping traffic tunnels is indicated by the dashed line^[37]. (Based on Yahoo Map)

The first phase of CJPL (CJPL-I) was constructed at the end of 2009. The labora-

Figure 1.4 The cross section of Jinping Mountain^[38].

tory is in the middle of the traffic tunnels across the Jinping Mountain. There are two dark matter experiments (CDEX^[39] and PandaX^[40]) and a 1-ton prototype of the Jinping Neutrino Experiment^[41] running at CJPL-I now. The second phase of CJPL (CJPL-II) started at the end of 2014, in order to provide more space for experiments.

Table 1.2 lists the result of rock radioactivity measurement in Jinping Tunnel^[42]. Also listed are those measured in Sudbury^[43], Gran Sasso^[44], and Kamioka^[45].

Table 1.2 Rock radioactivity in Bq/kg for some underground laboratories^[37].

Site	^{238}U	^{232}Th	^{40}K
Jinping	1.8 ± 0.2 (^{226}Ra)	< 0.27	< 1.1
Sudbury	13.7 ± 1.6	22.6 ± 2.1	310 ± 40
Gran Sasso hall A	116 ± 12	12 ± 0.4	307 ± 8
Gran Sasso hall B	7.1 ± 1.6	0.34 ± 0.11	7 ± 1.7
Gran Sasso hall C	11 ± 2.3	0.37 ± 0.13	4 ± 1.9
Kamioka	~ 12	~ 10	~ 520

Because of the 2400 m rock overburden, the muon flux is as low as $\sim 10^{-10} \text{ cm}^{-2} \text{ s}^{-1}$ ^[38]. All commercial nuclear power plants in operation and under construction^[46] are far away from CJPL. Figure 1.5 shows the location of all the plants together with the underground laboratories at Sudbury, Gran Sasso, Kamioka, and Jinping, respectively. The cosmic-ray muon and the expected reactor neutrino background fluxes are also shown in Figure 1.6 for comparison.

1.6 Physics prospects of the MeV-scale neutrino experiment at CJPL

A MeV-scale neutrino experiment was proposed to be built at CJPL in 2016^[37]. The primary goals include the study of solar neutrinos, geo-neutrinos, and supernova relic

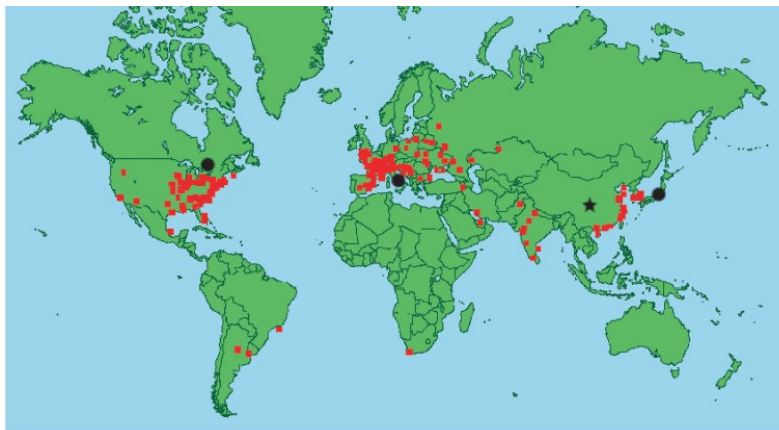


Figure 1.5 The location of all nuclear power plants and underground laboratories at Sudbury, Gran Sasso, Kamioka, and Jinping^[37].

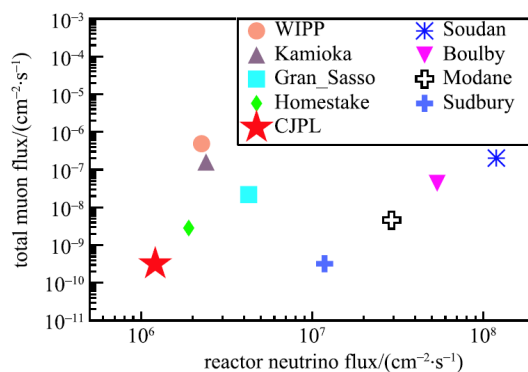


Figure 1.6 Muon and reactor neutrino fluxes at underground laboratories in the world^[37].

neutrinos. Neutrinos from dark matter annihilation can also be studied. The total fiducial target mass is 2000 ~ 3000 tons. In the proposal, the liquid scintillator with longer fluorescent time, referred to as slow liquid scintillator, is recommended because of the ability to provide both direction and energy measurements.

1.6.1 Jinping sensitivity for solar neutrinos

The proposed MeV-scale neutrino experiment at CJPL detects solar neutrinos via the neutrino electron elastic scattering (ES) process,

$$\nu_{e,\mu,\tau} + e^- \rightarrow \nu_{e,\mu,\tau} + e^- \quad (1-34)$$

The Feynman diagram of this process is shown in Figure 1.7. The electron recoil spectrum is thus continuous even in the case of monoenergetic neutrinos and it extends up to a

maximum energy T_{\max} given by

$$T_{\max} = \frac{E_\nu}{1 + \frac{m_e}{2E_\nu}} \quad (1-35)$$

where E_ν is the neutrino energy, m_e is the electron mass.

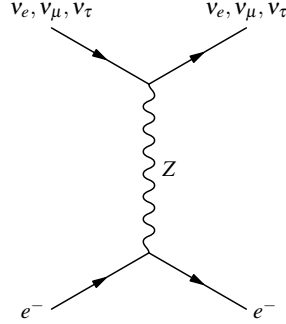


Figure 1.7 The Feynman diagram of the neutrino electron elastic scattering process.

A simulation study^[37] evaluated the sensitivity for solar neutrino measurement. The expected signal and background levels, energy resolution, fiducial mass, and live time were considered. A systematic uncertainty of 1.5% was assigned to all the input fluxes.

With a baseline configuration of 2000-ton fiducial mass, 1500-day exposure, and 500 PE/MeV energy resolution, the Jinping Neutrino Experiment can discover the CNO neutrinos and improve the precision of other solar neutrino components (pp, ^7Be , and pep) measurement. The flux measurement can also provide a tight constraint on the vacuum-matter transition to the MSW effect and the capability to distinguish different metallicity hypotheses. The details are discussed below.

1.6.1.1 Precision for solar neutrino measurement

Table 1.3 lists the expected recoiling electron event rates for different metallicity hypotheses. The detection threshold is set to be 200 keV.

Figure 1.8 shows the fit results of solar neutrino components with the baseline configuration. The hep neutrino component is negligible because the contribution is not significant. Although there are three solar neutrino components in the CNO cycle process (^{13}N , ^{15}O and ^{17}F), the ^{15}O and ^{17}F spectrum shapes are not distinguishable, only the ^{15}O component is considered in the fitter. Table 1.4 lists the relative statistical uncertainties for the detectable solar neutrino components.

The flux of CNO neutrinos strongly depends on the metallicity hypotheses^[37]. The dominant background sources for the CNO neutrino detection are the ^7Be , pep neutrinos,

Table 1.3 The expected recoiling electron event rates for different metallicity hypotheses. The uncertainties are all from the solar model prediction only^[37].

Electron event rate /day/100 ton	GS98 high metallicity	AGS09 low metallicity
pp	4.557 ± 0.027	4.595 ± 0.028
⁷ Be (384 keV)	0.228 ± 0.016	0.208 ± 0.015
⁷ Be (862 keV)	31.6 ± 2.2	28.8 ± 2.0
pep	2.244 ± 0.027	2.291 ± 0.028
¹³ N	1.48 ± 0.21	1.09 ± 0.15
¹⁵ O	2.03 ± 0.31	1.42 ± 0.21
¹⁷ F	0.0506 ± 0.0086	0.0312 ± 0.0053
⁸ B	0.427 ± 0.060	0.351 ± 0.049
hep	0.0009 ± 0.0003	0.0009 ± 0.0003

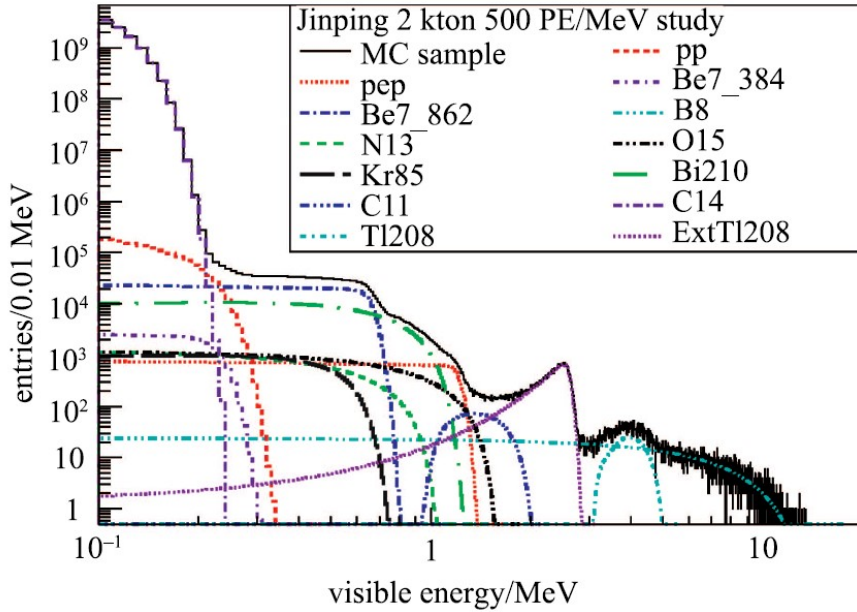


Figure 1.8 Solar neutrino fit results for the simulation sample^[37].

Table 1.4 Relative statistical uncertainties of solar neutrino fluxes for 2000-ton target mass, 1500-day live time and 500 PE/MeV energy resolution.

Component	Statistical uncertainty
pp	0.5%
${}^7\text{Be}$	0.4%
pep	3%
${}^{13}\text{N}$	30%
${}^{15}\text{O}$	10%
${}^8\text{B}$	2%

and radioactive ${}^{11}\text{C}$, ${}^{85}\text{Kr}$ and ${}^{210}\text{Bi}$ decays. Sufficient identification of background events will help to resolve the CNO neutrinos and relies on the energy resolution and particle identification provided by the slow liquid scintillator. The discovery of the ${}^{15}\text{O}$ neutrinos at Jinping will be possible if the relative uncertainty is better than 10% with a resolution of 500 PE/MeV.

1.6.1.2 Matter-vacuum transition phase

We must consider the matter effect when calculating the survival probability of solar neutrinos from the interior to the surface of the Sun. The survival probability can be approximated by the following formula^[47-48],

$$P^{\odot}(\nu_e \rightarrow \nu_e) = \cos^4 \theta_{13} \left(\frac{1}{2} + \frac{1}{2} \cos 2\theta_{12}^M \cos 2\theta_{12} \right) \quad (1-36)$$

the effective mixing angle in matter is

$$\cos 2\theta_{12}^M = \frac{\cos 2\theta_{12} - \beta}{\sqrt{(\cos 2\theta_{12} - \beta)^2 + \sin^2 2\theta_{12}}} \quad (1-37)$$

where

$$\beta = \frac{2\sqrt{2}G_F \cos^2 \theta_{13} n_e E}{\Delta m_{12}^2} \quad (1-38)$$

where G_F is the Fermi coupling constant, E is the neutrino energy, n_e is the density of electrons in the Sun. This effect has been studied by previous experiments, such as Borexino^[35,49], Super-Kamiokande^[50] and SNO^[51]. The current status is shown in Figure 1.9. The oscillation pattern in the transition region (1 ~ 10 MeV) is still loosely constrained. With a baseline configuration of 2000-ton fiducial mass, 1500-day exposure, 500 PE/MeV

energy resolution and low metallicity hypothesis, the expected flux measurements result of Jinping is shown in Figure 1.10.

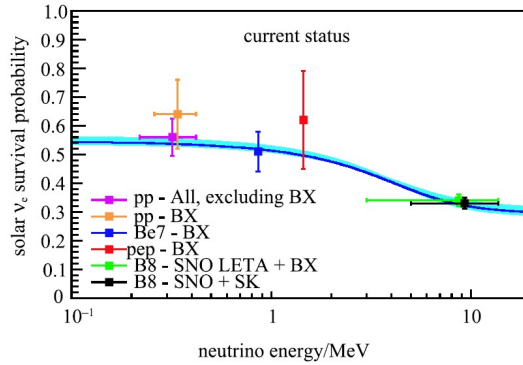


Figure 1.9 The survival probability from the vacuum to matter effect as a function of the neutrino energy, together with the present measurements. Theoretical prediction and its uncertainty are shown in the central line. The uncertainty of theoretical prediction is calculated by marginalizing $\theta_{12}, \theta_{13}, \Delta m_{12}^2$ with the present experimental uncertainty^[37].

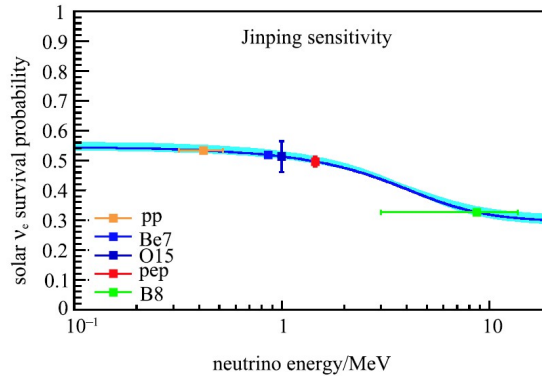


Figure 1.10 The survival probability from the vacuum to matter effect as a function of neutrino energy. The predicted sensitivities at Jinping are also plotted.

1.6.2 Jinping sensitivity for geo-neutrinos

Neutrinos from reactors are the main background of geo-neutrino measurement. The long-distance from nuclear power plants makes Jinping ideal to precisely measure the geo-neutrino flux. Table 1.5 summarizes the total signal and reactor background rates at Jinping. In the geo-neutrino signal region, the signal to background ratio is rather promising because the reactor neutrino background rate is less than 30 events per kiloton·1500 day.

With the actual signal and background spectra, 3 kilotons of fiducial mass, 1500-days exposure, and a resolution of 500 PE/MeV, a likelihood fit with both signals and backgrounds are performed on the simulation data. Figure 1.11 shows one example of a

Table 1.5 Total geo-neutrino and reactor neutrino event rates at Jinping^[37].

Component	rate/kton/1500 day
²³⁸ U	138
²³² Th	34
Total geo-neutrinos	172
Reactor background	64

fit with a free Th/U ratio. The uncertainty of ²³⁸U and ²³²Th fraction can reach down to 6% and 17%, respectively. The result shows that the ratio of Th/U ratio can be measured with a 27% precision.

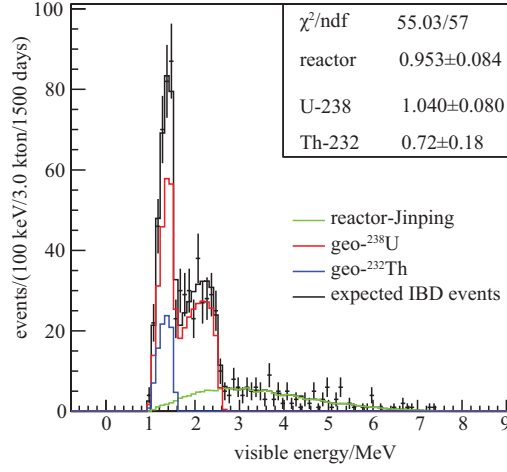

 Figure 1.11 Fit result for both the geo-neutrino signals and backgrounds^[37].

Figure 1.12 shows two possible outputs with uncertainties. The geo-neutrino flux predicted by different models as a function of heat production is compared with the expected measurement at Jinping. It is clear that Jinping has the sensitivity to test the models.

1.6.3 Jinping sensitivity for supernova relic neutrinos

The SRN energy spectrum $\phi(E)$ can be predicted by^[52]:

$$\frac{d\phi(E)}{dE} = \int_0^{\infty} (1+z)\phi[E(1+z)]R_{\text{SN}}(z) \left| \frac{cdt}{dz} \right| dz \quad (1-39)$$

where the integrand z is the redshift, $R_{\text{SN}}(z)$ is the core-collapse rate density, $\left| \frac{cdt}{dz} \right|$ is the cosmological line-of-sight factor. Figure 1.13 shows the $\bar{\nu}_e$ spectra for supernova relic neutrinos predicted by different models.

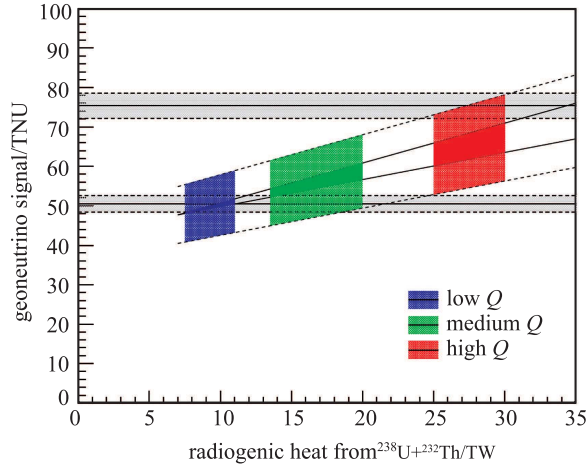


Figure 1.12 Geo-neutrino signals and model predictions at Jinping. The two horizontal shade areas are two possible geo-neutrino flux assumptions with the expected sensitivity at Jinping^[37].

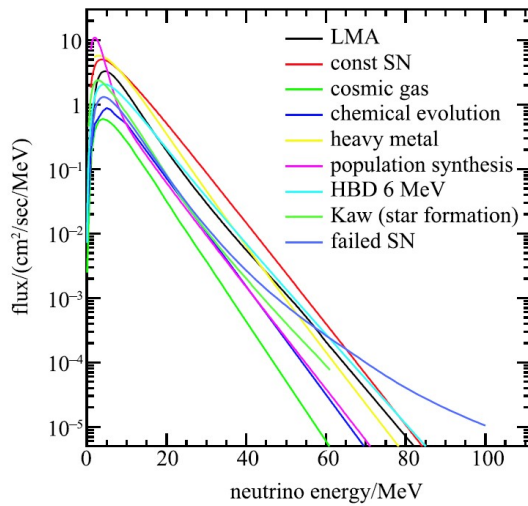


Figure 1.13 The $\bar{\nu}_e$ spectra for supernova relic neutrinos predicted by different models^[37].

All three flavors of neutrinos and anti-neutrinos exist in SRNs. Anti electron neutrinos are the most likely to be detected. Within the energy region of several tens of MeV, the cross-section of IBD is large in hydrogen-rich material, and the delayed coincidence with neutron capture gives a powerful tool to reject backgrounds.

A simulation study^[53] calculated the expected numbers of various backgrounds and SRN signals corresponding to a detector of water, Gd-doped water, a typical liquid scintillator, and LAB as the slow liquid scintillator at Jinping. In an LAB detector at Jinping with an exposure of 20 kiloton-years, the significance level of the SRN discovery within [10.8, 30.8] MeV can reach 99.95% (3.5σ).

1.7 Slow liquid Scintillator

Several studies^[37,54-55] have indicated that providing direction and energy measurements on charged particles can give an extra power to distinguish signal and background in MeV-scale neutrino experiments. Water Čerenkov detectors can detect Čerenkov light and reconstruct the direction. However, this type of detector has a low light yield and a high energy threshold for MeV-scale neutrino events. It is important to note that discriminating individual solar neutrino flux components from the recoiled electron energy spectrum requires a reasonable good energy resolution, which should be at least 4.5% at 1 MeV energy deposit, i.e., 500 photoelectrons/MeV^[37]. This requirement exceeds the yield limit of photoelectrons in water or heavy water Čerenkov detectors.

Liquid scintillator detectors can meet the light yield requirement. However, the liquid scintillator adopted in present neutrino experiments only provides energy information, because the vast scintillation light completely submerges the small amount of Čerenkov light emitted by charged particles.

The slow liquid scintillator can detect Čerenkov and scintillation light simultaneously. The concept of diluted scintillators was pioneered as part of the LSND experiment^[56]. However, its light yield is still low and not applicable to the dedicated low-energy neutrino experiments. Discrimination between Čerenkov and scintillation photons can be achieved in several ways: water-based liquid scintillator (WbLS)^[57] and oil-based slow liquid scintillator (SLS)^[58]. Meanwhile, the development of fast timing of newly available PMTs and the ultrafast timing of LAPPDs (Large Area Picosecond Photon Detectors) allows for more effective reconstruction techniques^[34].

Jinping Neutrino Experiment and THEIA^[54] are considering the detection scheme

with the slow scintillator. This new type of slow liquid scintillator has large time constants and suppresses the absorption and re-emission of Čerenkov light, providing an opportunity to separate the Čerenkov light from the scintillation light.

For solar neutrino detections, if the direction of a charged particle is reconstructed, a solar angle cut is a powerful tool to suppress radioactive backgrounds. If the scintillator is doped with some other isotopes, such as ${}^7\text{Li}$, solar neutrinos can be detected via two channels^[34]:

Elastic scattering (ES). The sensitivity to CNO and pep solar neutrinos of a 50 kiloton WbLS detector via the ES interaction has been studied^[59]. The angle between the incoming particle direction and the direction to the Sun, $\cos\theta_{\odot}$, can be used to differentiate signal from background. Due to the kinematics of the ES interaction, solar neutrinos are predominantly directed away from the Sun. This solar angle provides a key handle to discriminate solar neutrino events from an isotropic radioactive background. Neutrino flux sensitivities are determined using a binned maximum-likelihood fit over two-dimensional PDFs in energy and $\cos\theta_{\odot}$. The sensitivity of CNO neutrinos in a 50 kiloton detector via ES interaction is better than 10% if the angular resolution is 35° .

Charged current (CC). The CC interaction of ν_e on ${}^7\text{Li}$ is



CC neutrino detection allows extraction of the low-energy ${}^8\text{B}$ spectrum, providing a sensitive search for the transition region of the MSW effect in the solar neutrino oscillation. In the CC analysis, the ES signals are the background. Figure 1.14 shows the predicted spectrum for a 30-kiloton fiducial volume loaded with 1% ${}^7\text{Li}$ by mass, and a conservative light yield of 100 photoelectrons per MeV^[34]. The bottom panel shows the spectrum with a cut placed on $\cos\theta_{\odot} = 0.4$, which reduces the ES signals by more than two orders of magnitude.

For geo-neutrino detections, if the solar neutrino background can be suppressed by the direction information, the ${}^{40}\text{K}$ component of geo-neutrinos can be identified by the neutrino-electron elastic scattering process with 3σ precision with a kiloton-scale detector^[60].

For supernova relic neutrino detections, the primary background is from atmospheric neutrinos^[53]. This background, which is generated via the neutral and charged current interactions, can be effectively suppressed if we can detect Čerenkov light for particle

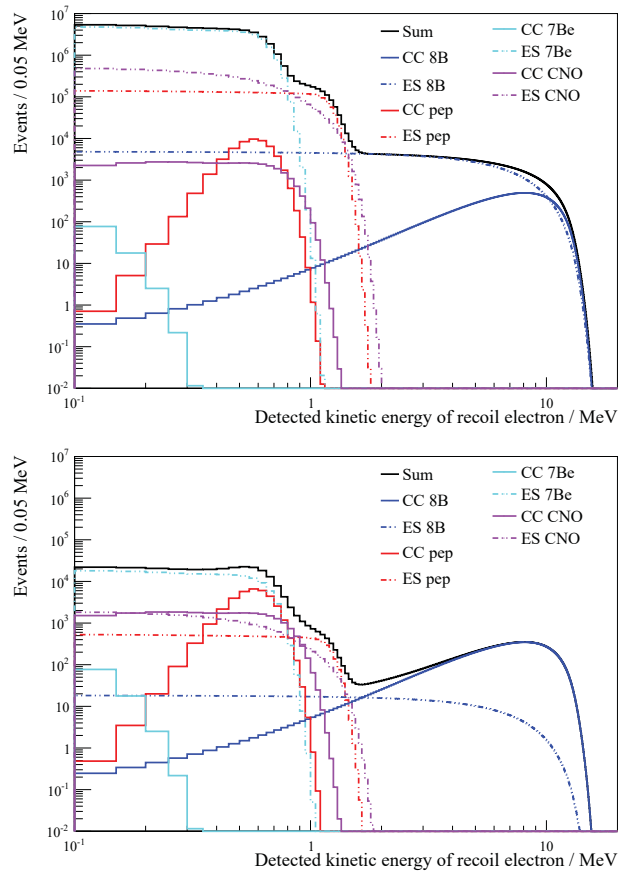


Figure 1.14 (Top) Predicted solar neutrino spectra in a 30-kT WbLS detector loaded with 1% ^7Li by mass. (Bottom) The same spectra with a cut on $\cos \theta_{\odot} = 0.4$, reducing the ES component to illustrate the power of CC detection. This plot is taken from Ref. [34].

identification, because proton and neutron in this energy range do not produce Čerenkov light, whereas electron and muon do. The results of significance levels (converted to χ^2 quantiles in units of σ) are shown in Figure 1.15.

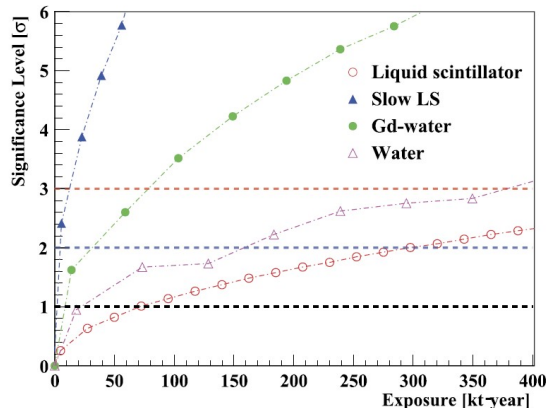


Figure 1.15 Significance levels (converted to χ^2 quantiles in units of σ) versus the exposure of several different types of detectors^[53].

In addition, a further particle identification is possible based on the ratio of Čerenkov light to scintillation light yield. This feature is useful for neutrinoless double beta decay ($0\nu\beta\beta$)^[61-63], neutrino CP phase^{[64][65]}, proton decay^[55] and geoneutrino^[66] experiments.

The thesis focuses on the LAB-based slow liquid scintillator. LAB was revisited in our study^[67]. A quadruple coincidence system was used to select vertical cosmic-ray muons. LAB has a characteristic of a considerable decay time constant of 35 ns, and can thus serve as a slow liquid scintillator. This feature could be applied to separate Čerenkov and scintillation lights by analyzing the time profile of the analogous output of a photomultiplier tube (PMT), given that the prompt time region is dominated by the former while the late time range is dominated by the latter. The slower the fluorescence, the better the separation ability. Figure 1.16 shows the simulation result of a 100 MeV muon emitted in the center of a 12 m-radius LAB detector. In the beginning, we can observe the Čerenkov ring, and later we only observe the uniform scintillation.

Since the light yield of LAB is much lower than that of typical liquid scintillators widely used in neutrino experiments, especially in low-energy solar neutrino experiments, CHESSE experiment^[57,68] has made good progress by adding 2,5-diphenyloxazole (PPO) and applying fast photon detectors^[69] to enhance the light yield and maintain the scintillation-Čerenkov separation ability. However, for large neutrino detectors (quick absorption below 400 nm in LAB) or neutrino detectors using acrylic material (transmit-

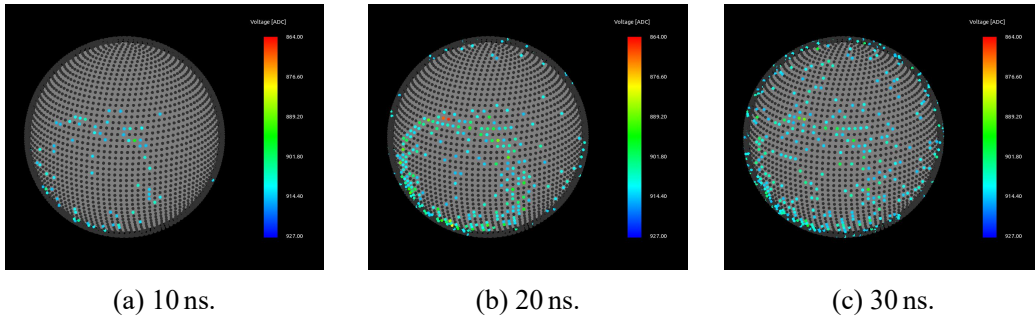


Figure 1.16 PMT responses of an LAB detector for a 100 MeV muon event at different times. A prompt Čerenkov cone is visible, while the isotropic slow scintillation light can also be seen later.

tance is cut off at about 300 nm), the light propagation loss cannot be ignored. We still need to shift the emission spectrum from the short wavelength to the more extended range (> 400 nm) to reduce the light propagation loss. This goal can be achieved by adjusting the concentrations of PPO and 1,4-bis (2- methylstyryl)-benzene (bis-MSB)^[70-71]. On the other hand, adding too much PPO and bis-MSB will weaken the separation ability between scintillation and Čerenkov lights, especially when using a more economical PMT detection approach. The timing precision of PMT is a few nanoseconds scale, and massive production is possible. The balance of time profile and light yield is vital to both the Čerenkov separation ability and the high energy resolution, which requires further study.

1.8 Organization of this thesis

The organization of this thesis is as follows. Chapter 1 briefly describes the neutrino property, the physics in MeV-scale neutrinos, the introduction of CJPL, and the slow liquid scintillator. Chapter 2 describes the studies of the LAB-based slow liquid scintillator in a 20 L small prototype detector, the scintillator properties, and performance evaluation. Chapter 3 provides the design and development of the simulation framework, which can be applied in the MeV-scale neutrino experiment. Chapter 4 discusses the design and construction of the 1-ton prototype detector for testing the slow liquid scintillator and backgrounds. Chapter 5 reports the performance of the 1-ton prototype detector, including the calibration, reconstruction, and Čerenkov light search. Chapter 6 reports the muon flux measurement by using the 1-ton prototype detector. Chapter 7 comes to conclusions and outlook.

Chapter 2 Studies of Slow Liquid Scintillator

In this chapter, we first report the studies on the Čerenkov component of a slow liquid scintillator based on LAB, the investigation of the light yields and time profiles for various formulas, and a proposed model to describe the inverse relationship between the light yield and the time profile. And then, we give the measurement on the scintillation emission spectra and attenuation length, and the measurement of the light transmission in acrylic - a typical container material for neutrino experiments. All of which are critical parameters in optimizing the design of MeV-scale neutrino detectors. Finally, we detail the evaluation of performance for a kiloton-scale detector using the candidate samples.

2.1 The 20 L Detector

2.1.1 Detector layout

We built a specific detector to conduct an experimental study on the separation between the Čerenkov and scintillation light in the LAB-based slow liquid scintillator. The yield and time profile of scintillation light can also be measured. Figure 2.1 shows the detector layout.

Four plastic scintillators for coincidence trigger were positioned vertically. When a cosmic-ray muon passes through the detector, the four plastic scintillators provide a quadruple-coincidence signal. Two plastic scintillators for vetoing the cosmic-ray shower were placed next to the bottom scintillator. These events can disturb the distinguished time profile.

An acrylic container was placed between the second and third coincident scintillators. The inner surface of the container was lined by a layer of coarse black acrylic to suppress reflections. The fiducial volume was 15.4 L. The container was filled with liquid scintillator. The formulas were LAB doped with different concentrations of 2,5-diphenyloxazole (PPO) and 1,4-bis (2-methylstyryl)-benzene (bis-MSB). We weighted PPO and bis-MSB by an electronic balance with 1 mg division minimal, and dissolved them in LAB into a 500 mL beaker. The concentrated solution was poured into the acrylic container, and the mixture was thoroughly stirred.

Six PMTs (Channel 0 to 5) collected light signals from the six coincidence and veto

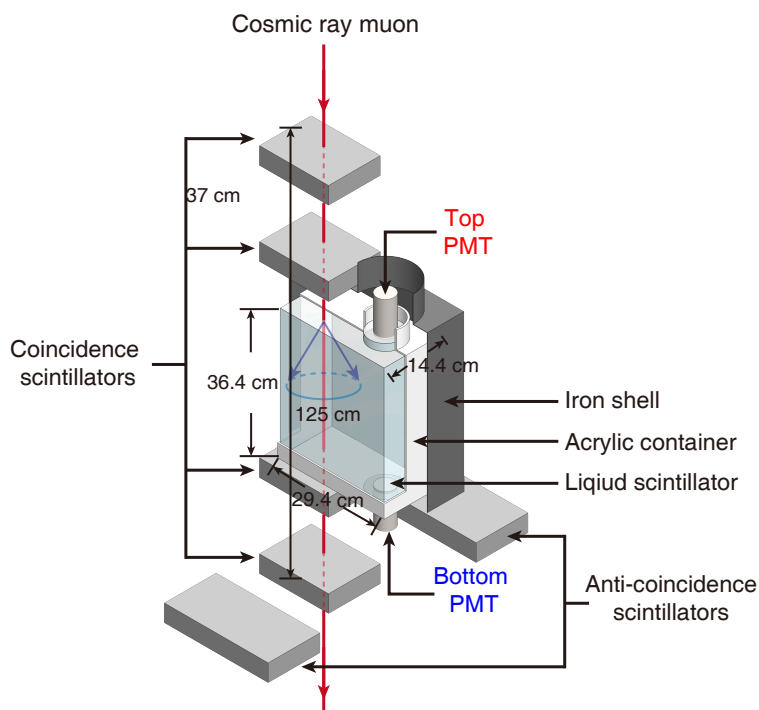


Figure 2.1 Layout of the 20 L detector.

plastic scintillators. Two PMTs (the top and bottom one) acquired the liquid scintillator's signals in the acrylic container. These two PMTs were symmetrically aligned with the acrylic container and immersed in the liquid scintillator for functional optical coupling. The top and bottom PMT were model Hamamatsu R1828-01. The diameter of the active photocathode area is 46 mm. The quantum efficiency is more than 10% from 300 to 530 nm, as shown in Figure 2.2. The rise time of the anode pulse is 1.3 ns.

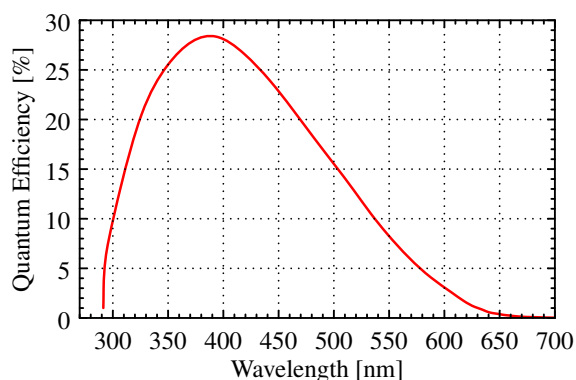


Figure 2.2 Quantum efficiency of Hamamatsu R1828-01.

The waveforms of the total eight PMTs were fed into one CAEN V1751 board, an 8 Channel 10 bit 1 GS/s waveform digitizer. Once a quadruple-coincidence signal of Chan-

nel 0 to 3 was issued, V1751 opened a 4096-ns window and read out the voltage waveforms of all eight PMTs. The waveforms were further analyzed offline.

2.1.2 Detector simulation

We modeled the whole apparatus in the simulation based on Geant4^[72-73] to validate the understanding of the collected data and to estimate the detection efficiency of scintillation light for light yield measurement. Standard electromagnetic and muon-nucleus processes were both included. We customized the quenching effect, time profile, and light yield of scintillation, PMT response, etc., in the program.

The simulation started with a cosmic-ray muon generator. Muons started on the top surface of the first coincidence scintillator. The energy and zenith angle follow the modified Gaisser formula^[74],

$$G(E, \theta, \phi) \equiv \frac{dN}{dE d\Omega} = \frac{I_0}{\text{cm}^2 \cdot \text{s} \cdot \text{sr} \cdot \text{GeV}} \cdot \left(\frac{E^*}{\text{GeV}} \right)^{-\gamma} \cdot \left(\frac{1}{1 + \frac{1.1E \cos \theta^*}{115\text{GeV}}} + \frac{0.054}{1 + \frac{1.1E \cos \theta^*}{850\text{GeV}}} \right) \quad (2-1)$$

where E is the muon kinetic energy, θ is the zenith angle, I_0 is a normalization constant, $\gamma = 2.7$ is the muon spectral index,

$$I_0 = 0.14, \quad E^* = E \left[1 + \frac{3.64 \text{ GeV}}{E \cdot (\cos \theta^*)^{1.29}} \right]$$

$$\cos \theta^* = \sqrt{\frac{\cos^2 \theta + P_1^2 + P_2(\cos \theta)^{P_3} + P_4(\cos \theta)^{P_5}}{1 + P_1^2 + P_2 + P_4}},$$

$$P_1 = 0.102573, \quad P_2 = -0.068287, \quad P_3 = 0.958633,$$

$$P_4 = 0.0407253, \quad P_5 = 0.817285,$$

Only 0.8% of muons could satisfy the quadruple-coincidence requirement. With the muon flux at sea level $\sim 1/(\text{cm}^2 \cdot \text{min})$, the simulated event rate was estimated to be 1.8/min.

Organic scintillators like LAB, do not respond linearly with ionization density. Birks' Law^[75] is a semi-empirical formula to describe the quenching effect,

$$\frac{dE_{\text{vis}}}{dx} = \frac{dE/dx}{1 + k_B dE/dx} \quad (2-2)$$

where dE/dx and dE_{vis}/dx , and are the energy loss density and visible energy loss density for scintillation light generation of a charged particle, k_B is Birks' constant. The Birks' constant used in the simulation was 0.015 cm/MeV ^[76] and dE_{vis}/dx was decreased by 2.8% for dE/dx . The total visible energy in the liquid scintillator sample was estimated to be $(69.1 \pm 1.9) \text{ MeV}$, with the uncertainty evaluated by the study with or without quenching. The simulation also considered the fluctuation of muon track length due to the muon angular distribution, which was less than 1%, and also included in the uncertainty.

The uncertainty of the reflectivity of the inner surface of the container resulted in a systematic uncertainty. We scanned the diffused reflectivity from 0% to 10% in the simulation. The estimated efficiency with 5% reflectivity was used as central value. The uncertainty of the reflectivity introduced less than 6% uncertainty to the detection efficiency.

The light propagation distance in the acrylic container was several tens of centimeters, comparable with the attenuation length of short-wavelength light ($< 400 \text{ nm}$) in LAB^[77], as shown in Figure 2.3.

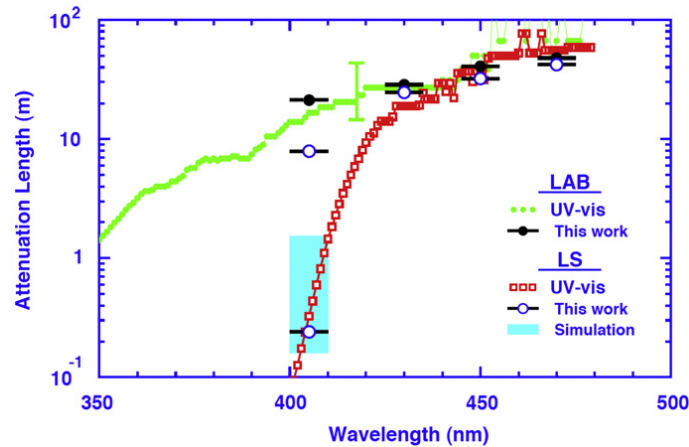


Figure 2.3 Attenuation length spectrum of LAB and liquid scintillator (LAB + 3 g/L PPO + 15 mg/L bis-MSB)^[77].

Since the attenuation effect cannot be ignored, we used a combination of all the

solution components to represent the attenuation length spectrum as below,

$$\frac{1}{L} = \sum \frac{n_i}{n_{0i} L_i}, \quad (2-3)$$

where L is the overall attenuation length, n_i is the concentration of the i -th component, and L_i is the attenuation length measured at concentration n_{0i} . Some studies^[77-78] gave the attenuation length spectra of pure LAB, LAB+3 g/L PPO, LAB+3 g/L PPO+15 mg/L bis-MSB. We can extract the individual attenuation length spectra of PPO and bis-MSB according to Eq. (2-3),

$$\frac{1}{L_{\text{PPO}}} = \frac{1}{L_{\text{LAB+PPO}}} - \frac{1}{L_{\text{LAB}}}, \quad (2-4)$$

$$\frac{1}{L_{\text{bis-MSB}}} = \frac{1}{L_{\text{LAB+PPO+bis-MSB}}} - \frac{1}{L_{\text{LAB}}} - \frac{1}{L_{\text{PPO}}}. \quad (2-5)$$

The refractive index used in the simulation was also a function of wavelength. Another study^[79] measured the refractive index of the LAB-PPO solution and parametrized the dispersion. For the range 210 ~ 230 nm, the dispersion can be described by a third-order polynomial,

$$n(\lambda) = A_0 + A_1 \lambda + A_2 \lambda^2 + A_3 \lambda^3 \quad (2-6)$$

For the range of 230 ~ 1000 nm, the dispersion is parametrized with the Sellmeier formula,

$$n^2(\lambda) = 1 + \sum_{i=1}^4 \frac{B_i}{1 - (C_i/\lambda)^2} \quad (2-7)$$

In both equations, the unit of λ is nm.

2.1.3 Event selection

Figure 2.4 shows a typical waveform of six coincidence channels, with the definition of the peak, width, and charge for each waveform. The peak, width, and charge are calculated for each waveform. Besides single vertical-going muons, two types of backgrounds should be excluded: electronics noise events and multi-track or shower events. (1) Electronics noise events, mainly caused by coherent noises in the environment, such as the power supplies of the PMTs or electromagnetic interference. The waveforms are

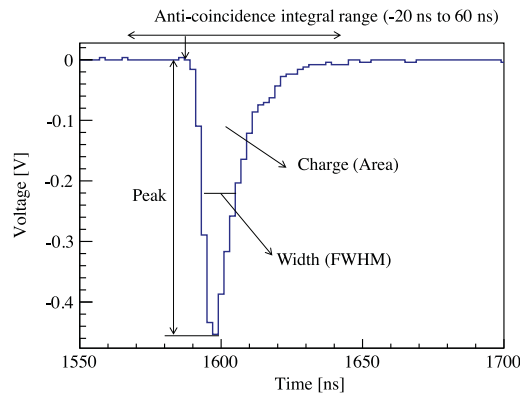


Figure 2.4 A typical waveform of the coincidence channels.

much narrower than the physical signals. Cuts on the peak-to-charge-ratio and peak-to-width-ratio are effective in removing these backgrounds. (2) Multi-track or shower events, caused by several muon tracks arriving at the same time, or several secondary tracks induced by a single muon. All events were required to have charges not to be significantly higher than baseline fluctuations in the anti-coincidence channels are rejected. Furthermore, the charge of coincidence channels was also checked. The energy deposit should follow a Landau distribution with the assumption of minimum-ionizing particles. Figure 2.5 shows the fitting result with a Landau distribution. We rejected the events with a charge smaller than 0.05 nC, or larger than 0.3 nC in any of the coincidence channels.

After the event selection, more than 2000 candidates survived for each slow liquid scintillator sample, giving an event rate of about 1.7/min. Figure 2.6 shows the waveforms of the eight channels for one candidate event in a pure LAB sample. The bottom PMT observed both scintillation and Čerenkov lights, while the top PMT only observed scintillation light as expected.

2.1.4 PMT gain calibration

We performed the PMT gain calibration once a day. In the gain calibration run, only recorded were the top or bottom PMT waveforms, with a trigger threshold at -2 mV. . For a proper calibration, there should be two peaks in the histogram of charge, as shown in Figure 2.7. The first peak lying at zero represents the baseline, while the second one represents the single photoelectron (PE) signals. The gain factor was the mean value from a fit to the second peak with a Gaussian function.

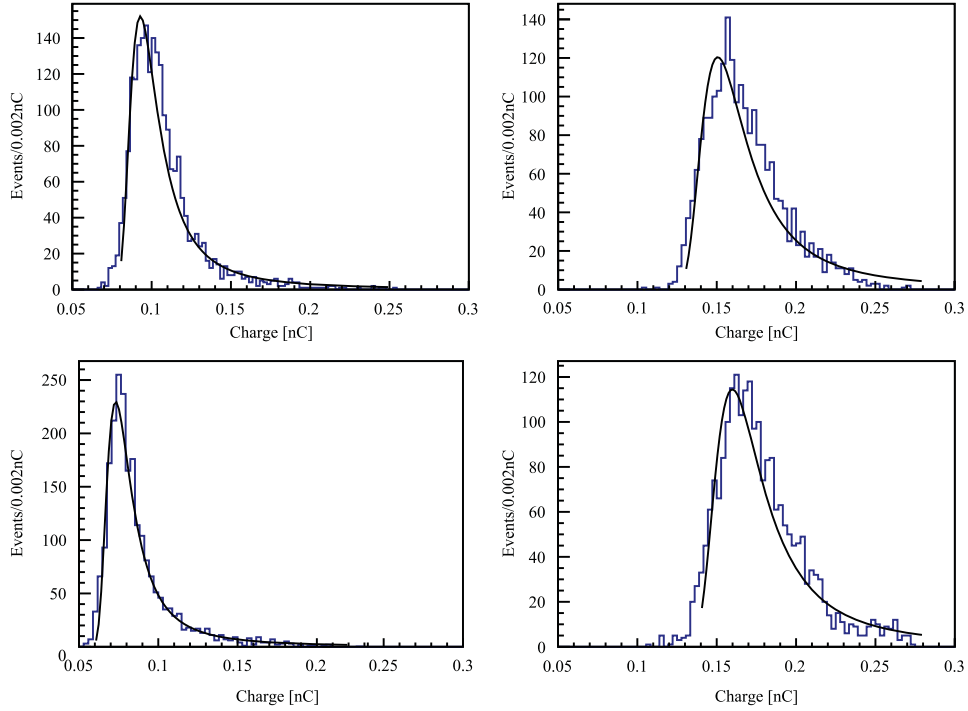


Figure 2.5 The charges distributions of the four coincidence scintillators. Fitted by Landau distribution.

2.2 Time profile measurement

The average waveforms of the selected candidates for some slow liquid scintillator samples are shown in Figures 2.8 and 2.9, respectively. We have corrected the relative difference of the gains and geometry acceptances between the two PMTs by the gain calibration and Monte-Carlo simulation. Because the cosmic-ray muons come from top to bottom, the direction of the forward Čerenkov light emitted by these muons is also from top to bottom. The top PMT can only detect the isotropic scintillation light, while the bottom PMT can detect both scintillation and Čerenkov lights. The average waveforms of two PMTs show that there is an apparent enhancement in the first 20 ns for the bottom PMT amplitude with respect to the top one. This enhancement is due to the contribution from the prompt Čerenkov component, and the peak height is highly dependent on the concentration of PPO and bis-MSB.

We constructed a function of the time profile with the PMT time response convoluted, taking into account both the Čerenkov and scintillation light contributions, as expressed by,

$$f_b(t) = [A_c \delta(t - t_c) + A_s n(t - t_s)] \otimes \text{gaus}(\sigma_b), \quad (2-8)$$

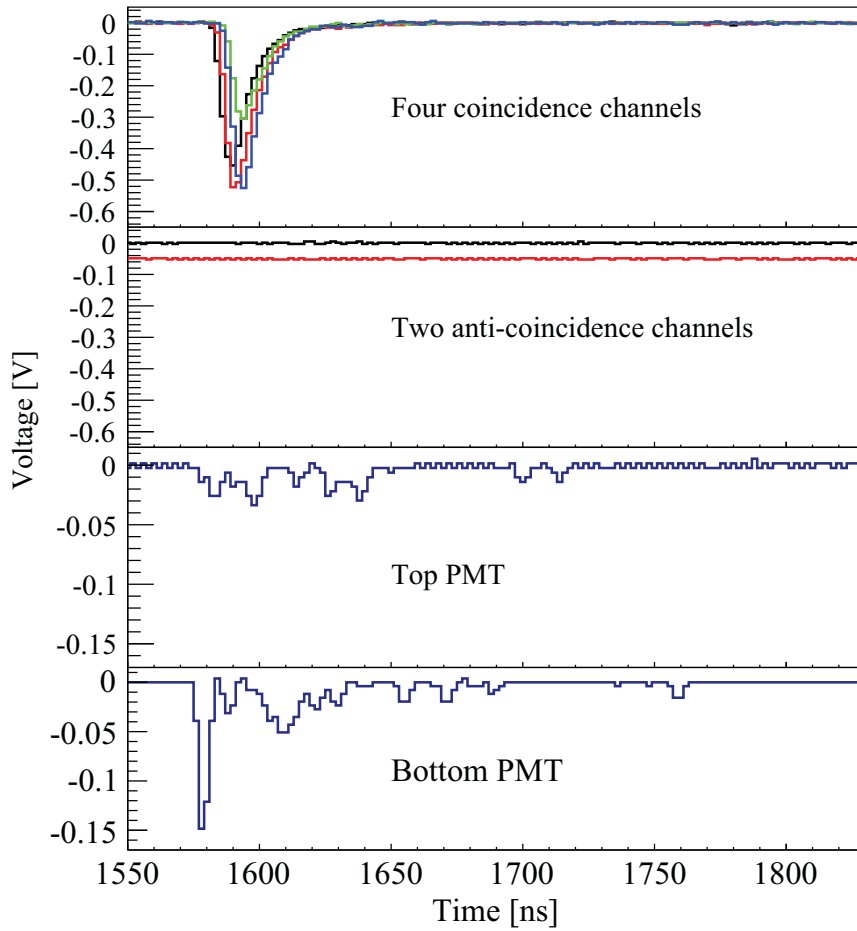


Figure 2.6 Waveforms of the eight channels for one candidate event of pure LAB sample. Waveforms of the two anti-coincidence scintillators are vertically shifted to avoid overlapping.

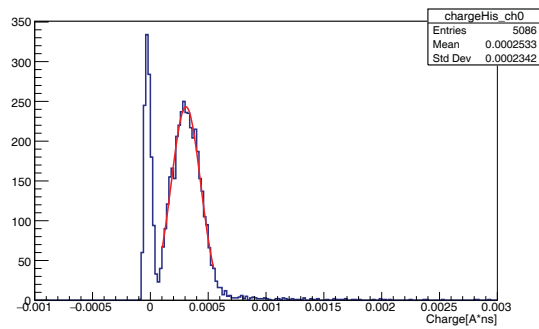


Figure 2.7 The charge distribution of a gain calibration run.

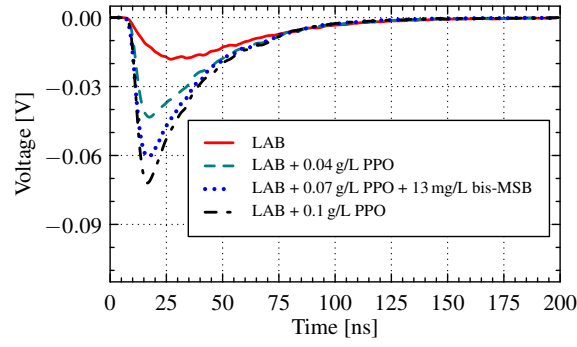


Figure 2.8 The average waveform of the top PMT. Only the scintillation light is presented, as expected.

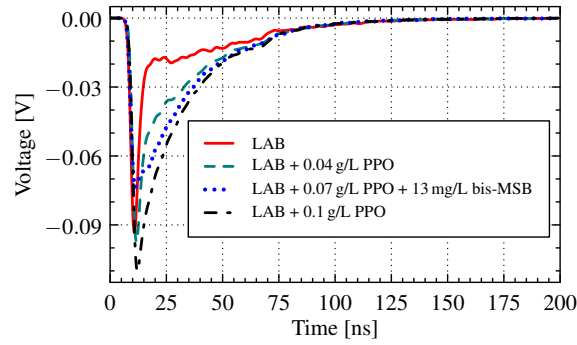


Figure 2.9 The average waveform of the bottom PMT. The sum of Čerenkov and scintillation lights are presented.

where A_c and t_c are the area and arrival time of the Čerenkov light. $\delta(t)$ represents the time profile of the prompt Čerenkov emission, which is a delta function since it is an instant process comparing to the PMT timing precision of ns. A_s and t_s are the area and arrival time of the scintillation light, respectively, $n(t)$ is the time profile of the scintillation emission, $\text{gaus}(\sigma_b)$ is the PMT time response function.

In contrast to the waveform of the bottom PMT, the waveform of the top PMT includes only the scintillation light contribution, which is expressed as

$$f_i(t) = A_s n(t - t_s) \otimes \text{gaus}(\sigma_i). \quad (2-9)$$

where A_s and t_s are the same as those defined in Eq. (2-8).

In a binary or ternary scintillator system, emissions may feature a finite rise time or be slightly lengthened in duration due to the finite time of intermolecular energy transfer^[75]. In organic solution scintillators, emissions present a finite rise time τ_r and a decay time τ_d so that a normalized pulse shape of scintillation light can be written as

$$n(t) = \frac{\tau_r + \tau_d}{\tau_d^2} (1 - e^{-t/\tau_r}) \cdot e^{-t/\tau_d} \quad (2-10)$$

Both the time constants τ_r and τ_d can be determined by Eq. (2-8) and Eq. (2-9). For example, an LAB sample with 0.07 g/L PPO and 13 mg/L bis-MSB, we determined $\tau_r = (1.16 \pm 0.12)$ ns and $\tau_d = (26.76 \pm 0.19)$ ns, respectively. Figure. 2.10 and 2.11 show the fitting results for both the top and bottom PMT waveforms, respectively.

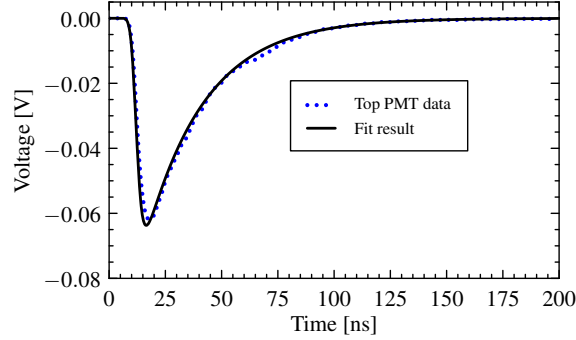


Figure 2.10 The fit to the top PMT's waveforms for the sample of LAB with 0.07 g/L PPO and 13 mg/L bis-MSB.

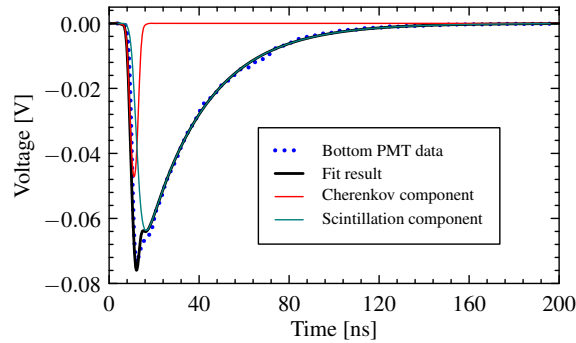


Figure 2.11 The fit to the bottom PMT's waveforms for the sample of LAB with 0.07 g/L PPO and 13 mg/L bis-MSB.

2.3 Light yield measurement

The number of scintillation photoelectrons D_s detected by the bottom PMT can be expressed as,

$$D_s = \frac{A_s}{A_g}, \quad (2-11)$$

where A_g is the single PE charge obtained from the PMT gain calibration, while A_s is the fitting result from both Eq. (2-8) and Eq. (2-9).

The detector efficiency is defined by the number of detected photoelectrons D_c or

D_s dividing the number of scintillation or Čerenkov photons N_c or N_s ,

$$\varepsilon_s \equiv \frac{D_s}{N_s}, \quad \varepsilon_c \equiv \frac{D_c}{N_c} \quad (2-12)$$

The detector simulation estimated the detection efficiency. The dominant uncertainty was associated with the PMT quantum efficiency, which is estimated to be 10%. Then the total number of scintillation photons N_s can be calculated from D_s divided by the detection efficiency ε_s ,

$$N_s = \frac{D_s}{\varepsilon_s} = \frac{A_s}{\varepsilon_s \cdot A_g}. \quad (2-13)$$

The scintillation light yield Y can be calculated by

$$Y = \frac{N_s}{E_{\text{vis}}} = \frac{A_s}{\varepsilon_s \cdot A_g \cdot E_{\text{vis}}}, \quad (2-14)$$

where E_{vis} is the total visible energy and was estimated to be (69.1 ± 1.9) MeV from the simulation in Section 2.1.2.

It is important to note that this light yield includes the contribution from the hard UV portion of Čerenkov light. This portion of Čerenkov light is absorbed and re-emitted in the liquid scintillator, losing the directional information of the original Čerenkov photons. They should be treated as part of the effective scintillation yield.

For the LAB sample with 0.07 g/L PPO and 13 mg/L bis-MSB, Table. 2.1 gives the numbers of measured PEs at the top and bottom PMTs, and the uncertainties are all fitting errors. The number of detected Čerenkov PEs was 5.47 ± 0.22 . The light yield for the sample was estimated to be $(4.01 \pm 0.60) \times 10^3$ photons/MeV.

Table 2.1 Measured photoelectrons for the LAB sample with 0.07 g/L PPO and 13 mg/L bis-MSB. The scintillation light is assumed to be isotropic, and thereby gives the same number of photoelectrons for both the top and bottom PMTs.

	Top	Bottom
Čerenkov light (PE)	--	5.47 ± 0.22
Scintillation light (PE)	56.1 ± 1.2	56.1 ± 1.2

2.4 Scanning of light yield and scintillation time

We scanned the concentration of PPO and bis-MSB, measured the scintillation light yield, rise time constant, decay time constant, and Čerenkov photoelectron yield for

each sample. Table 2.2 gives The results and the scintillation photon detection efficiencies. These quantities can affect the performance of separation between scintillation and Čerenkov lights. It has been noted that scintillator cocktails may feature more than one decay constant, due to the different components^[80]. We observed that the time profiles of high concentration scintillator cocktails (such as 2 g/L PPO or more) indeed have two or more decay exponential components, as shown in Figure 2.12. The weight of fast component (80%~90%) is much larger than that of the slow component. However, a single exponential can give a good fit for slow liquid scintillator samples, as shown in Figure 2.10, because the concentration is low enough.

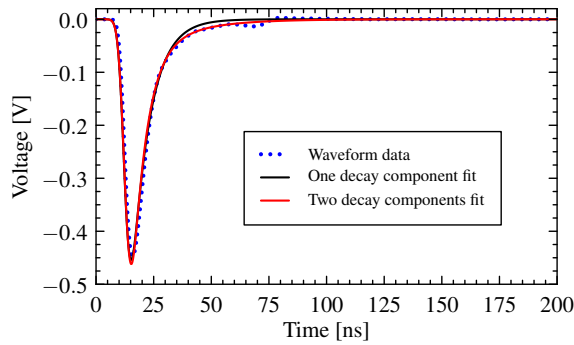


Figure 2.12 The fit to the top PMT’s waveforms for the sample of LAB with 2 g/L PPO.

The decay time constants and scintillation light yields are plotted in Figure 2.13 for all the test samples, showing an inverse relationship. The effect of wavelength shifter bis-MSB on decay time constants and scintillation light yields is relatively insignificant at low concentrations. Increasing PPO concentration will result in higher light yields and smaller time constants.

To understand this inverse relationship between the scintillation light yield and the

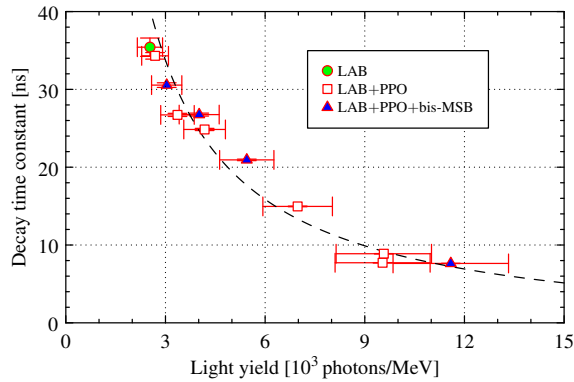


Figure 2.13 Decay time constant versus scintillation light yield for different concentrations of LAB, PPO, and bis-MSB solutions. The dashed line is a fit of Eq. (2-18).

Table 2.2 The scintillation photon detection efficiencies, scintillation light yields, time constants and Čerenkov PE numbers of the LAB samples with different concentrations of PPO and bis-MSB.

PPO (g/L)	bis-MSB (mg/L)	Detection efficiency ($\times 10^{-4}$)	Scintillation light yield (10^3 photons/MeV)	Rise time constant (ns)	Decay time constant (ns)	Number of Čerenkov photoelectrons
0	0	1.54 ± 0.23	2.53 ± 0.38	12.20 ± 1.39	35.42 ± 1.18	10.06 ± 0.40
0.02	0	2.23 ± 0.33	2.69 ± 0.40	3.72 ± 0.10	34.31 ± 0.42	9.08 ± 0.36
0.04	0.13	2.23 ± 0.33	3.04 ± 0.46	2.33 ± 0.20	30.55 ± 0.30	7.56 ± 0.30
0.07	0	2.20 ± 0.33	3.36 ± 0.50	1.33 ± 0.13	26.72 ± 0.20	8.58 ± 0.34
0.07	13	2.02 ± 0.30	4.01 ± 0.60	1.16 ± 0.11	26.76 ± 0.19	5.47 ± 0.22
0.1	0	2.18 ± 0.33	4.18 ± 0.63	1.15 ± 0.10	24.85 ± 0.14	8.26 ± 0.33
0.1	130	2.05 ± 0.31	5.45 ± 0.82	1.07 ± 0.18	20.94 ± 0.10	4.84 ± 0.19
0.5	0	2.13 ± 0.32	6.98 ± 1.05	1.00 ± 0.05	14.96 ± 0.04	7.55 ± 0.30
2	0	2.14 ± 0.32	9.57 ± 1.44	0.81 ± 0.04	8.88 ± 0.02	7.18 ± 0.29
3	0	2.10 ± 0.32	9.54 ± 1.43	0.64 ± 0.04	7.72 ± 0.02	7.24 ± 0.29
3	10	2.17 ± 0.33	11.59 ± 1.74	0.77 ± 0.04	7.63 ± 0.01	5.08 ± 0.20

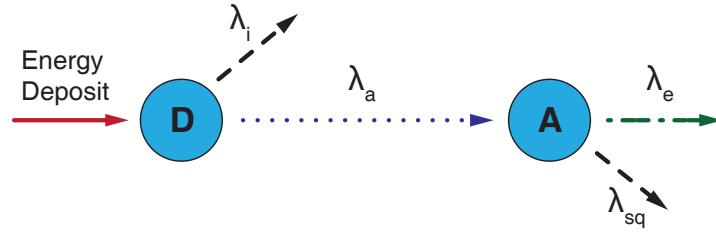


Figure 2.14 A simplified model of energy transfer paths between the donor (D) and acceptor (A) molecules in a liquid scintillator.^[81]

decay time constant, we examined the mechanism of light emission in the scintillator. As shown in Figure 2.14, incident charged particles in a liquid scintillator deposit their energies, some of which can be transferred between molecules.

The light yield Y from the energy transfer was modeled by a study^[81], as expressed by Eq. (2-15), in which the PPO concentration A represents the amounts of energy transfer,

$$Y = D \cdot \frac{1}{1 + \frac{\lambda_{sq}A}{\lambda_e}} \cdot \frac{1}{1 + \frac{\lambda_i}{\lambda_a A}} \quad (2-15)$$

where D is the number of excited solvent molecules, λ_{sq} is the self-quenching factor, λ_e is the rate of photon emission after self-quenching, λ_i is the internal loss factor of solvent molecules, and λ_a is the energy transfer from the solvent (donor) molecules to the solute (acceptor) PPO molecules.

The self-quenching effect is due to the interaction between unexcited and excited PPO molecules. The excitation energy is lost by collision, and since the self-quenching can be neglected for low PPO concentration (< 10 g/L), the light yield can thus be simplified as

$$Y = \frac{D \cdot A}{A + \frac{\lambda_i}{\lambda_a}} \quad (2-16)$$

The decay time constant τ can be described as the sum of the solute intrinsic lifetime τ_s and energy migration transfer (or “hopping”) time^[82],

$$\tau = \tau_s + \frac{A_0}{k_h A} \quad (2-17)$$

where k_h is the effective energy migration transfer rate for a given concentration A_0 . The number of energy migration transfer processes caused by solvent-solvent collisions is inverse proportional to the PPO concentration A .

Combining Eqs. (2-16) and (2-17), we can obtain the relationship between the light yield and decay time constant,

$$\tau = \tau_s - \frac{A_0 \lambda_a}{k_h \lambda_i} + \frac{A_0 \lambda_a D}{k_h \lambda_i} \cdot \frac{1}{Y} \equiv \tau_0 + \frac{C}{Y} \quad (2-18)$$

where

$$\tau_0 \equiv \tau_s - \frac{A_0 \lambda_a}{k_h \lambda_i}, \quad C \equiv \frac{A_0 \lambda_a D}{k_h \lambda_i}$$

Eq. (2-17) indicates an inverse relationship between the decay time constant τ , and the scintillation light yield Y . The relationship consistent with our measurements results in Figure. 2.13.

As shown in Table 2.2, when the concentration increases beyond 0.1 g/L, the decay time constant is less than 20 ns, so that the separation between scintillation light and Čerenkov light from the pulse shape discrimination becomes impossible. The addition of bis-MSB reduces the number of Čerenkov photons, even though it can shift the wavelength to the detectable region.

2.5 Emission spectrum

We measured the emission spectra of the samples using an Ocean Optics RTI fluorescence spectrometer excited at 260 nm. The relevant spectra are shown in Figure 2.15. LAB emits light at 280~300 nm. In a bulk solution, both absorption and re-emission occur during the light propagation process when adding PPO and bis-MSB, resulting in an upward shift in the wavelength. The transmission of acrylic is also shown in the plot (detailed in Section. 2.6). From the emission spectra, we concluded that a significant amount of additional bis-MSB should be required to shift the wave length and to reduce the propagation loss in the acrylic and let it detectable for the PMTs.

Figure 2.15 shows that the additions of 13 mg/L or more bis-MSB have similar wavelength spectra. The formulas with no bis-MSB addition have a better Čerenkov separation capability but may lead to a lower photoelectron yield. There is a trade-off between the photoelectron yield and Čerenkov separation capability. These emission spectra were implemented in the simulation for evaluating the detection efficiency in Section 2.1.2.

Combining the emission spectra with the scanning results in Table 2.2, we chose the formula of LAB with 0.07 g/L of PPO and 13 mg/L of bis-MSB as our slow liquid scintillator candidate in the 1-ton prototype neutrino detector at CJPL, since it has a reasonable

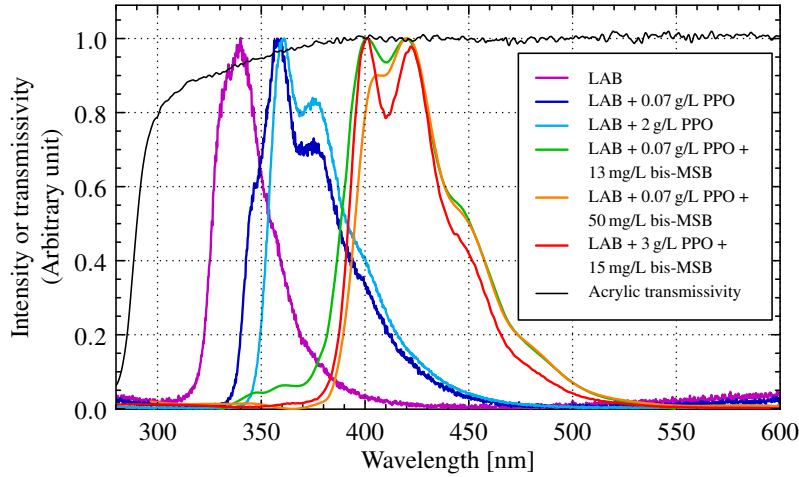


Figure 2.15 Emission spectra of the pure LAB, conventional LS (red line), and slow liquid scintillator candidates. The transmissivity of a 10-mm thick acrylic is also shown in this plot.

light yield and time constant while maintaining more than half of the Čerenkov photons for the pure LAB. The emission spectrum was shifted to the detectable range above 390 nm, falling into the detectable region with almost no optical loss in acrylics (see Section 2.6).

2.6 Optical transmission of acrylic

Since acrylics are compatible with LAB-based liquid scintillators in terms of chemical and optical properties, they are widely used for the scintillator vessels in neutrino experiments. However, to contain a kiloton-scale liquid scintillator, the acrylic vessel should be at least several centimeters thick, as used in the SNO experiment^[83]. It is, therefore, essential to have a careful study on the optical transmission loss in acrylic. To evaluate the effect, we performed a qualitative study on the transmission for a UV transparent acrylic sample. The acrylic sample was UV transparent type made by DONCHAMP, China.

Figure 2.16 shows the experiment setup, including a deuterium lamp, an Ocean Optics spectrometer, and a 10-mm-thick test sample plate in between. The lamplight was set perpendicularly incident to the acrylic plate, and the spectrometer was used to measure the transmission light. The light intensity spectra without and with the acrylic (referred to as K_0 and K_1) were measured for comparison. Figure 2.17 illustrates changes due to the acrylic transmissivity and reflectivity.

For the case of the vertical incident light, the transmission intensity should be $t(1 - r)^2 + t^3 r^2(1 - r)^2 + \dots$, and the ratio can be written as

$$\frac{K_1}{K_0} = \frac{t(1 - r)^2}{1 - t^2 r^2}. \quad (2-19)$$

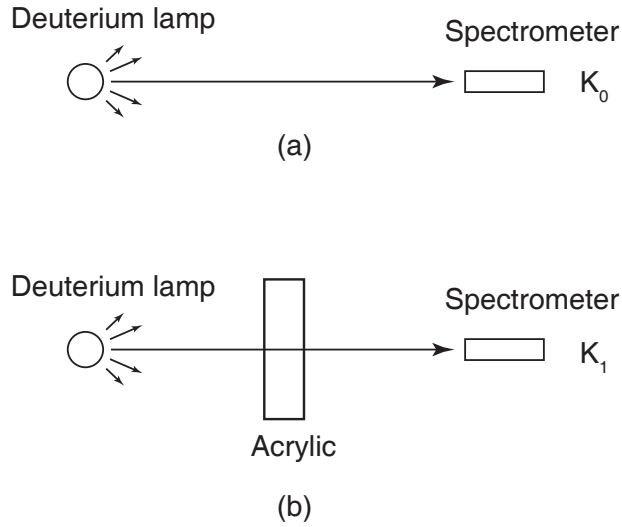


Figure 2.16 The schematic of the apparatus used for the acrylic optical transmission measurement.

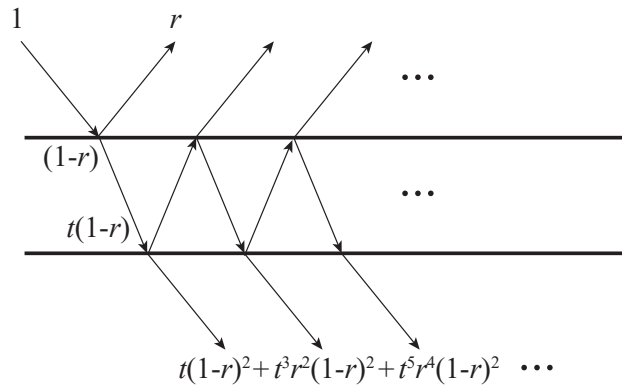


Figure 2.17 Transmissivity and reflectivity of an acrylic layer. The intensity of the incident light beam is 1, the transmissivity of the sample is t , and the reflectivity in the air is r . The light beam hits the interface at a perpendicular angle in the experiment, but in this figure, the light beams are drawn at a non-perpendicular angle to easily distinguish the incident from reflection light beams.

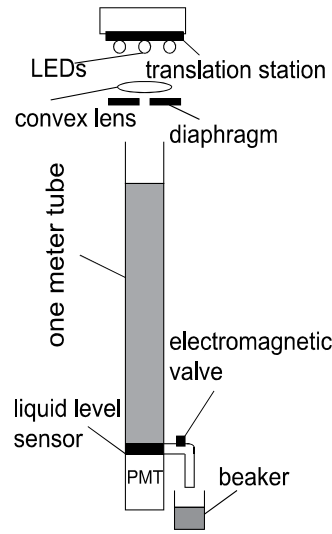


Figure 2.18 A schematic layout of the variable pathlength photometer used for attenuation length measurement.

The reflectivity r can be derived from the Fresnel formula ,

$$r = \left(\frac{n - 1}{n + 1} \right)^2 . \quad (2-20)$$

where n is the reflective index. The curve of transmissivity as a function of the wavelength obtained from Eqs. (2-19) and (2-20) is shown in Figure. 2.15. The acrylic sample was found to be nearly transparent in the visible light wavelength range (i.e., > 400 nm) and became almost opaque in the wavelength range below 270 nm. As shown in Figure. 2.15, the spectrum of emission light for the pure LAB was below 400 nm and should be shifted upward to avoid the absorption in acrylics.

2.7 Attenuation length measurement

If all the chemical components in the scintillator were precisely known, the attenuation length might have been easily obtained using Eq. (2-3). Given that the impurity of the sample is difficult to know, we used a photometer to measure the attenuation of the slow liquid scintillator candidates^[84-85]. Figure 2.18 shows a schematic layout of this photometer.

An LED lamp was mounted at the top of the photometer. The light was refocused from a lens to ensure it to travel through a diaphragm and a 1 m-long stainless steel pipe filled with the liquid scintillator. A solenoid valve and a liquid level sensor controlled the liquid level in the pipe. A PMT (Hamamatsu R7724, 51 mm diameter) was installed at the

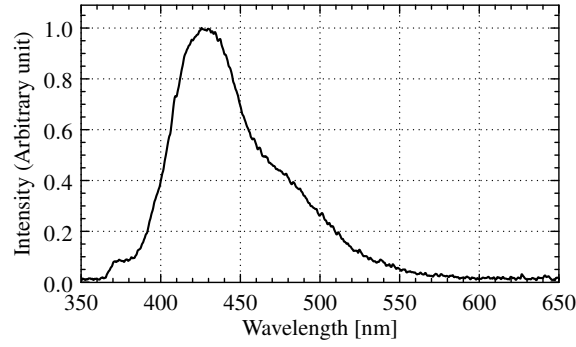


Figure 2.19 The emission spectrum of the LED mounted at the top. The central peak is 430 nm.

bottom of the equipment to receive light, and the wavelength of the response displayed a maximum at 420 nm^[86].

The slow liquid scintillator used in the measurement was LAB with 0.07 g/L of PPO and 13 mg/L of bis-MSB, which had an emission spectrum that partially overlapped with that of the LED light used in the experiment.

As shown in Figure. 2.19, the LED spectrum is not monochromatic, so the light attenuation cannot be described by a simple exponentially decreasing curve. Instead, the intensity of transmission light $I(x)$ is described by a weighted average of the LED spectrum $f(\lambda)$,

$$I(x) = I_0 \int f(\lambda) e^{-x/L(\lambda)} d\lambda \quad (2-21)$$

where I_0 is the intensity of incident light. The integral (2-21) is difficult to be used as a fitting function because $f(\lambda)$ and $L(\lambda)$ are complicated spectra. We, therefore, used an approximation by a sum,

$$I(x) \approx \sum_i f_i e^{-x/L_i} \Delta\lambda_i \equiv \sum_i \alpha e^{-x/L_i} \quad (2-22)$$

The spectrum of LED light and liquid scintillator are similar. Our prototype's scale is small enough, so the approximation down to the second order is enough to describe the data,

$$I(x) = I_0 [\alpha e^{-x/L_1} + (1 - \alpha) e^{-x/L_2}] \quad (2-23)$$

where α is the fraction of the component with a longer attenuation length (referred to as L_1), while L_2 is the shorter attenuation length. Figure 2.20 shows the fit result, $\alpha = 0.925 \pm 0.003$, $L_1 = (9.37 \pm 0.44)$ m, $L_2 = (0.16 \pm 0.02)$ m. We observed that the longer attenuation length component is much larger than the shorter one.

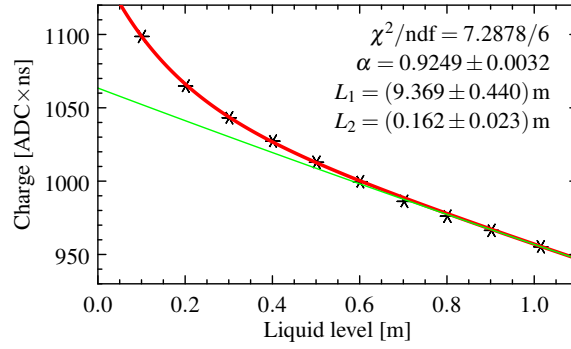


Figure 2.20 Two-exponential fitting results of LAB with 0.07 g/L PPO and 13 mg/L bis-MSB. The green line reflects the long attenuation length component.

It should be noted that the measured attenuation lengths included the contribution from the absorption, re-emission, and scattering effects^[87-88]. We expect that with a purification process, the attenuation length can be extended to 15~20 m^[89].

2.8 Performance evaluation for kiloton scale neutrino detector

In this section, we discuss the performance of the slow liquid scintillator in a kiloton scale neutrino detector by a simulation study. This simulation was performed by JSAP (Jinping Simulation and Analysis Package), which will be introduced in Chapter 3.

Figure 2.21 shows the detector model, which is similar to the Borexino and SNO+^[90] detectors. The height and diameter of the water tank were both 30 m. The target material was slow liquid scintillator (LAB + 0.07 g/L PPO + 13 mg/L bis-MSB.), filled in an acrylic inner vessel (14.62 m inner radius). The attenuation length was set to be 20 m for the wavelength greater than 400 nm. The fiducial mass was 5000 tons. Totally 8607 20-inch PMTs were placed around the inner vessel in the buffer water. The cathode coverage was 72%, and the quantum efficiency at 390 nm is 35%. The simulation result shows that the photoelectron yield was 440 PE/MeV, or 4.8% at 1 MeV energy deposit.

To evaluate the direction resolution, we simulated 2 MeV electron events in the center of the detector. The reconstruction method used a maximum likelihood estimation (MLE). The log-likelihood function is

$$\log \mathcal{L}(n_i, t_{ij}) = \sum_{i=1}^N \log P_i^C + \sum_{i=1}^N \sum_{j=1}^{n_i} \log P_{ij}^T \quad (2-24)$$

where

- N is the total number of PMTs, $i = 1, 2, \dots, N$ represents the PMT index.
- n_i is the PE number of PMT i .

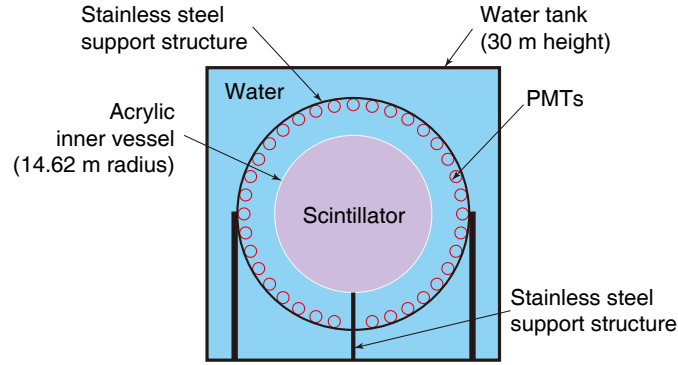


Figure 2.21 A typical solar neutrino observatory with 5 kilotons of fiducial mass.

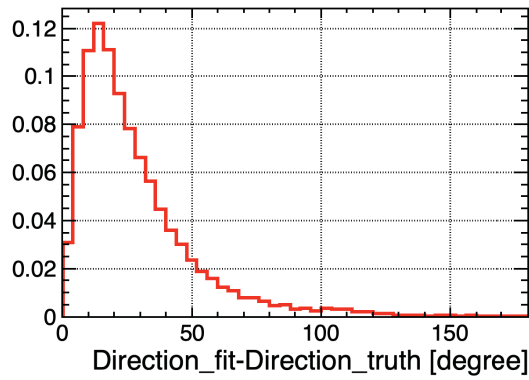


Figure 2.22 The distribution of the angle between the true value of the electron direction and the reconstruction result.

- $j = 1, 2, \dots, n_i$ is the PE index of PMT i .
- t_{ij} is the arrival time of PE_{ij} .
- P_i^C is the probability density function of PMT i detecting n_i PEs.
- P_{ij}^T is the probability density function of arrival time of PE_{ij} .

Figure 2.22 gives the distribution of Θ , which is the angle between the true value of the electron direction and the reconstruction result. We found 97% of events with $\Theta < 90^\circ$. This reconstruction method is a simple demonstration. For a real detector, the reconstruction is more complicated and challenging. Related research is under study.

2.9 Summary

The liquid scintillator technique is a key technology element for MeV-scale neutrino experiments. In this chapter, we present our studies on the properties of LAB-based slow liquid scintillators. Although the high concentration solution of PPO and bis-MSB in LAB has been widely applied in current neutrino experiments, the low concentration so-

lutions show very different properties, giving the power to distinguish Čerenkov light and scintillation. The inverse relationship between the scintillation light yield and the decay time constant indicates a balance between the energy and direction resolutions. The measurements of emission spectra, attenuation length, and acrylic transmissivity also provide essential parameters in optimizing the design of MeV-scale neutrino detectors. Finally, the simulation of low-energy electron events in a kiloton scale neutrino detector demonstrates the power of direction reconstruction in slow liquid scintillators. The full reconstruction method needs studying in the future.

Chapter 3 Development of Simulation Framework

Detector simulation and data analysis pipeline are essential for carrying on the R&D study for MeV-scale neutrino experiments. This thesis developed a general simulation and analysis framework on Linux. This framework is lightweight and developed on the platform of ROOT and Geant4, with a flexible geometry and customized physics processes, and an additional radioactive decay database. A streamed trigger mechanism is applied to emulate the background coincidence and electronic trigger system in the real world. Using the established standard data analysis pipeline in this package, one can access and analyze the data, even for beginners.

Figure 3.1 illustrates the directory structure of this framework.

```

JSAP/
├─ Analysis/
├─ CommonLib/
├─ DataType/
├─ DetectorStructure/
├─ EventDisplay/
├─ Generator/
├─ Simulation/

```

Figure 3.1 The directory structure of JSAP.

`Analysis/` The data analysis framework. Many analysis scripts and utilities can be found here.

`CommonLib/` The shared libraries used in the simulation and analysis, such as the timestamp library.

`DataType/` The definition of the output file structure. We used the ROOT file as the output of the simulation and analysis. A ROOT file has some branches, whose names and types can be found here.

`DetectorStructure/` The detector definition for simulation and data analysis.

`EventDisplay/` The event display programs for real data or simulation.

`Generator/` The radioactive decay database and the interface to read the database.

`Simulation/` A typical Geant4 application for Monte-Carlo simulation.

3.1 Overview of simulation

Monte-Carlo (MC) simulation can be used to determine the detection efficiency and to model backgrounds. Figure 3.2 shows the simulation flow chart of a proposed MeV-scale neutrino experiment at CJPL.

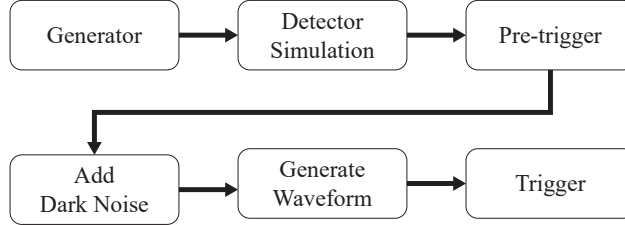


Figure 3.2 The simulation flow chart of a proposed MeV-scale neutrino experiment at CJPL.

Generator The generator creates a primary particle in the simulation and produces its position, time, momentum, and energy. For neutrino interactions, the generator only starts from the secondary particles. To study the backgrounds, we also generate the radioactive decay product: alpha, beta, and gamma rays. The generator provides the input of the full detector simulation.

Detector simulation The package takes the input from the physics generator, the detailed geometry, material, and electronics description of the detector, and simulates the detector's response. The output is the photoelectron hit information with track and energy loss recorded.

Pre-trigger Since the complete electronics simulation consumes much CPU time, the pre-trigger system uses criteria to rapidly decide which events should be recorded and speed-up the simulation process.

Dark noise The dark noise is caused by thermal electron emission on the PMT photocathode, leading to an equivalent photoelectron signal.

Waveform generation In this stage, the input is the photoelectron hit information, including the time, PMT number, PE type, etc. We convoluted these photoelectrons with the single photoelectron response of the corresponding PMT. The output is the waveform, the same as the actual experimental data.

Trigger Compared with the pre-trigger stage, this stage assimilates and synchronizes information from the raw waveforms, checks the trigger condition, issues a trigger when an event meets the requirement and packages the entire event.

3.2 Detector definition

The detector definition requires the geometry setup and electronics properties for a neutrino detector, the visualization attributes and other user-defined properties. The geometry setup focuses on the shape, material, and spatial position of a solid model in the detector, i.e., the logical relations to one another, such as containment. The electronics properties define the waveform and trigger parameters of PMTs, such as the quantum efficiency, single PE waveform, trigger multiplicity, etc.

3.2.1 Introduction of GDML

The conventional method to define the detector geometry is to dynamically allocate volumes, solids, and materials using C++ `new` operator in user codes. The developer may pre-define some parametrized base classes for describing the shape of volumes (such as water tank, acrylic vessel, PMT). The users could create derived classes and change the size and position of different volumes.

The geometry of the neutrino detector at CJPL is still under optimization. The conventional method to define the detector geometry is not flexible enough for our application. In JSAP, we used GDML (Geometry Description Markup Language) to construct the geometry. GDML has been applied in some neutrino experiments, such as Dayabay and JUNO. GDML is a markup language based on XML. It is designed to describe and exchange geometries of the detector between different applications. It is based on the concept of “geometry trees”, i.e., the hierarchy relationship of volumes in a detector. The position and material of individual solids can also be described. A GDML file is a pure XML file, which is human-readable and universally used among different applications.

Unlike the method of defining geometry in the C++ codes, the users are free to create various volumes using GDML and are not restricted by the base class. GDML can also describe the electronics and other non-geometrical detector definitions. Another advantage is that there’s no need to re-compile the program when changing the geometry, which may consume much CPU time for compiling a sophisticated C++ program.

A set of XML Schema Definition (XSD) files defines the the structure of a GDML

file. The general structure of the GDML file is divided into five parts:

1. `<define> ... </define>` defines numerical values used in the geometry construction.
2. `<materials> ...</materials>` defines the materials.
3. `<solids> ... </solids>` defines the shapes of solid.
4. `<structure> ... </structure>` defines the geometry tree. The assignment of a solid and material makes up a logical volume. The hierarchy of volumes defines the physical volumes in Geant4.
5. `<setup> ... </setup>` specifies the top volume of the geometry tree.

A GDML file can be split into several files. These files are not standalone, as a macro replacement in the main GDML file. These files can be combined together by using the `ENTITY` statement. The material and PMT setup are split into different files by `ENTITY`.

The geometry can also be defined in several standalone GDML files, each one representing an independent module. Each GDML file only contains the materials, the solids, and the volumes of this module. The PMT volumes are modularized in a standalone GDML file.

3.2.2 Detector hierarchy in JSAP

All the detector definitions are in the `DetectorStructure/` directory. An example of a 1-kiloton detector definition is shown in Figure 3.3.

```
DetectorStructure/
├── materials/
├── PMTlib/
├── 1kt_sphere/
│   ├── main.gdml
│   ├── PMT_Gain.xml
│   ├── PMT_Position.xml
│   └── Trigger_Params.xml
```

Figure 3.3 The directory structure of JSAP.

`materials/` and `PMTlib/` are public components that can be used in other detectors such as the 1-ton prototype. The simulation module of JSAP reads `main.gdml` as the entrance of the geometry definition. This file defines the general structure and geometry tree of the detector. For a liquid scintillator neutrino detector, many PMTs are

essential; the optional components for managing the PMTs are inserted in `main.gdml` via `ENTITY` statement:

- `PMT_Position.xml` defines the position of PMT.
- `PMT_Gain.xml` defines PMT gain and dark noise rate.
- `Trigger_Params.xml` defines the electronics of the detector, such as the time window and trigger condition.

3.2.3 Materials

In the `DetectorStructure/materials/` directory, JSAP provides some materials commonly used in neutrino detectors, such as water, acrylic, stainless steel, and liquid scintillator, etc. One can also define customized materials using the standard GDML syntax. The element formula and density are required.

For a transparent material, several properties are essential for the optical simulation: the refractive index, the absorption length, the Rayleigh scattering length, and the Mie scattering length. These properties may vary with the wavelength of light.

The liquid scintillator is the key material of the Jinping Neutrino Experiment. The input properties in the simulation include:

- Formula and density.
- Common properties of transparent materials: refractive index, absorption length, Rayleigh scattering length, and Mie scattering length.
- Light yield.
- Time profile: rise time constant and decay time constant.
- Scintillation spectrum of fast and slow components.
- Yield ratio of fast and slow component.
- Birks' constant.
- Scintillation resolution scale. A Gaussian-distributed number of photons is generated according to the energy loss during the step in Geant4. A resolution scale of 1.0 produces a Poisson-like statistical fluctuation, which will be broadened for those with scale greater than 1. A value of zero gives no fluctuation.

3.2.4 PMT

The shape and electronics parameters of a PMT are also imported in the simulation by means of GDML. Several PMT models are pre-defined in

`DetectorStructure/PMTlib/` directory. Two files are needed to define a PMT: (1) the geometry description (such as `Hamamatsu_R5912_Geo.gdml`); (2) the electronics parameters (such as `Hamamatsu_R5912_Elec.xml`).

The PMT surface is usually a thin shell of revolution. We input the PMT profile curve in the form of discrete points with (r, z) coordinates. The GDML Generic Polycone rotates the curve around the axis of revolution $r = 0$ and generates the shape of PMT, as shown in Figure 3.4. A logical volume named “CathodeLog” is required in the geometry definition. This volume is the photocathode for generating photoelectrons in the simulation.

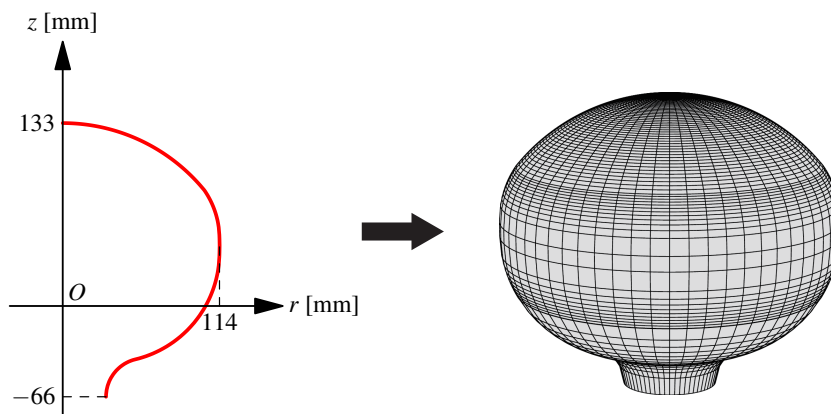


Figure 3.4 The curve of PMT profile and its revolution imported in JSAP.

The electronics parameters defined in `Hamamatsu_R5912_Elec.xml` describe a PMT model’s standard parameters, such as the transit time, transit time spread, quantum efficiency curve, time constants of the waveform, etc.

Two ways define the the position and rotation of PMTs. One is to use the GDML modules function, and the other is to treat the PMT volume as a physical volume directly, as shown in Listing 3.1.

Listing 3.1 The position and rotation of PMTs defined by GDML modules.

```
<physvol name="PMT_0">
  <file name="../PMTlib/Hamamatsu_R5912/
    Hamamatsu_R5912_Geo.gdml"/>
  <position x="0.428" y="0.139" z="0.700" unit="m"/>
  <rotation x="-168.757" y="30.9399 " z="0" unit="deg"/>
</physvol>
```

This method is very flexible in a small detector simulation. However, in a large neutrino detector simulation, there are thousands of PMTs, and the GDML file has an

incredibly large size. It consumes too much time to read and parser the GDML file. In this situation, we used an internal PMT arrangement routine. For example, in a spherical detector, if turning on this mode by defining a variable named `AutoPMT`, the position of PMTs is controlled by two parameters, as shown in Listing 3.2,

- The distance between PMT center and detector center, notated as R .
- The distance between two adjacent PMTs, notated as d .

Listing 3.2 Define the position and rotation of PMTs by internal PMT arrangement routine.

```
<define>
  <variable name="AutoPMT" value="1"/>
  <quantity name="PmtCenterR" value="14.38" unit="m" />
  <quantity name="PmtCenterDist" value="26*1.05*2"
    unit="cm" />
</define>
```

The PMTs are arranged in N rings in z direction,

$$N = \left\lfloor \frac{\pi R}{d} \right\rfloor \quad (3-1)$$

For the i -th ring ($i = 0, 1, \dots, N - 1$), the z coordinate is

$$z = R \cos \frac{i}{N} \pi \quad (3-2)$$

and N_i PMTs are arranged in a circle with a radius of r_i at z ,

$$r_i = R \sin \frac{i}{N} \pi, \quad N_i = \left\lfloor \frac{2\pi r_i}{d} \right\rfloor, \quad (3-3)$$

The x, y coordinates are

$$x = r_i \cos \frac{2\pi j}{N_i}, \quad y = r_i \sin \frac{2\pi j}{N_i}, \quad j = 0, 1, \dots, N_i - 1 \quad (3-4)$$

3.2.5 GDML parser

In the GDML files of the detector definition, some blocks and attributes such as Birks' constant and PMT electronics parameters are not included in the standard GDML parser in Geant4. We developed the parser to read in these attributes. The framework provides an interface for reading GDML in `Simulation/DataIOModule/`. The class `JPSimGDMLReader`, which is derived from `G4GDMLReadStructure`, is the

main parser in the detector construction. We also rewrote some Geant4 internal geometry parsers in `JPSimG4GDMLCustom.cc` to enhance the function.

3.3 Physics processes

Physics processes describe how particles interact with materials. In the simulation, the electromagnetic and optical processes are the most interested. Besides, the fast neutron is one of the critical backgrounds and should be treated carefully in the simulation.

The modular management of physical processes in the JSAP simulation module is achieved by the `JPSimPhysicsList` class, which can be found in `/Simulation/PhysicsListModule/`. This class is derived from `G4VModularPhysicsList`. One can turn on/off or insert a customized physics list in this class.

All particles are constructed in the `ConstructParticle()` function of `JPSimPhysicsList`. All physics processes are registered explicitly in the construction function of this class, including

- Standard electromagnetic process.
- Decay.
- Optical process.
- Hadron elastic and inelastic scattering.
- Ion Elastic scattering.
- Neutron physics.

All these processes can be the Geant4 pre-defined or user customized classes. We customized optical and neutron physics. Other processes can also be customized if needed.

3.3.1 Optical processes

In Geant4, optical photons are treated as a class of particles distinct from their higher energy gamma cousins. `JPSimOpticalPhysics` derived from `G4OpticalPhysics` manages the optical processes. The Geant4 catalog of optical processes includes refraction and reflection at medium boundaries, bulk absorption, Mie and Rayleigh scattering. Processes that produce optical photons include the Čerenkov effect and scintillation. `JPSimOpticalPhysics::ConstructProcess()` constructs all these processes.

The light yield of the liquid scintillator is in the order of $10^3 \sim 10^4$ photons/MeV. It

consumes too much time if we simulate each photon. We reduced the light yield from Y to $Q \cdot Y$ in the scintillation and Čerenkov process, where Q is the maximum value of PMT quantum efficiency. Accordingly, the quantum efficiency is increased by $1/Q$ to conserve the number of photoelectrons. For a typical PMT, $Q \approx 0.25$, this optimization reduces the optical photon simulation time by 75%.

3.3.2 Neutron physics

Nuclear models are still not perfect in predicting nuclear cross-sections of neutrons. Thus, all physical quantities relevant for an accurate model of nuclear reactions in Monte-Carlo simulations should be provided as a database. This database should include cross-sections, angular distributions of the emitted particles, and other interesting data. For the case of neutron-induced reactions, such databases are called “evaluated data”. They contain recommended values for different quantities that rely on compilations of experimental nuclear data. These data are usually completed with theoretical predictions, benchmarked against available experimental data (i.e., integral and differential experiments). It should be noticed that the information available varies from isotope to isotope and can be incomplete or missing.

The G4NeutronHP package in Geant4 allows using evaluated nuclear data libraries in the G4NDL format. Any simulation involving neutrons with energies below 20 MeV and not using the G4NeutronHP package can lead to unreliable results. The simulation module of JSAP imports the G4NeutronHP package and corresponding evaluated nuclear data libraries. An object of the `NeutronHPphysics` class is registered in the physics list, implementing the elastic, inelastic, neutron capture, and fission process.

Fast neutrons can be detected through the reaction of neutron capture. Hydrogen or gadolinium (if the scintillator doped with gadolinium) nucleus captures a neutron and emits one or more characteristic gamma rays. The energy and branching ratio were not precise in the Geant4 database, so we customized the neutron capture process. The energy and number of gamma rays were taken from the Daya Bay database.

3.4 Generator

We rewrote the generator of radioactive decay in a standard Geant4 application. Radioactive isotopes are the main backgrounds for the MeV-scale neutrino experiment at CJPL. There are four series of radioactive decays (decay chain): thorium series ($4n$), nep-

tanium series ($4n + 1$), uranium series ($4n + 2$) and actinium series ($4n + 3$). Three of them (except neptunium series) exist in nature. The isotopes in the three series can be detected in many materials, especially in metal. Many serious backgrounds such as ^{214}Bi , ^{210}Bi , ^{208}Tl are in the decay chains. The secular equilibrium is achieved in a decay chain, so each isotope in this decay chain has the same radioactivity. The total activity can be estimated from the abundance of U/Th.

Another important radioactive background not in the decay chains is ^{40}K . Potassium exists in detector materials; the natural abundance of ^{40}K is 0.0117%. This isotope undergoes β^- decay and electron capture. About 89% ^{40}K decay to ^{40}Ca via β^- decay with a maximum energy of 1.31 MeV for the emitting electron. The rest 11% goes to ^{40}Ar via electron capture (EC), emitting a 1.46 MeV gamma ray.

The energies and branching ratios for some isotope decays were not accurate in the Geant4 database. The calculation of the beta energy spectrum in Geant4 did not include correction terms such as screening correction, finite-size correction, and weak magnetism correction. In order to get a more precise simulation, we created a database to save the decay information. We also wrote codes to calculate the shape of the beta spectrum, including all the correction terms mentioned below. The decay data was from the National Nuclear Data Center, Brookhaven National Laboratory. Each decay branch has these fields below,

- Q-value.
- Branching ratio.
- Spin and parity difference between the daughter nucleus and its parent nucleus.
- Number of gamma rays.
- The energy of each gamma ray.

We provided an interface `DecaySpec` to load the database and sample the energy of alpha, beta, gamma rays. When an isotope was specified, the program selected a decay mode randomly depending on the branching ratio. If an alpha decay was chosen, the program gave a monoenergetic alpha particle. If a beta decay was chosen, the program calculated the beta spectrum and sampled energy from this spectrum. Also generated were gamma rays of this alpha or beta decay. Finally, the generator output the sampled kinetic energies for alpha, beta and gammas.

In a Geant4 application, the actual generation of primary particles is done by a concrete class of `G4VPrimaryGenerator`. Geant4 provides three concrete classes:

- `G4ParticleGun`
- `G4GeneralParticleSource`
- `G4HEPEvtInterface`

`G4GeneralParticleSource` (GPS) is suitable for a sophisticated manner and provides a macro command interface. A macro file can control the generation of primary particles. We rewrote `G4GeneralParticleSource` to `ExGeneralParticleSource` to support the customized radioactive decay generator. A corresponding messenger class, `ExGeneralParticleSourceMessenger`, is used for parsing the macro file. An example of a macro file is shown in Listing 3.3.

Listing 3.3 An example of macro file as the input of the generator.

```
/gps/pos/type Volume
/gps/pos/shape Sphere
/gps/pos/centre 0. 0. 0. m
/gps/pos/radius 0.7 m
/gps/pos/confine ScintillatorLog_PV
/gps/ang/type iso

/gps/source/add 5
/gps/rad Bi214
/gps/radZA 83 214

/gps/event/add 1
/gps/rad Po214
/gps/radZA 84 214
/gps/tim/type Exp
/gps/tim/tzero 237.03 us

/run/beamOn 100
```

In this macro file, we first specify the volume where the primary particles are placed. The GDML messenger supports a regular geometry such as a sphere and also a physical volume in the detector geometry definition by the `/gps/confine` command. The standard GPS uses the acceptance-rejection method to sample in a physical volume. In this method, we first sample the vertex in a regular geometry and then reject it if it is not

in the physical volume. This method is inefficient when the physical volume is a thin shell, or the physical volumes are distributed in a thin shell (like PMTs). The standard GPS does not support spherical shell as a regular geometry, so we add it to increase the sampling efficiency.

Then radioactive isotopes are specified. If one isotope has a short half-life, the time correlation of this cascade decay can also be implemented. The GPS class reads the isotopes in the macro file, samples energy from `DecaySpec`, and randomly gives the position and momentum direction.

3.5 Simulation and trigger process

The streamed trigger system imitates the trigger mechanism in the real world. It is conducive to handle the mix of radioactive decay backgrounds. Comparing to a conventional event mixing method, we mix the primary particles at the beginning of the generator.

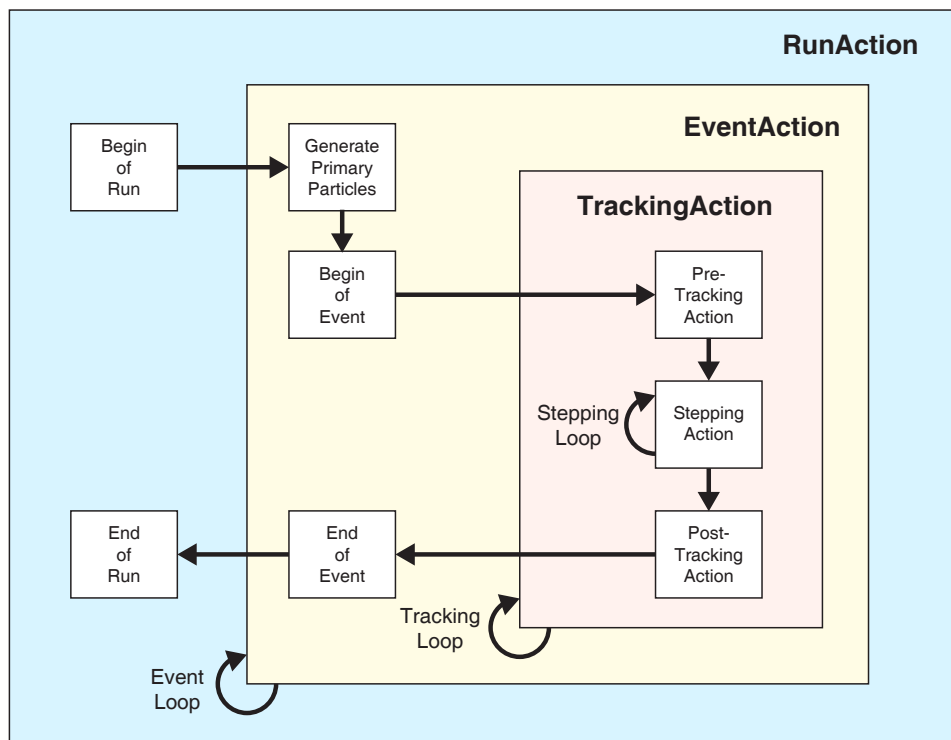


Figure 3.5 Event loop in a Geant4 simulation application.

3.5.1 Detector simulation

Figure 3.5 shows the typical event loop in a Geant4 simulation application. The “event” loop in Geant4 is transformed into a concept of “segment”. The time is divided into several “segments”. Usually, one segment equals one second. All the primary particles in one segment are simulated in an “event” loop in Geant4. A primary particle can be identified by a pair of integer: segment ID and particle ID. For instance, if the activity of a beta source is 5 Bq, the number of electrons N is generated in one segment according to Poisson statistics with a mean value of 5. Every electron has its particle ID, global timestamp, position, energy, and momentum. The global timestamp is a pair of integer: second and nanosecond. All the primary particles in this segment are generated and sent to the detector simulation. In some cases, such as a cascade decay, a delayed particle may be generated in the next segment. The simulation code will transfer this particle to a buffer and process it in the next segment.

The JSAP simulated these particles one by one in the tracking loop. Like a standard Geant4 application, the JSAP handled trajectory information in the `SteppingAction` class. The trajectory was saved as all the step points, including the position, time, process type, and track ID. The photoelectron hit information was processed in the `TrackingAction` class. When an optical photon hit the photocathode of a PMT and was killed, we determined whether this photon was converted to a photoelectron based on a sampling of quantum efficiency. The photoelectron hit information was stored in a map:

```
std::map<int, std::vector<JPSimHit> >
```

The key of this map is the PMT ID and the value of the map is a list of photoelectron information, including hit time, wavelength, PE type (0 for Čerenkov or 1 for scintillation, -1 for others), and primary particle ID.

3.5.2 Electronics simulation

The `EventAction` class handled the electronics triggers, while the function of `EndOfEventAction()` executed the next pre-trigger, dark noise, pulse shape, and trigger procedure sequentially. The pre-trigger routine scanned the photo-electron’s hit time and found the time intervals containing sufficient photoelectrons and output these intervals. Also added were “fake” triggers caused by the PMT dark noise. Let us suppose a detector to have N PMTs, and each PMT has dark noise rate f Hz, the multiplicity trigger

threshold is m PMTs, the coincidence time window is τ ns, the dark noise coincidence rate R can be calculated by

$$R = \frac{1}{\tau} \sum_{i=m}^N \binom{N}{i} (f\tau)^i (1 - f\tau)^{N-i} \quad (3-5)$$

For example, in the 1-ton prototype detector, $N = 30$, $m = 10$, $f = 5$ kHz, $\tau = 125$ ns, $R = 2.7 \times 10^{-25}$ Hz. In the case of a large neutrino detector, $N = 8000$, $m = 100$, $f = 10$ kHz, $\tau = 250$ ns, $R = 2.3 \times 10^{-37}$ Hz. Usually, the dark noise coincidence rate is quite low, so no false triggers are added.

Dark noise hits were added in the time intervals given by the pre-trigger. A dark noise hit is just like a single photoelectron, but the PE type is -1 (dark noise). The photoelectron number and the hit time in the interval were sampled from a Poisson distribution and a uniform distribution, respectively.

All the photoelectrons in the time intervals were convoluted with the single photoelectron pulse shape to generate waveforms. Also considered was the fluctuation of single PE charge and baseline, as shown in Figure 3.6.

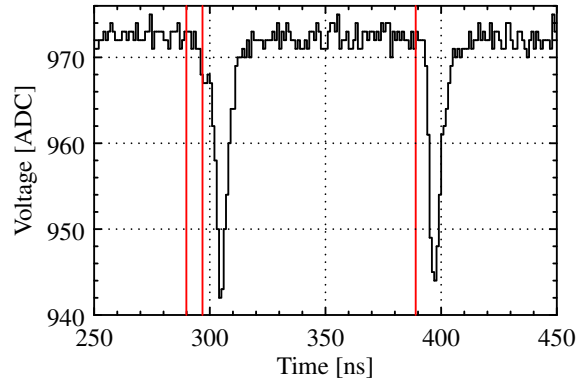


Figure 3.6 An example of simulated waveform. The red lines are the time of photoelectrons.

These raw waveforms were sent to the trigger routine for the final event assembly. As shown in Figure 3.7 for the trigger logic, each channel has a generated over-threshold logical signal, all of which are then summed to find the trigger time whenever the multiplicity threshold is satisfied. The waveforms before and after the trigger time were used to assemble an event.

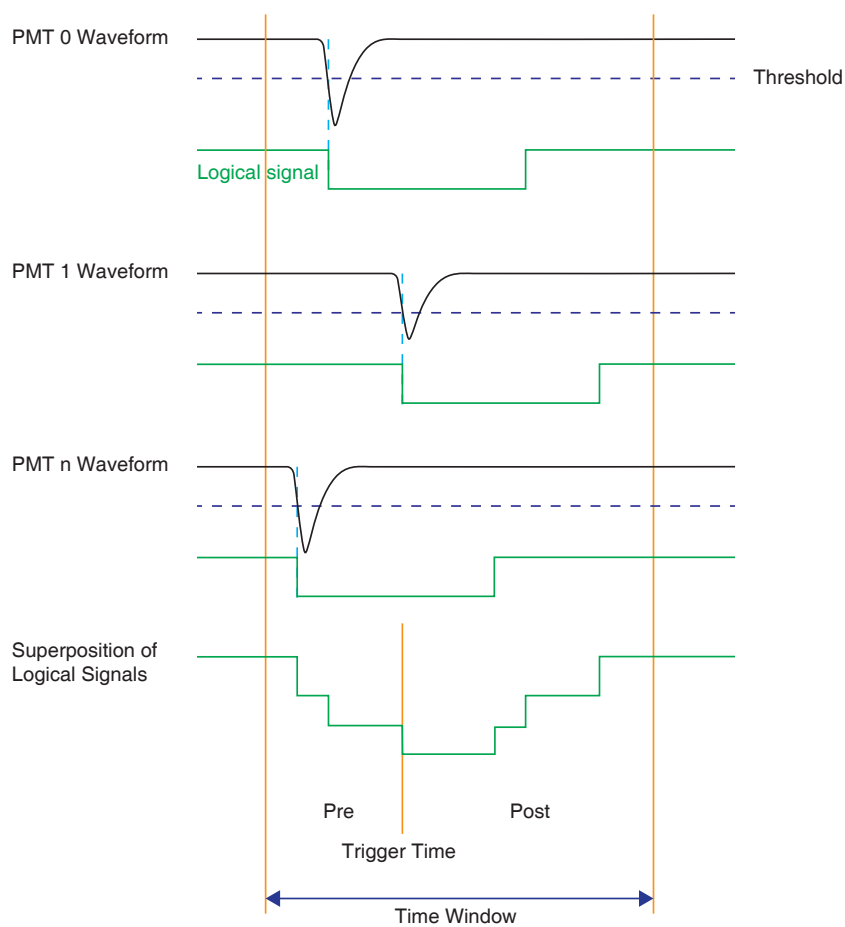


Figure 3.7 The trigger system in the JSAP.

```

Output.root
├─ Readout
├─ SimTruth
├─ SimTriggerInfo
│   └─ PEList
│       └─ truthList
    
```

Figure 3.8 The structure of the output file.

3.6 Output file format

The standard output provided a ROOT I/O interface. The file structure definition can be found in `DataType/JPSimOutput.hh`. As shown in Figure 3.8, there were three branches in an output file: `SimTruth`, `SimTriggerInfo` and `Readout`. The `Readout` branch contained the waveform the same with the 1-ton prototype, as described in Section 4.3.4. The branch `SimTruth` contained the generator information. The `SimTriggerInfo` contained the information of tracks and PEs of each trigger. There were two sub-branches in `SimTriggerInfo`: `PEList` and `truthList`. The former one `PEList` stored the information of each PE, including vertex ID, PMT ID, position, time, charge. There were many fields about the PE time. We found that the fine time structure of PEs is crucial in the full vertex reconstruction. The scintillation time profile convoluted with the PMT time response cannot be simplified as a Gaussian distribution, resulting in a more complicated reconstruction algorithm. The time of PEs in each stage was needed to study the reconstruction algorithm. The saved time information of a PE was on several levels:

- `dETime` is the time of a primary particle depositing energy.
- `photonTime` is the time of an optical photon emitting. The slow liquid scintillator has a large decay time constant, so `photonTime` is significantly behind `dETime`.
- `HitTime` is the time of the photon hitting on the photocathode of a PMT. The time of flight is added in this stage.
- `PulseTime` includes TT and TTS comparing to `HitTime`.
- `PESec`, `PENanoSec`, `PESubNanoSec` add the initial global timestamp of the primary vertex comparing to `PulseTime`.
- `HitPosInWindow` is the PE time in the trigger window. All the stages above are included.

The information of the primary particle and corresponding trajectories is saved in `truthList`. For optical photons, only the trajectories of detected photons are kept to save the disk space. A trajectory is saved by its step point containing the physical process, position, time, momentum, energy, and energy deposit. The physical process is numbered by a pair of integers: process type and process sub-type.

3.7 Summary

The general simulation framework was developed for the MeV-scale neutrino experiment at CJPL. The main features are:

- Simple dependencies, easy to compile, build, and install.
- Scalable geometry setup, which is convenient for quantitative estimation of the experimental sensitivity under different geometric constraints.
- Customized physics list for high precision simulation.
- Streamed trigger system. The physical signal and the backgrounds can be processed simultaneously, which is convenient for simulating the influence of radioactive background and dark noise on the experiment.

Chapter 4 Design and Construction of the 1-ton Prototype

We built a 1-ton prototype detector at CJPL-I in 2017. The detector's motivations were to test the performance of the slow liquid scintillator, identify and measure the backgrounds. In this chapter, we introduce the 1-ton prototype details, including the detector structure, electronics trigger, and data acquisition (DAQ) system.

4.1 Detector structure

The available space constrained the geometry of this prototype detector at CJPL-I. The final target mass was decided as a one-ton scale.

4.1.1 Structural design

The prototype detector is placed in the experiment hall of CJPL-I, with a lead brick shielding. Figure 4.1 draws the structural scheme of the detector. The detector is mainly composed of the stainless steel tank, acrylic vessel, 30 PMTs, and other components.

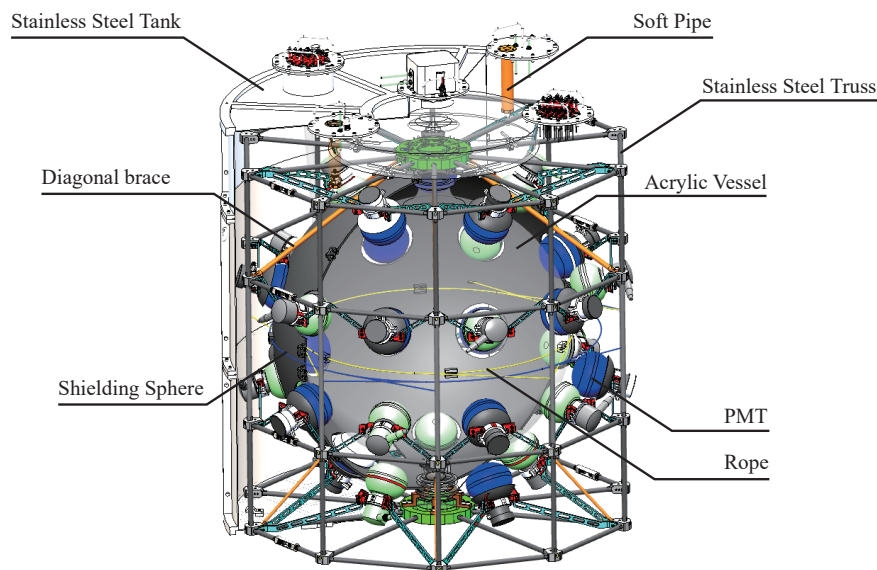


Figure 4.1 Structural scheme of of 1-ton prototype.

The height of the stainless steel tank is 2090 mm, the diameter is 2000 mm, and the thickness is 4 mm. For the convenience of installation, the tank is divided into three parts. The heights equal to 470 mm, 800 mm, and 820 mm from top to bottom. There are five

filling holes on top of the tank. The middle one is set for filling liquid scintillator in the acrylic vessel. Two of the others are reserved for the cables of the PMTs. The last two holes are used to fill the tank.

Figure 4.2 illustrates the shape of the acrylic vessel, with three parts connected through bulk polymerization: sphere, chimney, and overflow tank. The inner radius of the sphere is 645 mm, and the thickness is 20 mm. The chimney is a cylinder for filling, has an inner radius of 40 mm, and a thickness of 35 mm. The overflow tank prevents the spillover of the liquid caused by the temperature variation. The liquid outside the acrylic vessel is purified water.

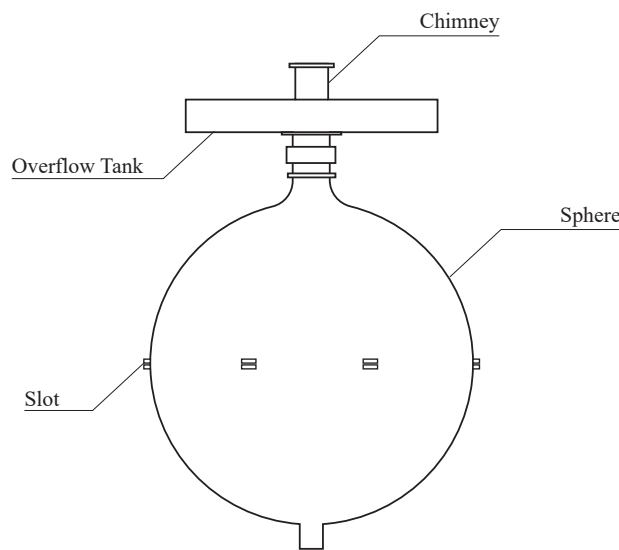


Figure 4.2 The shape of the acrylic vessel.

In the water phase, the acrylic vessel was filled with pure water. Now in the liquid scintillator phase, the acrylic vessel is filled with the LAB based slow liquid scintillator. The formula of the scintillator is linear alkylbenzene (LAB) solution doped with 0.07 g/l of the fluor 2,5-diphenyloxazole (PPO), and 13 mg/l of the wavelength shifter 1,4-bis (2-methylstyryl)-benzene (bis-MSB). The liquid circulation system is achieved by a soft pipe connected with the bottom of the acrylic vessel.

We twined three ropes around the sphere through slots on the equator to fix the acrylic sphere in the horizontal direction. As shown in Figure 4.3, both ends of these ropes are fixed on the stainless steel truss.

There is a shielding sphere made of black acrylic between the acrylic vessel and stainless steel truss. The thickness is 10 mm. It is used to suppress the radioactive background from stainless steel materials in the inner tank and the light leakage from outside.

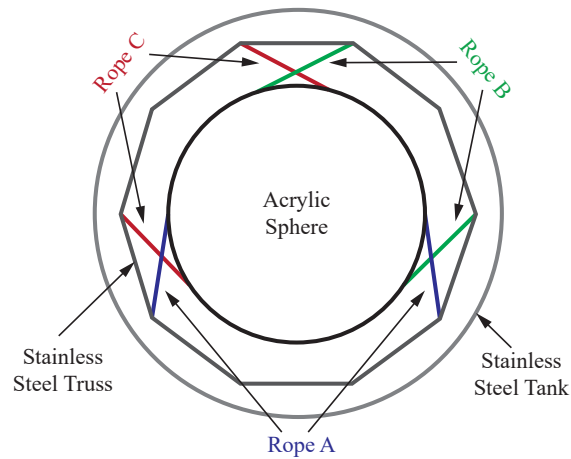


Figure 4.3 Horizontal restriction of the acrylic sphere.

There are 30 holes on the shielding sphere, one hole for each PMT. The shielding sphere is also fixed in the horizontal direction by ropes.

4.1.2 Photomultiplier tube

A total of 30 Hamamatsu R5912 PMTs are utilized in the detector. The photocathode coverage is approximately 12% of 4π . The diameter of the Hamamatsu R5912 is 202 mm. Figure 4.4 shows the dimensional outline of this model of PMT.

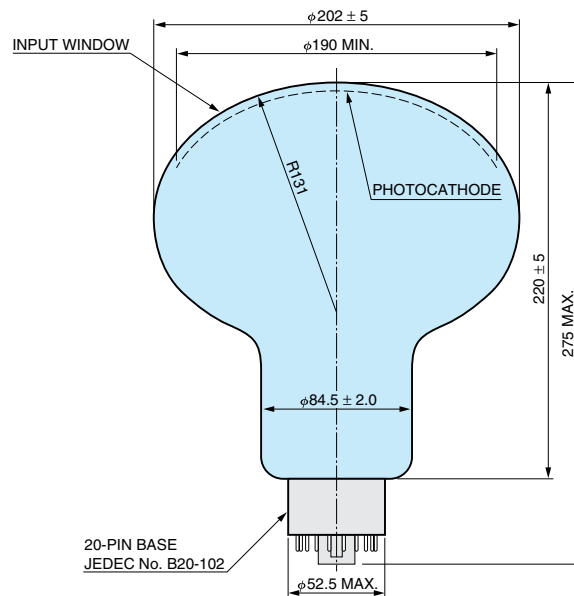


Figure 4.4 Dimensional outline of Hamamatsu R5912^[86]. The unit is mm.

The photocathode material is bialkali. The window is made of borosilicate glass. Figure 4.5 shows the quantum efficiency spectrum, with a spectral response from 300 nm

to 600 nm, and the quantum efficiency at 390 nm is approximately 25%.

The supply high voltages of the 30 PMTs are from 1600 V to 1700 V. In this high voltage range, the transit time (TT) and transit time spread (TTS, FWHM) is approximately 55 ns and 2.4 ns, respectively. The typical value of the waveform rise-time is 3.8 ns.

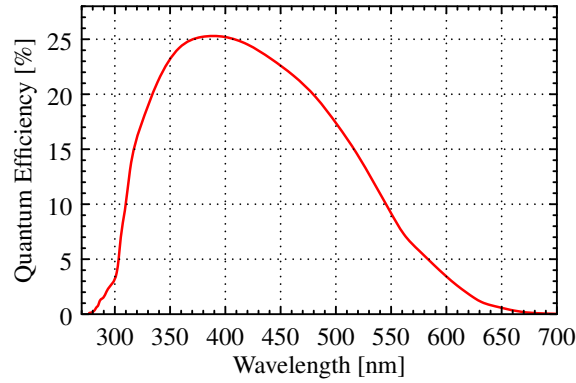


Figure 4.5 Quantum efficiency of R5912 along the wavelength.

The ring (story) and column number define the positions of the 30 PMTs. The PMTs are installed in four stories: 5 in the top and bottom stories, 10 in the middle stories. All the PMTs are fixed on the truss through stainless steel brackets. The uniformity of the PMT distribution is essential for light measurement. Figure 4.6 shows the distribution of PMTs. From *A* to *E* represent the PMTs, and *O* represents the center of the sphere. The angles satisfies $\angle COE = \angle COD = 34.4^\circ$, $\angle AOC = 40^\circ$, $\angle AOB = 39.8^\circ$. Table 4.1 gives the center positions of the total 30 PMTs.

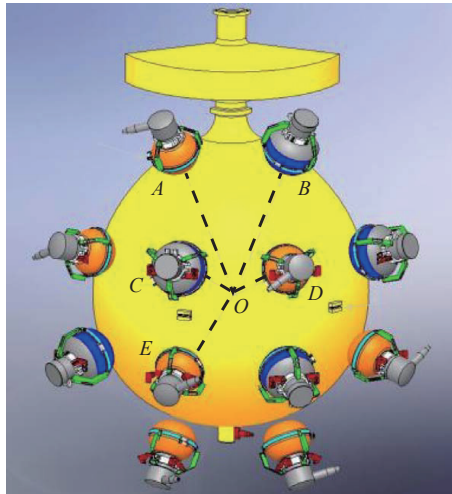


Figure 4.6 Distribution of the PMTs.

Table 4.1 The center positions of total 30 PMTs.

Ring	Column	Channel	x /mm	y /mm	z /mm
1	1	0	428	139	700
1	2	8	0	451	700
1	3	16	-428	139	700
1	4	24	-265	-364	700
1	5	1	265	-364	700
2	1	9	796	0	245
2	2	17	644	467	245
2	3	25	245	756	245
2	4	2	-245	756	245
2	5	10	-644	467	245
2	6	18	-796	0	245
2	7	26	-644	-467	245
2	8	3	-245	-756	245
2	9	11	245	-756	245
2	10	19	644	-467	245
3	1	27	796	0	-245
3	2	4	644	467	-245
3	3	12	245	756	-245
3	4	20	-245	756	-245
3	5	28	-644	467	-245
3	6	5	-796	0	-245
3	7	13	-644	-467	-245
3	8	21	-245	-756	-245
3	9	29	245	-756	-245
3	10	6	644	-467	-245
4	1	14	428	139	-700
4	2	22	0	451	-700
4	3	23	-428	139	-700
4	4	7	-265	-364	-700
4	5	15	265	-364	-700

4.1.3 Pure water circulation system

The water in the stainless steel tank can shield the radioactive backgrounds from the tank and stainless steel truss. The circulation system can purify the water continuously by a pure water machine. The acrylic vessel is also connected to the pure water machine. Figure 4.7 draws the schematic diagram.

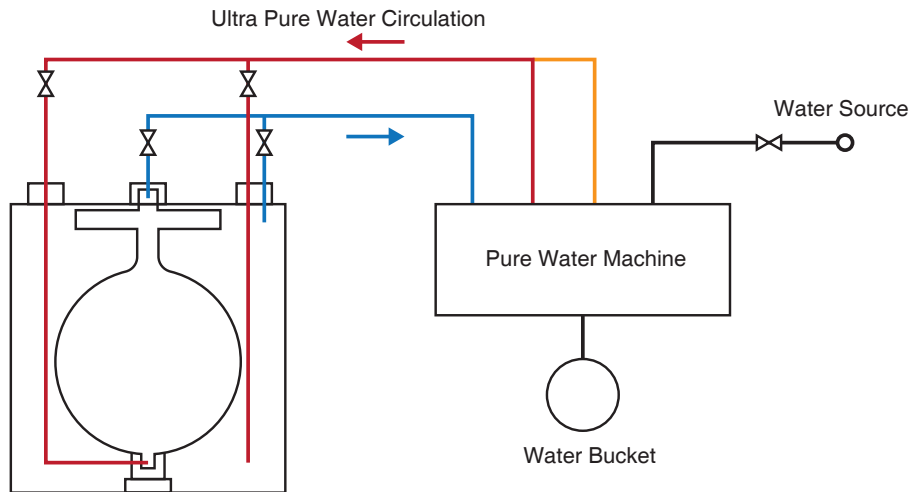


Figure 4.7 Schematic diagram of the Pure water circulation system.

4.1.4 Nitrogen gas system

A nitrogen gas system is deployed in the detector for purging the liquid scintillator. This operation can remove the radon and oxygen in the liquid scintillator. The radon is a serious background, and the oxygen increases the quenching effect. As shown in Figure 4.8, the nitrogen gas comes from the high-pressure cylinder filled with liquid nitrogen. A relief valve is installed on the cylinder to adjust the pressure of nitrogen. A mass flow controller controls the gas flow. The gas goes into the bottom of the liquid scintillator and goes out from a gas washing bottle.

4.1.5 Slow control system

The slow control system consists of the monitors of liquid level sensor, temperature, water resistance, and gas status.

A commercial supersonic sensor Senix TSPC-30S1-232 measures the liquid level. As shown in Figure 4.9, the sensor is a cylinder with a length of 103 mm length, and a diameter of 30 mm. The sensor can also measure the temperature. Two sensors are

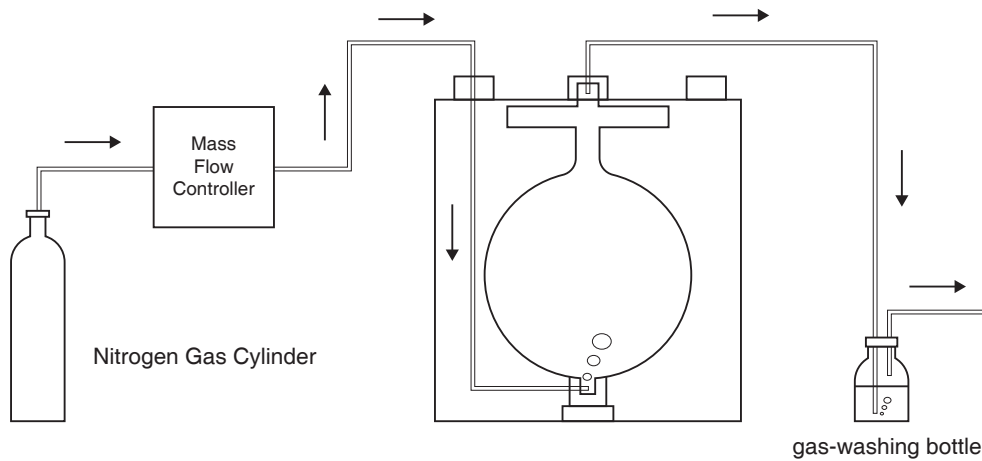


Figure 4.8 Schematic diagram of the nitrogen gas system.

installed on the top of the stainless steel tank and acrylic vessel to measure the water and liquid scintillator level. The sensors are connected with a PC. A client software based on LabVIEW readout the liquid level data, as shown in Figure 4.10. Turning on the sensor may interfere with the electronics system of data taking due to the electromagnetic interference. Therefore, the liquid level is measured once a day only when the data-taking is not running.

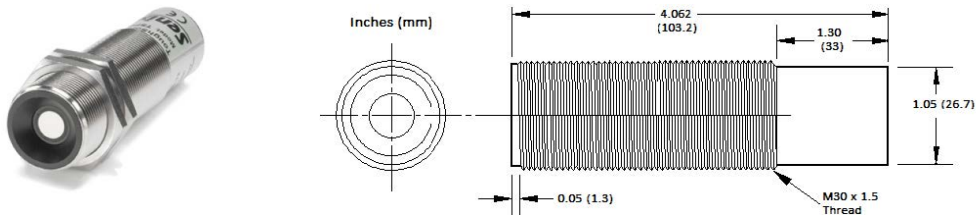


Figure 4.9 The supersonic sensor Senix TSPC-30S1-232^[91] used for liquid level measurement.

Two commercial water resistance sensors model Suntex EC-4100RS are installed at the inlet and outlet of the water circulation system. The water-resistance and temperature are read out by the sensor's LED screen, as shown in Figure 4.11.

The pressure of the nitrogen gas system is read from the barometer of the gas cylinder. Gas pressure in and out of the relief valve is the most concerned. A mass flow controller monitors the gas flow. An oxygen detector installed near the gas cylinder can alert suffocation in case of nitrogen leakage.

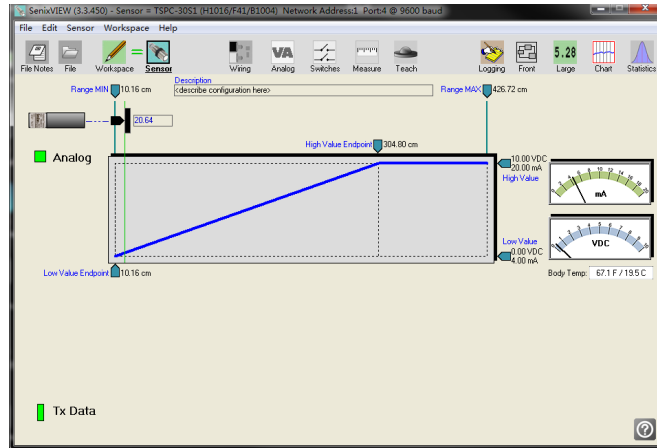


Figure 4.10 The client software for reading the liquid level.



Figure 4.11 Panel of the water resistance sensor.

4.1.6 Installation process

Figure 4.12 and 4.13 shows the detector installation process:

- (a) Fix the acrylic vessel on the acrylic bearing.
- (b) Install the shielding sphere.
- (c) Install the stainless steel truss.
- (d) Install the PMTs onto the stainless steel truss.
- (e) Hoist the whole inner structure into the bottom part of the stainless steel tank.
- (f) Connect the middle and top parts of the tank with the bottom part.

After the installation, we also built a lead brick shielding around the detector to shield radioactive backgrounds from the laboratory.

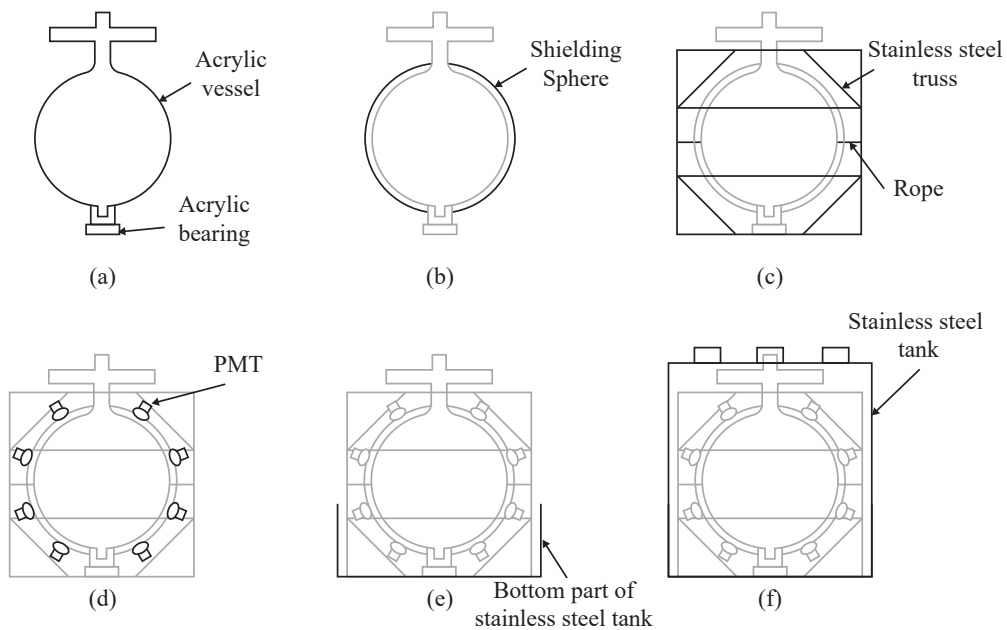


Figure 4.12 Detector installation process.

4.2 Electronics trigger

4.2.1 Electronics boards

The electronics trigger system is installed in a VME crate. There are 6 CAEN VME boards in the VME crate:

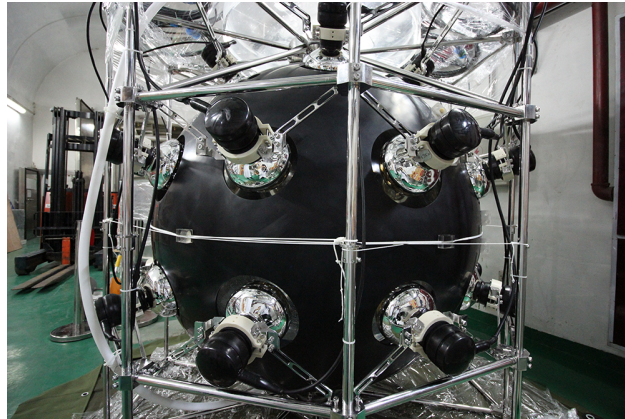
- One VME-PCI optical link bridge V2718^[92], shown in Figure 4.14(a). It is the VME master and the interface to connect the data-taking server.
- Four FlashADC boards V1751^[93], shown in Figure 4.14(b). They convert the PMT waveforms to digital signals.
- One programmable logic unit V1495^[94], shown in Figure 4.14(c). It handles the coincidence logic and generates trigger signals.

V2718 A VME to PCI Optical Link Bridge, 6U height, 1U wide. The unit acts as a VME Master module and can be controlled by a standard PC equipped with PCI or PCIe CAEN Controller cards. The connection between the V2718 and the Controller takes place through an optical fiber cable.

V1751 An 8 Channel 10-bit 1 GS/s Waveform Digitizer, 6U height, 1U wide. The dynamic input is 1 V_{pp}. The voltage offset of the input channels is programmable in the range ± 0.5 V. The digitizer also provides 16 programmable LVDS I/Os.



(a) Acrylic vessel.



(b) Install the acrylic vessel, shielding sphere and PMTs onto the stainless steel truss.



(c) Hoist the whole inner structure into the bottom part of the stainless steel tank.



(d) Connect the middle and top parts of the tank with the bottom part.



(e) Install the lead brick shielding.



(f) Install the platform for the cabinet.

Figure 4.13 Photos of the detector installation process.

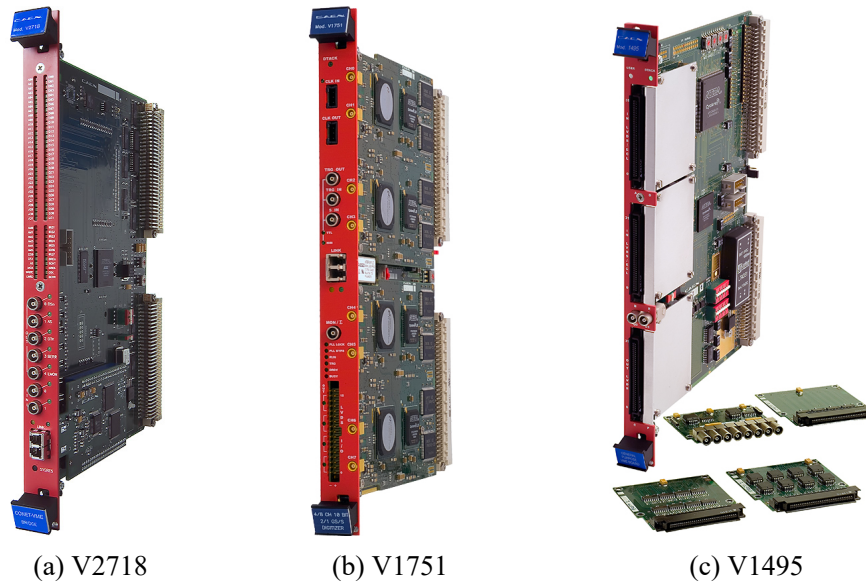


Figure 4.14 Three models of electronics boards.

The modules feature a front panel clock/reference In/Out and a PLL for clock synthesis from internal/external references. The data stream is continuously written in a circular memory buffer. When a trigger occurs, the FPGA writes further N samples for the post-trigger and freezes the buffer that can be read either via VME or via Optical Link. The acquisition can continue without dead time in a new buffer. Mod. V1751 supports multi-board synchronization allowing all ADCs to be synchronized to a common clock source and ensuring trigger time stamps alignment.

V1495 A General Purpose VME Board, 6U height, 1U wide. It is suitable for various digital applications, such as gate, trigger, or translator. The user can directly customize the function by two FPGA: “Bridge” and “User”. The first one, “Bridge”, is used for the VME interface and managing the programming via VME of “User”. The second one, “User” (Cyclone EP1C20), manages the front panel I/O channels and is substantially an empty FPGA. It is available to be programmed by the user according to the desired logic function. The program to determine the coincidence of the PMT signal is accomplished in the FPGA “User”.

4.2.2 Trigger logic

The trigger scheme is shown in Figure 4.15. The analog signals of 30 PMTs are fed into four V1751 boards directly (CH0 ~ CH7 in each board). At the beginning of a run, a software trigger is sent to Board 0 to start all the boards. Then all the boards

start acquiring PMT signals and send the over-threshold signals to the LVDS output. The V1495 processes these LVDS and generates the coincidence signal as the trigger sending back to V1751 Board 0. The trigger signal propagates to other boards in a daisy chain.

Once receiving a trigger signal from V1495, the V1751 digitizer will store the Trigger Time Tag (TTT), increment the event counter, and fill the active buffer with the pre/post-trigger samples. The acquisition window width (also referred to as record length) and the pre/post position is programmable. Before Run 1680, the record length was 1029 ns. This value has been set to 600 ns since Run 1680. An event is composed of the trigger time tag, pre- and post-trigger samples, and the event counter.

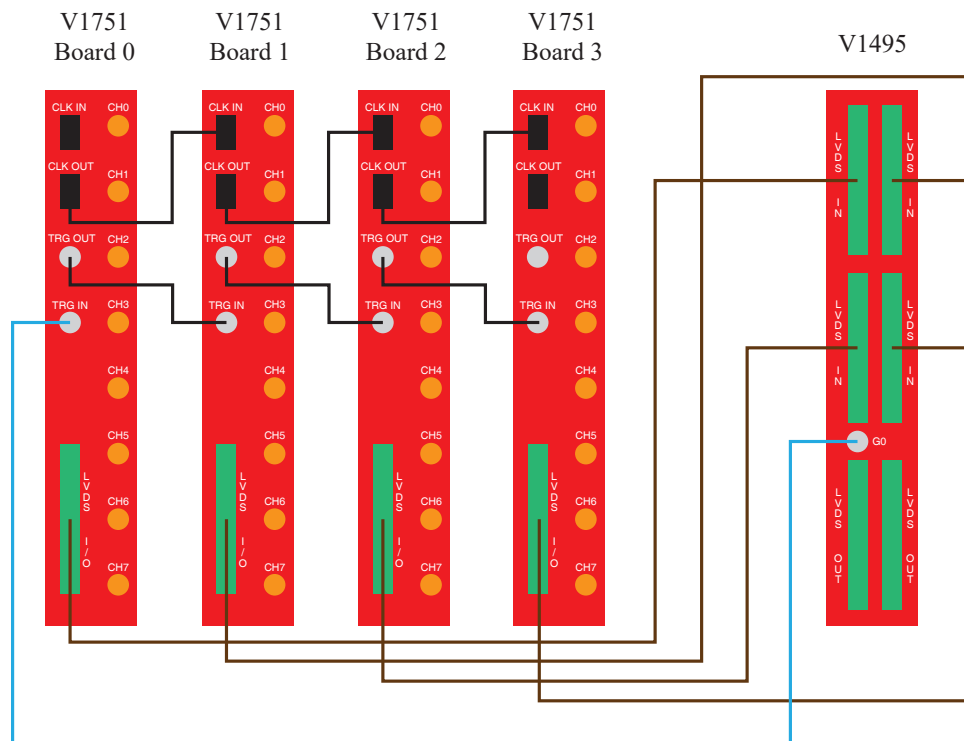


Figure 4.15 Trigger scheme of the 1-ton prototype.

4.2.3 Synchronization

The 1-ton prototype deploys four V1751 boards with the synchronous signal sampling and the same reference, which requires the boards to be “synchronized,” – the internal synchronous board clocks and the identical time reference. The trigger and readout are also be aligned.

4.2.3.1 Clock synchronization

The first action to be performed to obtain the synchronization of the acquisition system is the synchronization of the clock and its phase alignment. The trigger logic algorithms operate at a frequency at 125 MHz, while the ADC sampling frequency is 1 GHz. The sampling clock of the digitizer V1751 is either locked to an internal oscillator or an external clock source. A PLL (Phase-locked Loop) and a Clock Distributor provide the clock management. The PLL can receive a reference clock from either an internal oscillator or an external clock source through the clock input (CLK IN) connector. A mechanic switch on the board allows selecting the clock generator.

The counter, which gives the “event time tag”, the trigger logic, and the ADC sampling work with different frequencies. The event time tag, also called “Trigger Time Tag” (TTT), is given by a counter which marks the arrival time of an external trigger signal or when a signal crosses the relative threshold. For digitizers V1751, TTT is expressed in units of its clock cycles, 8 ns, corresponding to a frequency of 125 MHz. However, when the acquired data is written into the internal board memory, the TTT counter is read every two trigger logic clock cycles, indicating a valid resolution of 16 ns for the trigger timestamp.

In the multi-board acquisition system, the master board (hereafter Master) acts as a clock master to provide a reference clock to the other one – a clock slave (hereafter Slave). A cable connects the CLK OUT of the Master and the CLK IN of Slave. We configure the Master PLL to enable the clock’s output, and the Slave PLL to accept the external clock. The TRG OUT of both boards can be programmed to deliver the clock signal. In so doing, using an oscilloscope can observe the alignment of the clock signals, as shown in Figure 4.16. Then we set a delay on the Master clock output to obtain the alignment of the clock signals produced by TRG OUT of each board.

4.2.3.2 Trigger and readout synchronization

At the beginning of a run, we need a software trigger to start all the boards. Then the external trigger goes to TRG IN of the Master (Board 0). The start of the event acquisition functions in the following way:

- All Slave boards armed to start with TRG IN edge;
- A software (SW) trigger is sent to the Master;
- The SW trigger is propagated through the daisy chain TRG IN/TRG OUT and starts

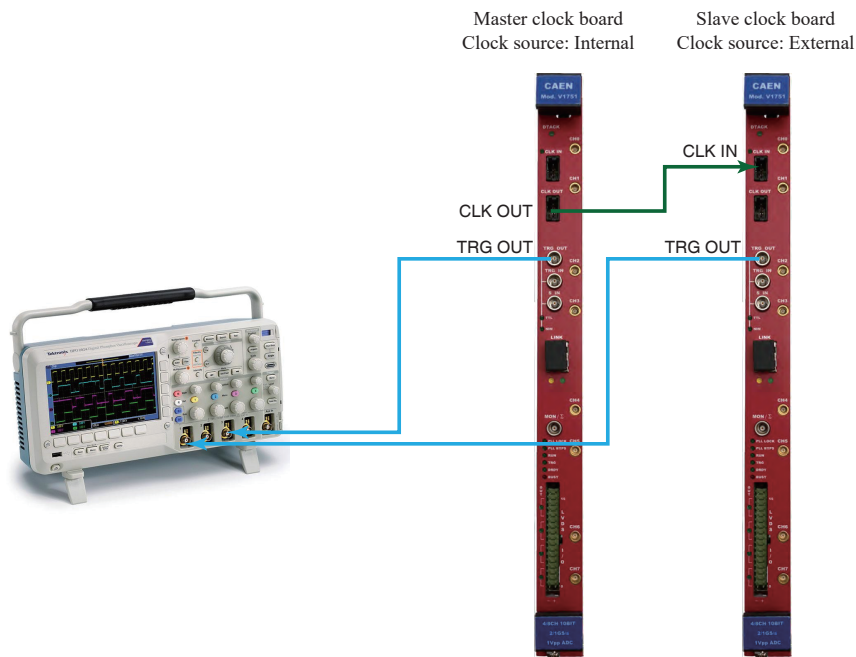


Figure 4.16 Hardware connection of V1751 clock synchronization.

all the boards. In this way a delay is introduced;

- At this point, Master is programmed in to accept trigger on the TRG IN connector. The external trigger signals go through the daisy chain and trigger all the boards.

The external trigger signals goes through the daisy chain and triggered all the boards. The SW trigger that starts the acquisition arrives at the Slave with a delay proper of this hardware configuration. To ensure that all digitizers start the acquisition simultaneously, the Master can set a delay in the start of the event acquisition. Figure 4.17 demonstrates the SW trigger's timing and the acquisition start of a system with four boards.

In the data-taking program, the correct delay is set to obtain the time alignment of the board acquisition start: this will ensure that they will have the same time reference and require temporal correlations between events acquired from different digitizers.

In this hardware setup, the digitizers are configured such that the signals from the external global trigger are considered valid for the event acquisition. The trigger signal sent to the Master is propagated to the Slave in the daisy chain so that the latter can receive the trigger signal with a fixed delay compared to the Master. All boards start the acquisition synchronously, so the trigger propagation introduces a delay also in the TTT of the events acquired by the Slave. Figure 4.18 illustrates the resulting TTT recorded by the boards. The TTT of Master (Board 0) is saved as the trigger timestamp of the event.

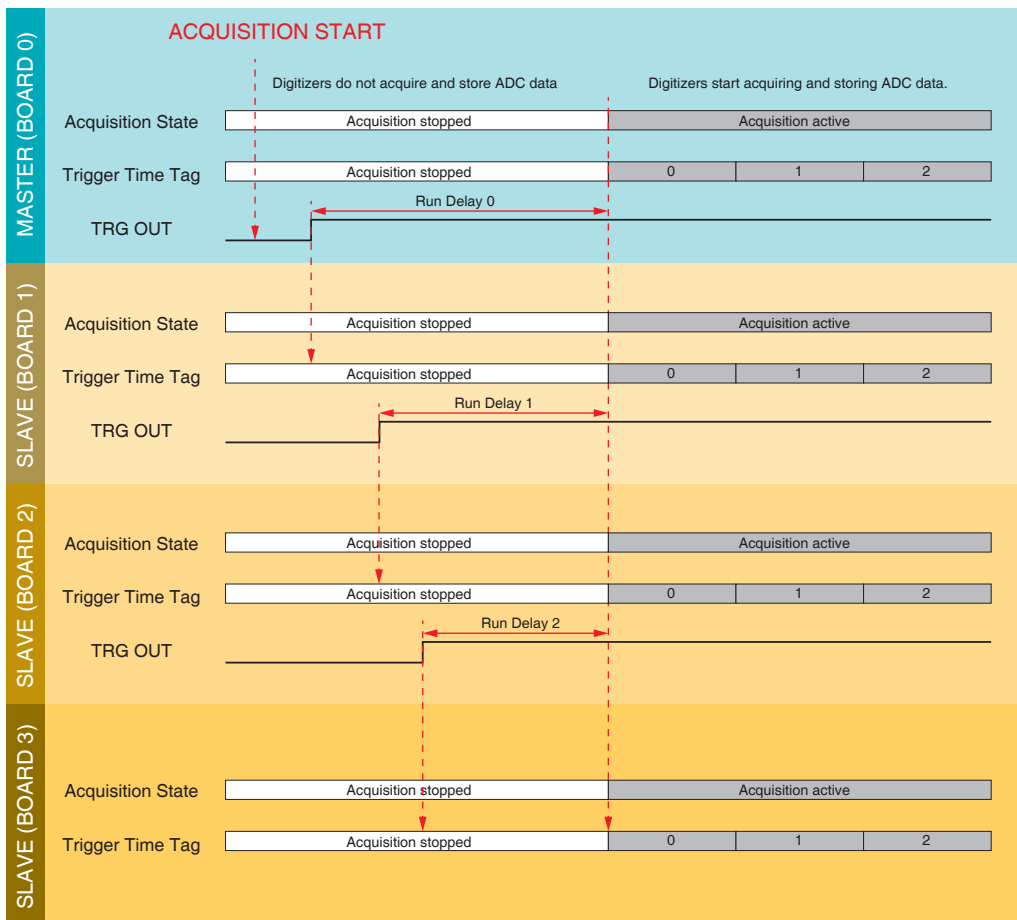


Figure 4.17 Timing diagram of the start of run sequence.

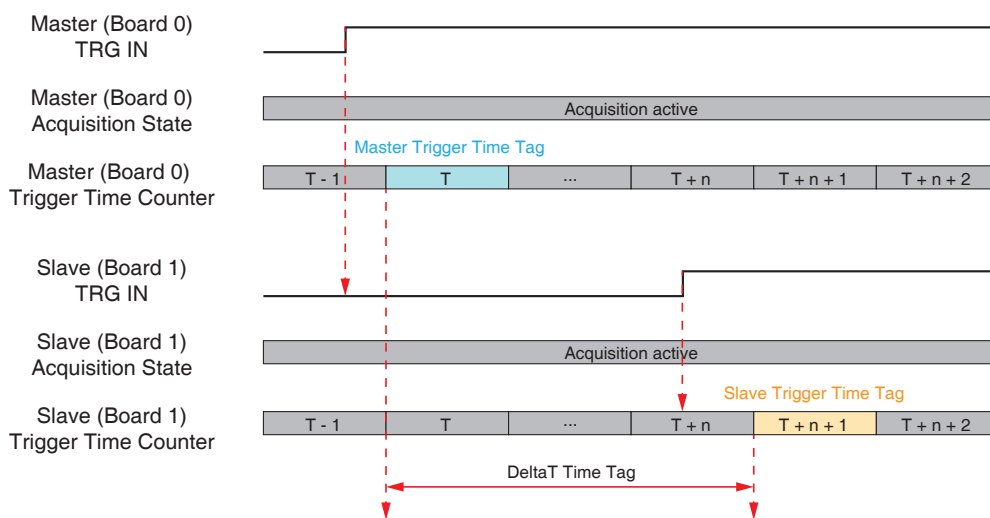


Figure 4.18 Synchronous Master and Slave acquisition (note that the Trigger Time Tags are different).

The memory buffer of the digitizers records the events with timing given by the arrival of the trigger signal. The delay in the TTT of the Slave implies that its memory buffer contains the sampling information that is out of phase compared to the one of the Master. Figure 4.19 explains the delay introduced in the memory buffer of the Slave. Only the waveform in the overlapping part of the sampling time window is saved to the output file.

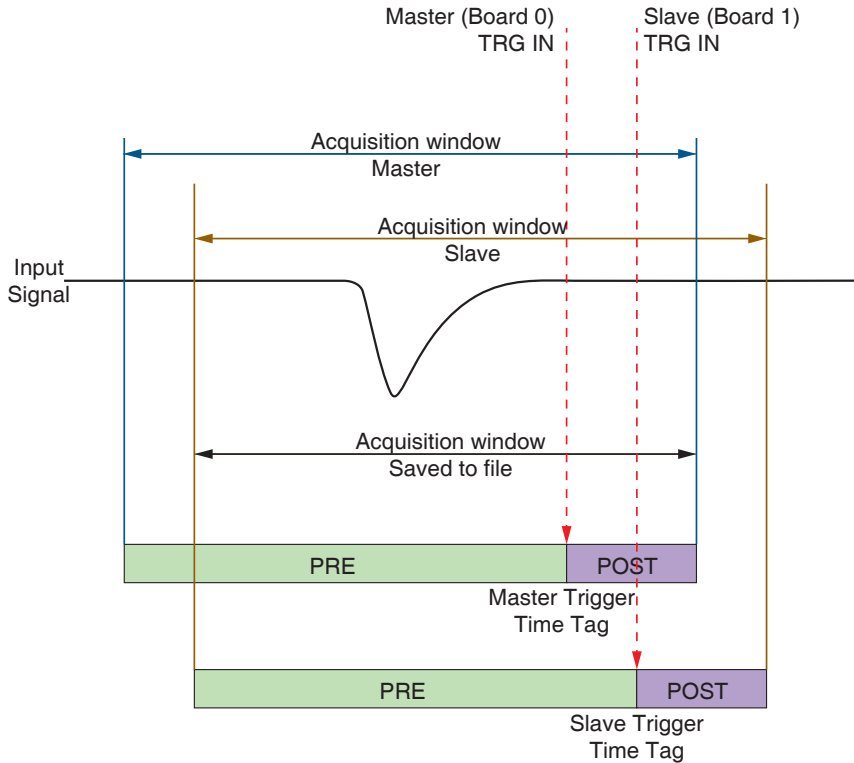


Figure 4.19 Master and Slave acquisition windows.

For V1751, another factor affects the readout alignment in addition to TTT. V1751 packs seven samples together, and we need to know which of the seven samples is over the threshold and triggers the acquisition. Unfortunately, this information is missing in the event structure sent from V1751 due to a bug in CAENDigitizer Library^[95]. We contacted CAEN to report this bug, and they released an update in May 2019. The data taken before Run 1680 had a problem in time alignment between different boards. In an event, the waveform of Board 1, 2, or 3 may have an offset $\Delta T_i, i = 1, 2, 3$ relative to Board 0. This offset is a random variable. The distribution of ΔT_1 distribution of Run 320 to Run 563 is shown in Figure 4.20. We could find two peaks -3 ns and 4 ns in the distribution. In Run 565 to Run 617, the distribution changed, the two peaks are -6 ns and 1 ns, as shown in

Figure 4.21. The synchronization bug was fixed after Run 1680. The ΔT_1 distribution of Run 1718 is shown in Figure 4.20. Only one peak was observed.

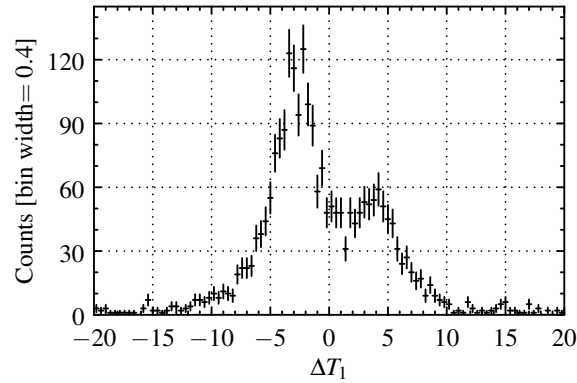


Figure 4.20 ΔT_1 distributions of Run 320 to 563. Tight selection criteria.

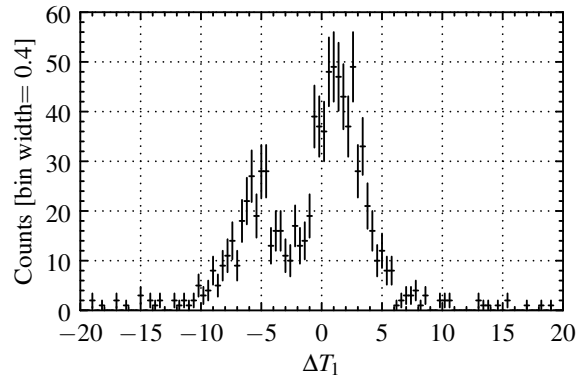


Figure 4.21 ΔT_1 distributions of Run 565 to 617. Tight selection criteria.

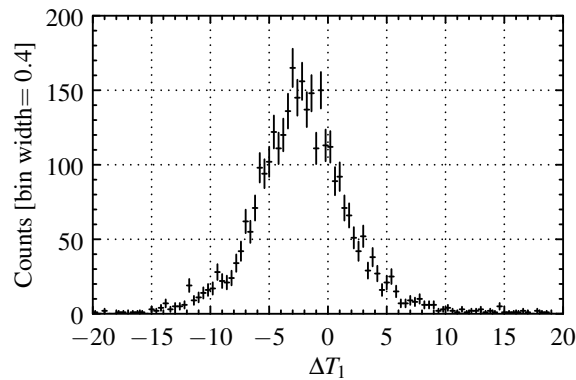


Figure 4.22 ΔT_1 distributions of Run 1718. Tight selection cut criteria.

4.3 Data acquisition system

4.3.1 Hardware system

The data acquisition system reads out data from the digitizers in the VME crate to the data-taking server. As shown in Figure 4.23, V2718 is the VME master, and four V1751 are VME slaves. An optical cable connects A2718 and the PCI express card A3818 in the data-taking server. The data is transferred from V1751 to the bridge V2718 via VME bus and then to the data-taking server through an optical cable.

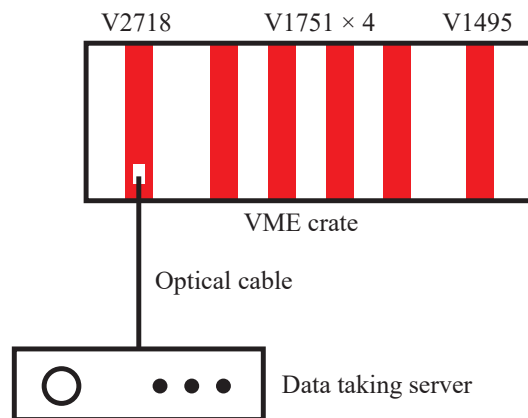


Figure 4.23 The data acquisition system.

4.3.2 Software system

We developed a data-taking program based on CAENVME Library and CAENDigitizer Library to control the hardware system and saves the data to files. The program has three main parts:

1. Initialize and read in parameters from the configuration files.
2. Configure VME boards V1495 and V1751.
3. Data acquisition loop.

There are two configuration files: `pedestal.txt` and `config.txt`. The former one stores the pedestal values of all 30 channels, while the latter one is used to set the run mode and multiplicity (the number of fired PMTs to issue a trigger).

The configuration of V1495 is done through the VME write function provided by CAENVME Library. We initialize the VME bridge V2718 and use `CAENVME_WriteCycle` to write the multiplicity to the corresponding address of V1495. The configuration of V1751 is much more complicated, as follows:

1. The length of each waveform record time window.
2. The channel mask. This operation activates the channels fed into V1751.
3. The interrupt behavior when the memory contains events ready for reading.
4. The trigger position in the time window.
5. DC offset, trigger threshold, and trigger polarity.
6. LVDS output.
7. The behavior when an external trigger arrives
8. Acquisition mode.
9. Malloc readout buffer. The malloc operation must be done after the digitizer's configuration mentioned above.
10. Run delay mentioned in Figure 4.17 for synchronization.

The program can run in two modes: pedestal run and physics run, which have different acquisition loop. In a pedestal run, the program sends a software trigger every $10^5 \mu\text{s}$ in the acquisition loop, and saves the random waveforms (almost baseline) of the 30 PMTs to a file. We start a pedestal run once a day, and this run lasts approximately 1 minute. After the pedestal run, we execute another script to calculate the mean value of all the sample points of a channel. This value is the pedestal. This script also updates the pedestal values in the configuration file.

In a physics run, the program polls the status of V1751 in the acquisition loop. When the data is ready, the program reads the data from the buffer of the digitizer. The data is unpacked into three fields: event number, event time tag, and waveforms. The event time tag is used for correcting the time synchronization, as mentioned in Section 4.2.3.2. Another software selection criterion is applied to the readout waveforms to suppress the false trigger of hardware. The program checks every sample point in the waveform. If no data point is over the threshold (usually is 5 mV), the waveform of this channel will be discarded. The event number, trigger timestamp, and waveforms are saved to files. The maximum size of an output file is set to be 200 MB. When the data size exceeds 200 MB, the program creates a new file. This size is convenient for transfer and data quality checks.

4.3.3 Real-time event display

A real-time event display program is installed in the data-taking server. This program is a front-end web application based on JavaScript. The slow control PC (or other devices in the local area network of CJPL, even a smartphone) can access the data-taking

server by HTTP protocol and browse the web page of real-time event display, as shown in Figure 4.24. We implemented the detector 3D model on the left by `three.js` and implemented the waveforms on the right by Baidu ECharts.

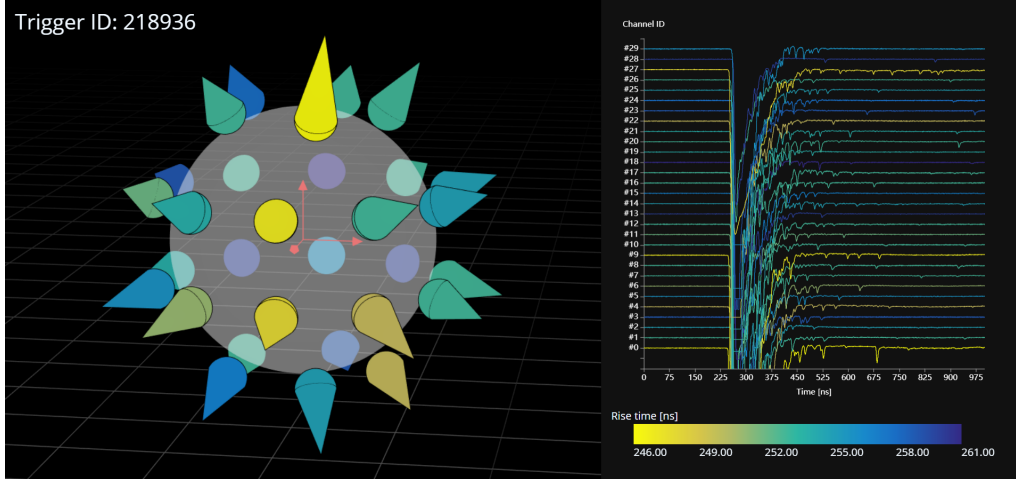


Figure 4.24 Real-time event display of a muon candidate. The color stands for the rise-time and the length of the cone stands for the charge.

The data-taking program writes the trigger ID, trigger time, and waveforms to a JSON file every 2 seconds. The event display program reads the JSON file every 2 seconds, calculates the rise-time and charge of each channel, and then update the web page.

4.3.4 Readout file format

The trigger information and waveforms are saved in ROOT files. One event constitutes an entry of `TTree`, containing the waveforms of all the triggered PMTs. The trigger information includes the run number, trigger number, and trigger timestamp (second and nanosecond). The length of the channel ID array and waveform array are variables. Therefore the channel ID and corresponding waveforms are stored in `std::vector`. Figure 4.25 shows the structure of channel ID and waveform.

For instance, the triggered channel in this event c_0, c_1, \dots, c_{n-1} constitutes the `std::vector<unsigned int> ChannelId`, the $0 \sim k - 1$ element in the `std::vector<unsigned int> Waveform` is the waveform of channel c_0 , the $k \sim 2k - 1$ element is the waveform of channel c_1 , and so on, where k is the length of acquisition window.

We also provide a tool for converting the output ROOT file to HDF5 file. HDF5 is a popular, portable, and flexible file format for storing and managing data. Many languages provide support for HDF5. One can analyze the data without the ROOT framework. We

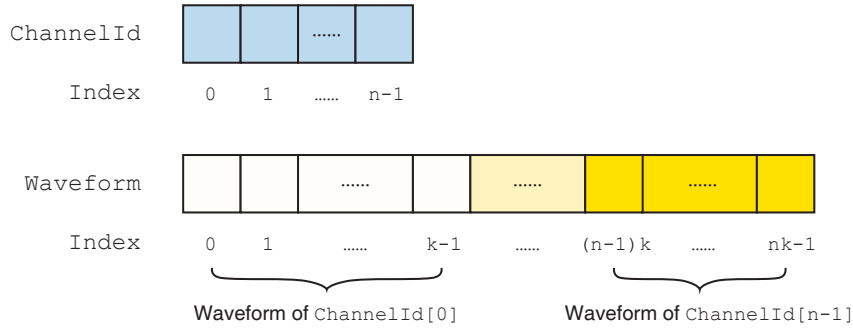


Figure 4.25 The structure of ChannelId and Waveform.

design two tables saved in the HDF5 files. One is the trigger information, and the other is the waveform. The structure and samples of these two tables are shown in Table 4.2 and Table 4.3.

Table 4.2 The structure and samples of TriggerInfo table.

RunID	EventID	TriggerType	DetectorID	Sec	NanoSec
int32	int64	int32	int32	int32	int32
257	1	25	1	1501492559	89692193
257	2	25	1	1501492559	109000153
...

Table 4.3 The structure and samples of Waveform table.

EventID	ChannelID	Waveform
int64	int16	int16 [1029]
257	1	[974, 973, ..., 972]
257	2	[975, 972, ..., 973]
...

4.4 Summary

The 1-ton prototype detector was built for verifying the feasibility of the slow liquid scintillator as the detector material. It has been running for two years since 2017. Using this prototype, we can test the performance of detector components used in the future neutrino experiment (the slow liquid scintillator, PMTs, electronics and DAQ system, etc.), and measure the radioactive background from the detector material and underground

laboratory. The construction process also help us gain experience for large detectors.

Chapter 5 Performance of the 1-ton Prototype Detector

This chapter discusses the performance of the 1-ton prototype, including the run status, calibration, vertex position reconstruction, and Čerenkov light search.

5.1 Run status

The detector started running the water phase on May 5, 2017. Two months later, the liquid scintillator (LS) phase started on July 31, 2017 (Run 257). Several adjustments and updates were applied to the detector for optimization, as shown in Figure 5.1.

5.2 PMT gain calibration

The calibrations of the 1-ton prototype detector include the PMT gain calibration, PMT time calibration, and energy scale calibration. The calibration parameters are also indicators of the detector status.

The PMT gain calibration method is “RollingGain”, a novel method that uses single photoelectron waveform, mainly dark noise hits and low energy events in the data stream, to give a precise and real-time gain measurement. The gain factor characterizes the healthy status of a PMT. It is used for online data quality monitor and offline data processing. The RollingGain calibration doesn’t need to stop a run, or install an LED or laser light source, or to put any extra load on the data acquisition system.

5.2.1 Parametrization of single photoelectron waveform

To model the asymmetric PMT single photoelectron pulse shape, we chose the exponentially modified Gaussian (EMG, or ex-Gaussian) function, i.e., a convolution of a right-sided exponential function and a Gauss function,

$$f(t) = A_0 \cdot \frac{1}{\tau} \exp\left(-\frac{t}{\tau}\right) \theta(t) \otimes \frac{1}{\sigma\sqrt{2\pi}} \exp\left(-\frac{t^2}{2\sigma^2}\right) \quad (5-1)$$

where $\theta(t)$ is the Heaviside step function,

$$\theta(x) = \begin{cases} 0, & x < 0 \\ 1, & x \geq 0 \end{cases} \quad (5-2)$$

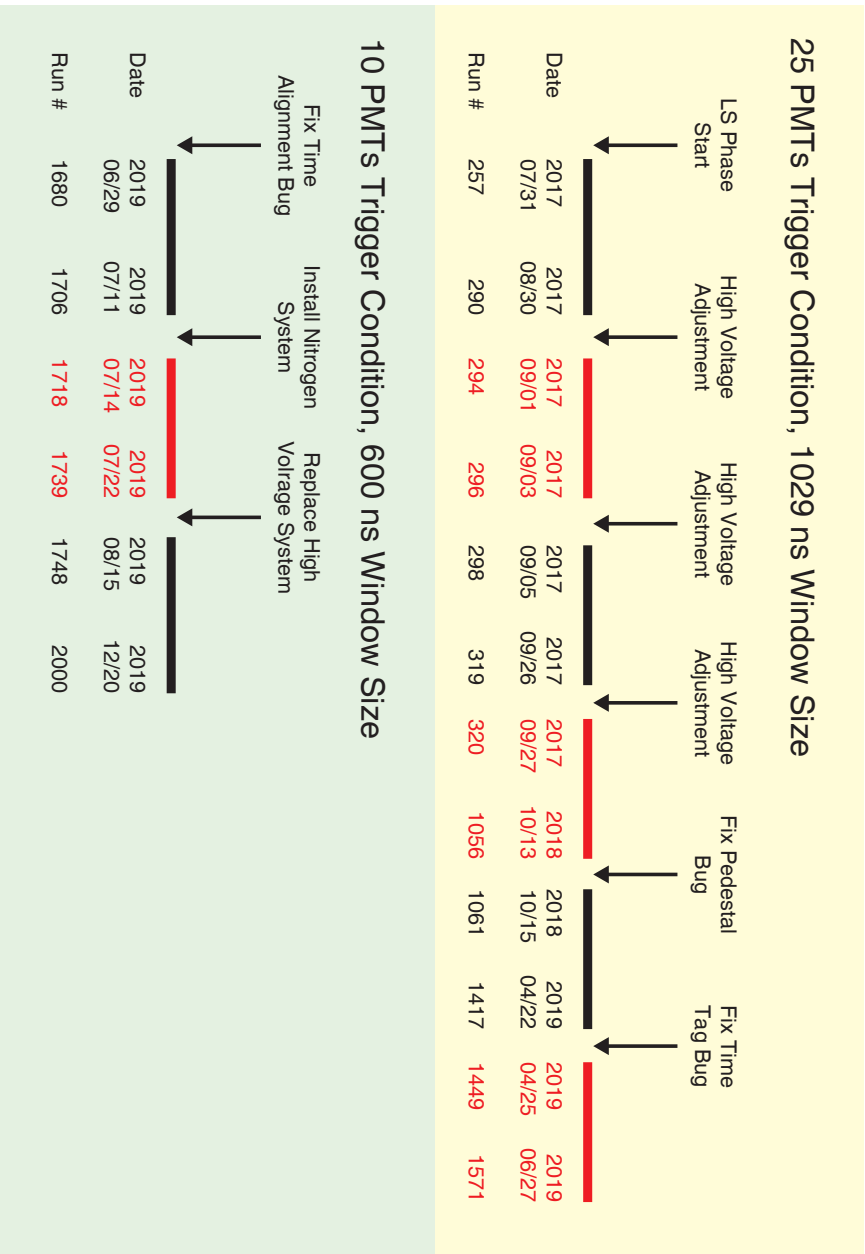


Figure 5.1 Adjustments during the LS phase.

The convolution could be carried out and the pulse shape could be written in an explicit form,

$$f(t) = A_0 \cdot \frac{1}{2\tau} \exp\left(\frac{\sigma^2}{2\tau^2} - \frac{t}{\tau}\right) \operatorname{erfc}\left(\frac{\sigma}{\sqrt{2}\tau} - \frac{t}{\sqrt{2}\sigma}\right) \quad (5-3)$$

The function contains three free parameters: the single PE charge A_0 and two shape parameters σ and τ , which determine the left width and right width of the pulse. Figure 5.2 shows the plot of this function.

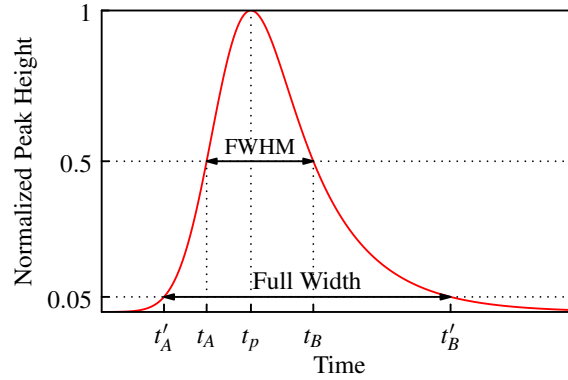


Figure 5.2 An example of the ex-Gaussian function.

To find the FWHM and full width, we calculated the peak time first. Using the condition that the first derivative of Eq. (5-3) is zero, the peak time t_p can be calculated by the formula

$$t_p = \sigma \left(\frac{\sigma}{\tau} - \sqrt{2}x \right) \quad (5-4)$$

where x is the root of the equation

$$e^{x^2} \operatorname{erfc}(x) = \sqrt{\frac{2}{\pi}} \cdot \frac{\tau}{\sigma} \quad (5-5)$$

This indicates that t_p equals σ times a function of τ/σ .

Assuming that $t_A = t_p - \mu_1\sigma$ and $t_B = t_p + \mu_2\sigma$, μ_1 and μ_2 satisfy

$$\exp\left(\mu_1 \cdot \frac{\sigma}{\tau}\right) \operatorname{erfc}\left(x + \frac{\mu_1}{\sqrt{2}}\right) = 0.5 \operatorname{erfc}(x) \quad (5-6)$$

$$\exp\left(-\mu_2 \cdot \frac{\sigma}{\tau}\right) \operatorname{erfc}\left(x - \frac{\mu_2}{\sqrt{2}}\right) = 0.5 \operatorname{erfc}(x) \quad (5-7)$$

These two equations only contain the combinations of τ/σ , which indicates that $\text{FWHM} = t_B - t_A = \sigma(\mu_1 + \mu_2)$, also equals σ times a function of τ/σ , notated by H ,

$$\text{FWHM} = \sigma H\left(\frac{\tau}{\sigma}\right) \quad (5-8)$$

The plot of $H(\tau/\sigma)$, as shown in Figure 5.3, could be obtained from the numerical solution of Eq. (5-6) and (5-7). Note that $H(\tau/\sigma) \rightarrow 2.355$ when $\tau/\sigma \rightarrow 0$ in the Gaussian function approximation. Also, $H(\tau/\sigma) \rightarrow 0.693\tau/\sigma$ when $\tau/\sigma \rightarrow \infty$ in the exponential function approximation.

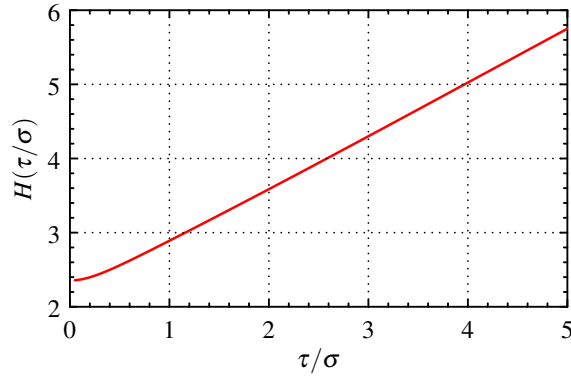


Figure 5.3 Plot of $H(\tau/\sigma)$.

For a PMT pulse, τ/σ is usually in the range of 1 to 5. We find that $H(\tau/\sigma)$ is almost a linear function in this range. The fit function is

$$H\left(\frac{\tau}{\sigma}\right) = 2.144 + 0.720\frac{\tau}{\sigma} \quad (5-9)$$

Therefore FWHM is a linear combination of σ and τ ,

$$\text{FWHM} = 2.144\sigma + 0.720\tau \quad (5-10)$$

Similarly, the full width is

$$\text{Full width} = 3.559\sigma + 3.042\tau \quad (5-11)$$

Figure 5.4 shows a typical single PE waveform (PMT 0, Run 1860, File 0, Trigger 17). The fitting result shows that $\sigma \approx 1.46$ ns and $\tau \approx 2.84$ ns. The FWHM is 5.18 ns and the full width is 13.84 ns.

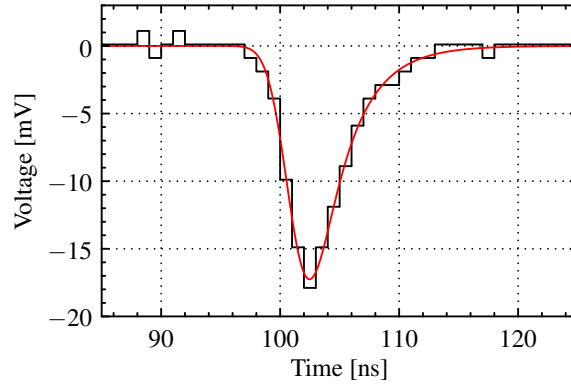


Figure 5.4 A typical single PE waveform and the fit result.

5.2.2 Peak search

We used the Savitzky-Golay filter to determine the number of peaks. The peak search algorithm is a smooth filter of a time series f_i with the time label t_i . Savitzky-Golay filter was first introduced by A. Savitzky and M.J.E. Golay in 1964^[96]. The key idea is that the polynomial fit at t_i gives the smoothed value g_i . We denote a polynomial $p_i(t)$ of degree M which is fitted in the least-square method through $2n + 1$ points (n points on the left and right side of t_i respectively). Then we have $g_i = p_i(t_i)$.

Here the polynomial $p_i(t)$ can be written as

$$p_i(t) = \sum_{k=0}^M b_k (t - t_i)^k \quad (5-12)$$

The smoothed value $g_i = p_i(t_i) = b_0$. The peak search algorithm need the first and second derivation of f_i

$$p_i'(t_i) = b_1, \quad p_i''(t_i) = 2b_2 \quad (5-13)$$

The least-square method is used to determine b_k ,

$$\min_{b_k} \sum_{j=i-n}^{i+n} [p_i(t_j) - f_j]^2 \quad (5-14)$$

or in a matrix form

$$\min_{\mathbf{b}} (\mathbf{A}\mathbf{b} - \mathbf{f})^2 \quad (5-15)$$

where

$$A = \begin{pmatrix} (-n)^M & (-n)^{M-1} & \cdots & 1 \\ (-n+1)^M & (-n+1)^{M-1} & \cdots & 1 \\ \vdots & \vdots & \vdots & \vdots \\ 0 & 0 & \cdots & 1 \\ \vdots & \vdots & \vdots & \vdots \\ (n-1)^M & (n-1)^{M-1} & \cdots & 1 \\ n^M & N^{M-1} & \cdots & 1 \end{pmatrix} \in \mathbb{R}^{(2n+1) \times (M+1)} \quad (5-16)$$

$$\mathbf{b} = \begin{pmatrix} b_M \\ \vdots \\ b_1 \\ b_0 \end{pmatrix} \in \mathbb{R}^{(M+1) \times 1}, \quad \mathbf{f} = \begin{pmatrix} f_{i-n} \\ \vdots \\ f_i \\ \vdots \\ f_{i+n} \end{pmatrix} \in \mathbb{R}^{(2n+1) \times 1} \quad (5-17)$$

The solution of \mathbf{b} is

$$\mathbf{b} = (A^T A)^{-1} A^T \mathbf{f} \quad (5-18)$$

This can be stably solved by means of the QR -decomposition,

$$A = QR \quad (5-19)$$

where Q is a $(2n+1) \times (M+1)$ orthogonal matrix and R is an $(M+1) \times (M+1)$ upper triangular matrix. Thus

$$\mathbf{b} = R^{-1} Q^T \mathbf{f} \equiv B \mathbf{f} \quad (5-20)$$

The matrix B , which depends on the filter parameters n and M , can be calculated before the peak search. The first derivation of f_i is a linear combination of $f_{i-n}, \dots, f_i, \dots, f_{i+n}$. In our peak search algorithm, we choose $n = 4, M = 3$.

5.2.3 PMT charge response model

The PMT charge response model was introduced by Bellamy^[97]. When one photoelectron is collected by the first dynode, the charge distribution is a Gaussian distribution,

$$G_1(x) = \frac{1}{\sigma_1 \sqrt{2\pi}} \exp \left[-\frac{(x - Q_1)^2}{2\sigma_1^2} \right] \quad (5-21)$$

where Q_1 is the gain calibration result to be determined. In the case of n photoelectrons, the charge distribution is the convolution of n single charge distribution. Therefore the mean is nQ_1 and the standard deviation $\sqrt{n}\sigma_1$,

$$G_n(x) = \frac{1}{\sigma_1 \sqrt{2n\pi}} \exp \left[-\frac{(x - nQ_1)^2}{2n\sigma_1^2} \right] \quad (5-22)$$

The response of an ideal noiseless PMT is simply a convolution,

$$S_{\text{ideal}}(x) = f(n) \otimes G_n(x) = \sum_{n=0}^{\infty} f_n G_n(x) \quad (5-23)$$

where $f(n)$ is the discrete pdf of n . In the dark noise case, n follows a Poisson distribution,

$$f(n) = P(n; \mu) = \frac{\mu^n e^{-\mu}}{n!} \quad (5-24)$$

$$S_{\text{ideal}}(x) = P(n; \mu) \otimes G_n(x) = \sum_{n=0}^{\infty} \frac{\mu^n e^{-\mu}}{n!} \frac{1}{\sigma_1 \sqrt{2n\pi}} \exp \left[-\frac{(x - nQ_1)^2}{2n\sigma_1^2} \right] \quad (5-25)$$

The background processes are split into two groups with different distribution functions:

1. The low charge processes present in each event (e.g., the leakage current, etc.) These processes are responsible for the nonzero width of the signal distribution when there is no photoelectron emission from the photocathode (pedestal). A Gaussian distribution can describe this background;
2. The discrete processes which can, with nonzero probability, accompany the measured signal (such as the thermal emission from other dynodes, noise initiated by the measured light, etc.). An exponential function can describe this background.

Therefore the background is

$$B(x) = \frac{1-w}{\sigma_0 \sqrt{2\pi}} \exp \left(-\frac{x^2}{2\sigma_0^2} \right) + w \left[\theta(x) a \exp(-ax) \otimes \frac{1}{\sigma_0 \sqrt{2\pi}} \exp \left(-\frac{x^2}{2\sigma_0^2} \right) \right] \quad (5-26)$$

where σ_0 is the standard deviation of the pedestal, w is the probability that a measured signal is accompanied by a type II background process, a is the coefficient of the exponential decrease of type II background, $\theta(x)$ is the step function,

$$\theta(x) = \begin{cases} 0, & x < 0 \\ 1, & x \geq 0 \end{cases} \quad (5-27)$$

The realistic PMT charge response is a convolution of $S_{\text{ideal}}(x)$ and $B(x)$,

$$S_{\text{real}}(x) = S_{\text{ideal}}(x - Q_0) \otimes B(x) = \sum_{n=0}^{\infty} f_n S_n(x) \quad (5-28)$$

where Q_0 is the mean of the pedestal. The n -th component is represented by $S_n(x)$,

$$S_n(x) = (1 - w)G_n(x - Q_0) + w \frac{\alpha}{2} \exp \left[-\alpha \left(x - Q_n - \frac{1}{2} \alpha \sigma_n^2 \right) \right] \left[1 + \operatorname{erf} \left(\frac{x - Q_n - \sigma_n^2 \alpha}{\sigma_n \sqrt{2}} \right) \right] \quad (5-29)$$

where

$$Q_n = Q_0 + nQ_1 \quad (5-30)$$

$$\sigma_n = \sqrt{\sigma_0^2 + n\sigma_1^2} \quad (5-31)$$

This formula also gives $n = 0$ component correctly,

$$S_0(x) = (1 - w)\delta(x - Q_0) + w \frac{\alpha}{2} \exp \left[-\alpha \left(x - Q_0 - \frac{1}{2} \alpha \sigma_0^2 \right) \right] \left[1 + \operatorname{erf} \left(\frac{x - Q_0 - \sigma_0^2 \alpha}{\sigma_0 \sqrt{2}} \right) \right] \quad (5-32)$$

Note that σ_0 is much smaller than σ_1 . The pedestal can be calculated and subtracted from the raw waveform. The approximation of $Q_0 \rightarrow 0, \sigma_0 \rightarrow 0$ is

$$S_n(x) = (1 - w)G_n(x) + w \frac{\alpha}{2} \exp \left[-\alpha \left(x - nQ_1 - \frac{1}{2} n\alpha \sigma_1^2 \right) \right] \left[1 + \operatorname{erf} \left(\frac{x - nQ_1 - n\alpha \sigma_1^2}{\sigma_1 \sqrt{2n}} \right) \right] \quad (5-33)$$

The $n = 0$ component is given by

$$S_0(x) = (1 - w)\delta(x) + w\alpha\theta(x) \exp(-\alpha x) \quad (5-34)$$

Substitute into Eq. (5-28) we get

$$S_{\text{real}}(x) = f_0 \left[(1 - w)\delta(x) + w\alpha\theta(x) \exp(-\alpha x) \right] + \sum_{n=1}^{\infty} f_n S_n(x) \quad (5-35)$$

In the dark noise case, μ is very small and only $n = 0, 1$ components left,

$$f_0 = e^{-\mu}, \quad f_1 = \mu e^{-\mu} \quad (5-36)$$

The PMT gain calibration is to obtain the charge distribution of a PMT and fit the gain factor Q_1 .

5.2.4 RollingGain on the dark noise

In this section, we describe how to collect the dark noise hits for a PMT, calculate the charge, and fit the charge distribution to obtain the gain factor Q_1 .

5.2.4.1 Event selection

Figures 5.5 and 5.6 show the peak time distribution. The definition of dark noise hits was the waveforms appearing in the window $[0, 150]$ (for 1029 ns window size) or $[0, 40]$ (for 600 ns window size), which did not contain signal. These dark noise hits were single-photon electron events used for the gain calibration. After the main peaks, the tail activity is higher than the noise window because of ringing and after pulses and should be excluded. Cuts used for the dark noise window were applied:

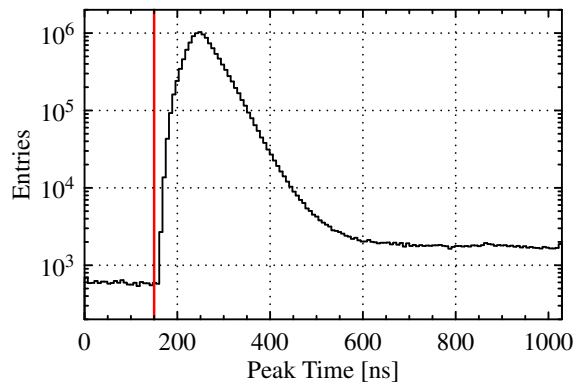


Figure 5.5 The peak time distribution when the data-taking window size is 1029 ns. The dark noise window is $[0, 150]$.

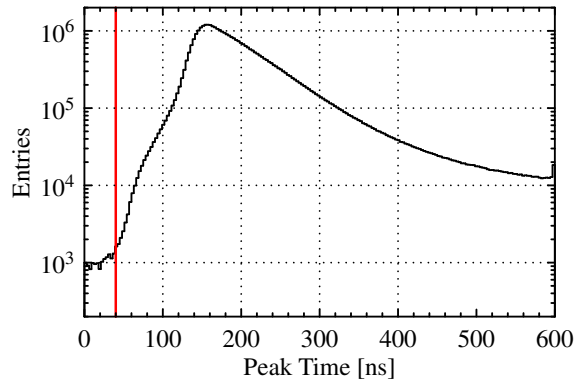


Figure 5.6 The peak time distribution when the data-taking window size is 600 ns. The dark noise window is $[0, 40]$.

Common cuts used for the dark noise window were applied:

- The peak height > 4 mV to avoid the baseline fluctuation.
- The peak time was in $[5, 150]$ (1029 ns window size) or $[5, 30]$ (600 ns window size). The start point was not zero to avoid an incomplete waveform at the beginning.
- The time to the previous trigger was above $20 \mu\text{s}$. This cut was to suppress the effect of re-triggering and ringing. The variance of a single PE charge along the time to the previous trigger is shown in Figure. 5.7.

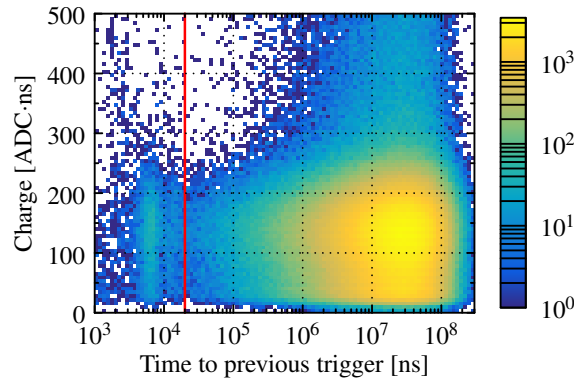


Figure 5.7 The single PE charge v.s. the time to the previous trigger. The plot is made by applying all the rest cuts except for the one being studied. The red line indicates the $20 \mu\text{s}$ cut. The dataset is from Run 1449 to Run 1571.

- Only one PMT had dark noise hit in this event to avoid the physical signal accidentally appearing in the dark noise window.
- Only one PMT has dark noise hit in this event to avoid the accident physical event in the dark noise window.
- The waveform around the peak (peak time -20 ns to $+30$ ns) was summed up to calculate the charge. The waveform was also fitted by the parametrization of single PE waveform Eq. (5-3). To avoid the electronic noise, the fitting should be converged, and the fit result should satisfy $0.8 \text{ ns} < \sigma < 2.5 \text{ ns}$ and $1.5 \text{ ns} < \tau < 6 \text{ ns}$. The σ, τ fit results of PMT #0 are shown in Figure 5.8. Other PMTs have a similar pattern.

5.2.4.2 Fit example

The fit range was from 70 to 400 ADC·ns. The start point was not zero because we had a peak height cut in the dark noise selection, so Eq. (5-35) was not accurate in the low charge range. Meanwhile, the δ function in Eq. (5-35) was eliminated in the fitting range.

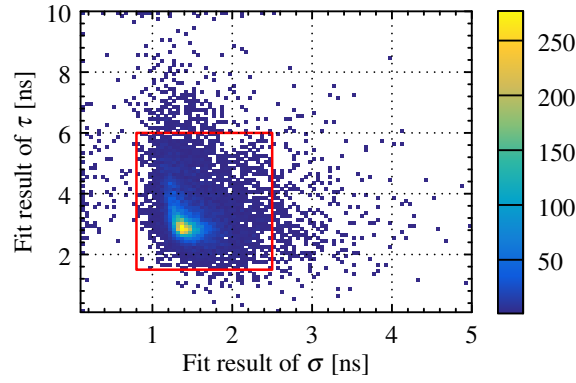


Figure 5.8 The σ , τ fit results of PMT #0. The plot is made by applying all the rest cuts except for the one being studied. The red box indicates the cuts the cut criteria. The dataset is from Run 1449 to Run 1571.

The fit function is written explicitly,

$$S(x) = N e^{-\mu} [w \alpha e^{-\alpha x} + \mu S_1(x)] \quad (5-37)$$

$$S_1(x) = \frac{1-w}{\sigma_1 \sqrt{2\pi}} \exp\left[-\frac{(x-Q_1)^2}{2\sigma_1^2}\right] + w \frac{\alpha}{2} \exp\left[-\alpha\left(x-Q_1-\frac{1}{2}\alpha\sigma_1^2\right)\right] \left[1 + \operatorname{erf}\left(\frac{x-Q_1-\alpha\sigma_1^2}{\sigma_1\sqrt{2}}\right)\right] \quad (5-38)$$

There are 6 free parameters in parametrization: N , Q_1 , σ_1 , w , α , μ .

- N is the overall normalization parameter.
- Q_1 , σ_1 characterize the single PE distribution.
- w , α are parameters for background distribution.
- μ is a related to the intensity of single PE.

All parameters were assumed to be greater than 0, w was assumed to be $0 < w < 1$. Q_1 was the PMT gain factor.

The fitting result of Run1449 to Run1521 is shown in Table. 5.1. χ^2/ndf shows that the model fits the data very well. The fitting examples are shown in Figure 5.9.

5.2.4.3 Fit result check

The RollingGain had a smarter fitter to overcome a lot of practical difficulties. The RollingGain started with the best guess of mean and gauss sigma as the initial values for each channel, then invoked several full-model fits until reaching a good one. The RollingGain also had a strict failure check procedure. It checked

Table 5.1 Fit result of Run1449 to Run1521.

PMT	Q_1	σ_1	$w (\times 10^{-6})$	$\alpha (\times 10^{-2})$	$\mu (\times 10^{-6})$	χ^2/ndf
0	159.4 ± 1.3	40.7 ± 1.0	1.4 ± 0.1	1.7 ± 0.1	1.3 ± 0.0	0.85
1	133.3 ± 1.0	33.8 ± 0.8	2.5 ± 0.1	2.0 ± 0.1	2.3 ± 0.1	1.15
2	147.5 ± 0.3	37.5 ± 0.3	0.8 ± 0.0	1.4 ± 0.0	1.1 ± 0.0	2.14
3	96.1 ± 0.3	39.2 ± 0.2	3.3 ± 0.3	0.6 ± 0.0	50.7 ± 0.3	2.22
4	141.0 ± 1.2	36.6 ± 0.9	1.3 ± 0.1	1.9 ± 0.1	1.0 ± 0.0	1.23
5	163.0 ± 1.4	46.4 ± 1.1	24.6 ± 8.1	1.3 ± 0.1	36.0 ± 11.3	1.02
6	154.7 ± 1.3	41.0 ± 1.2	1.0 ± 0.2	1.5 ± 0.1	1.0 ± 0.2	0.85
7	143.2 ± 0.8	32.9 ± 0.7	2.7 ± 0.5	1.6 ± 0.1	3.0 ± 0.6	0.90
8	155.0 ± 0.4	42.4 ± 0.4	0.8 ± 0.0	1.3 ± 0.0	0.8 ± 0.0	2.20
9	145.6 ± 0.9	36.8 ± 0.8	3.3 ± 0.2	1.6 ± 0.1	3.9 ± 0.1	1.16
10	157.5 ± 2.1	43.2 ± 1.6	9.1 ± 0.8	1.7 ± 0.1	6.0 ± 0.4	1.08
11	156.3 ± 1.5	45.7 ± 1.2	4.5 ± 0.1	1.7 ± 0.1	3.4 ± 0.2	1.12
12	110.3 ± 0.5	31.6 ± 0.4	5.9 ± 0.3	2.0 ± 0.0	7.1 ± 0.2	2.28
13	161.5 ± 0.7	45.1 ± 0.5	1.0 ± 0.0	1.8 ± 0.1	1.4 ± 0.0	1.27
14	160.1 ± 0.6	43.7 ± 0.4	12.6 ± 0.9	1.4 ± 0.0	11.0 ± 0.8	2.14
15	140.5 ± 0.6	39.7 ± 0.5	6.2 ± 0.2	1.4 ± 0.0	6.9 ± 0.1	1.57
16	148.4 ± 1.2	34.2 ± 1.0	2.0 ± 0.4	1.8 ± 0.1	1.1 ± 0.2	0.96
17	138.8 ± 0.5	37.5 ± 0.4	2.4 ± 0.1	1.5 ± 0.0	3.7 ± 0.0	1.53
18	137.8 ± 0.5	37.8 ± 0.4	0.7 ± 0.1	1.1 ± 0.0	0.9 ± 0.1	2.75
19	149.1 ± 0.9	42.6 ± 0.6	12.5 ± 1.2	1.5 ± 0.0	10.9 ± 0.9	1.84
20	167.8 ± 1.3	43.5 ± 1.0	270.5 ± 49.2	1.8 ± 0.1	219.2 ± 37.3	1.04
21	146.3 ± 1.3	40.8 ± 1.0	1.8 ± 0.1	1.8 ± 0.1	1.1 ± 0.0	1.17
22	156.7 ± 1.0	44.3 ± 0.9	2.9 ± 0.5	1.3 ± 0.0	4.4 ± 0.7	1.26
23	142.0 ± 0.7	38.4 ± 0.5	7.6 ± 0.7	1.6 ± 0.0	13.2 ± 0.3	0.91
24	147.7 ± 0.4	39.6 ± 0.3	4.1 ± 0.1	1.3 ± 0.0	4.4 ± 0.0	3.47
25	150.0 ± 1.3	47.0 ± 1.1	36.2 ± 1.7	1.5 ± 0.0	30.4 ± 0.9	0.76
26	166.8 ± 1.2	46.9 ± 1.0	8.2 ± 0.2	1.6 ± 0.0	6.1 ± 0.2	1.19
27	122.1 ± 0.5	27.9 ± 0.4	6.2 ± 0.3	1.5 ± 0.0	8.1 ± 0.2	3.64
28	153.9 ± 0.4	38.6 ± 0.4	5.4 ± 0.1	1.3 ± 0.0	7.4 ± 0.1	1.24
29	153.2 ± 0.4	37.7 ± 0.4	0.6 ± 0.0	1.7 ± 0.0	1.2 ± 0.0	1.40

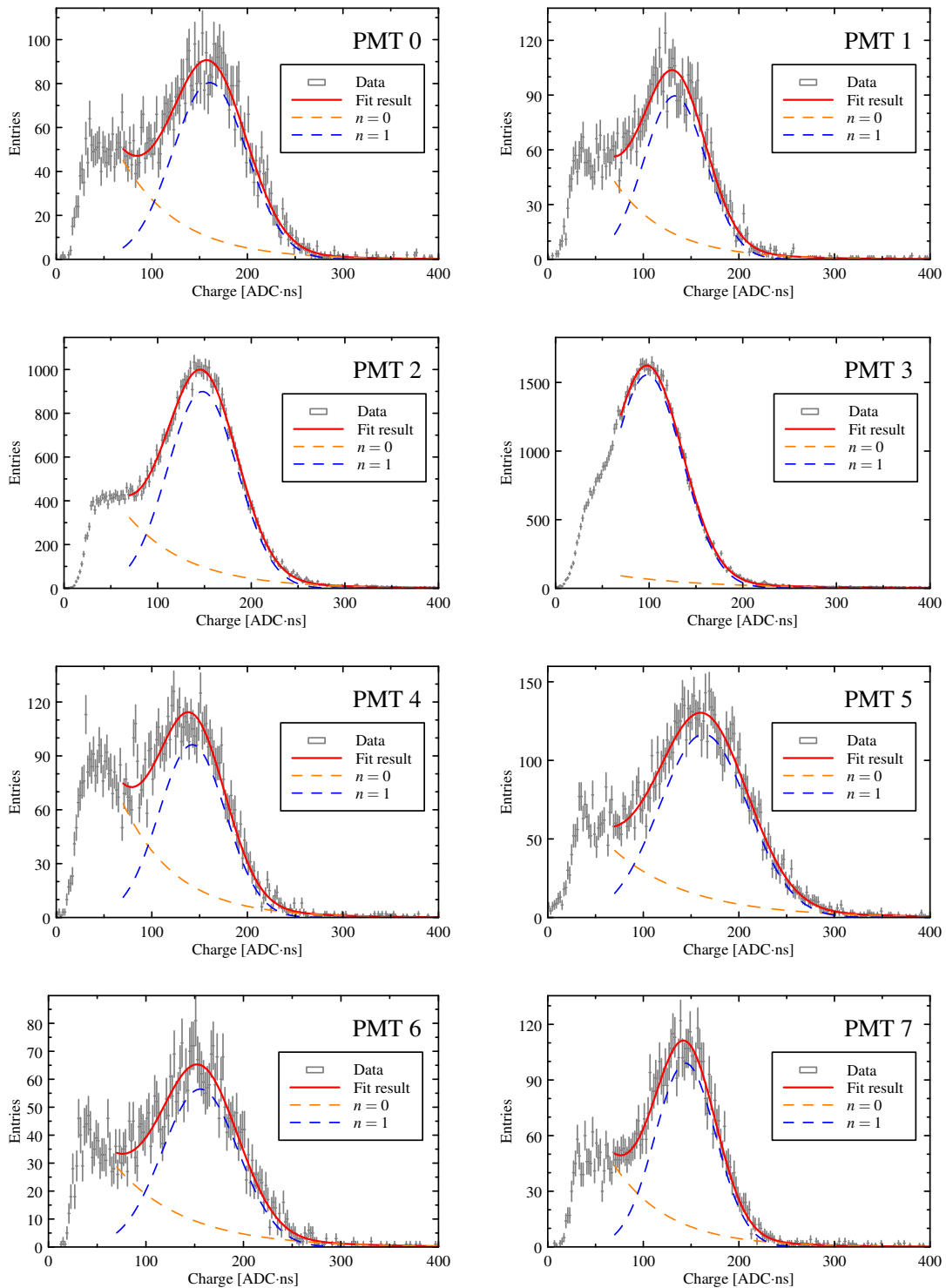


Figure 5.9 Fit to the dark noise of PMT #0 to PMT #7. The $n = 0, 1$ components are also shown. The dataset is from Run 1449 to Run 1521. (to be continued)

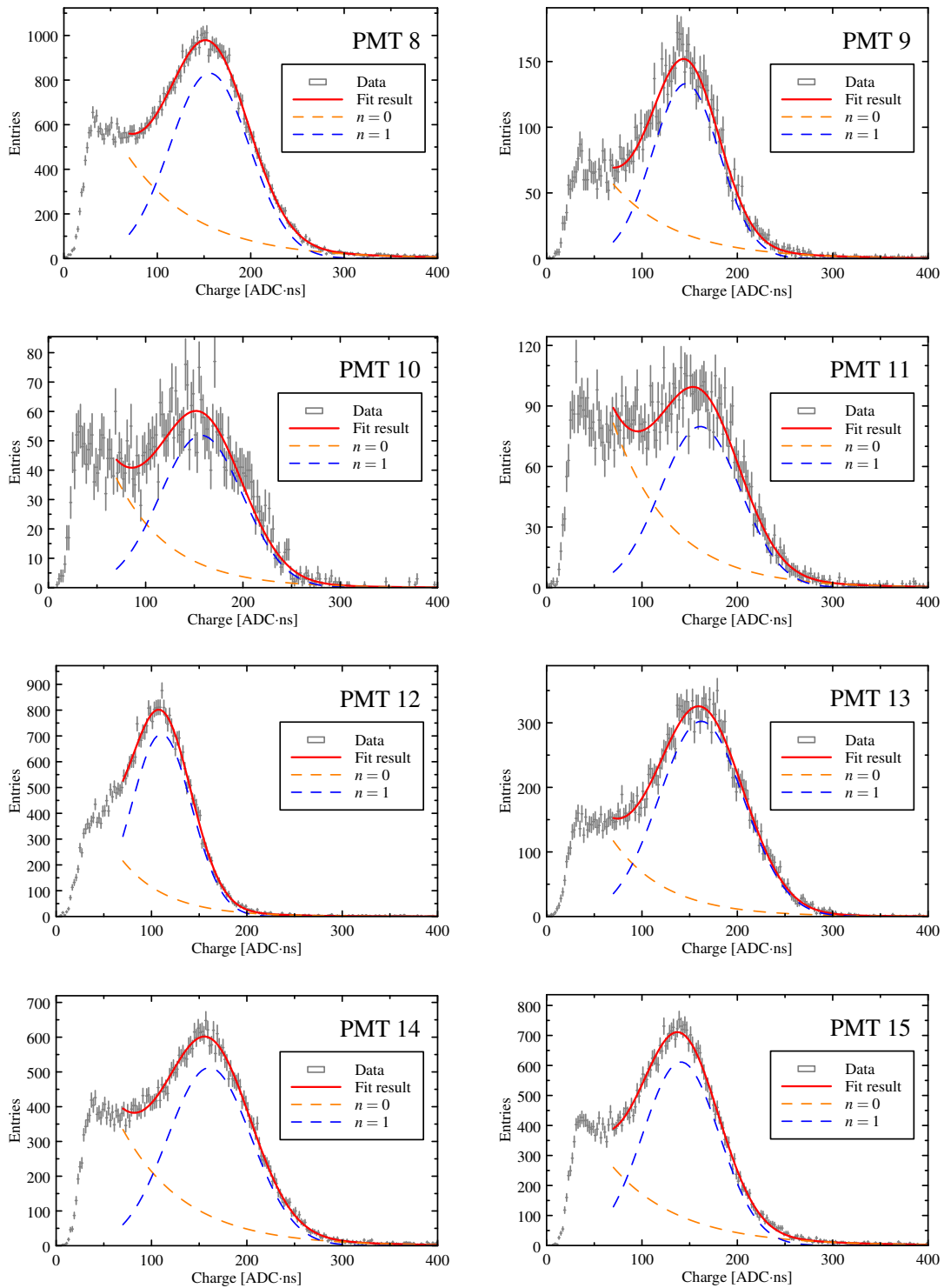


Figure 5.9 Fit to the dark noise of PMT #8 to PMT #15. The $n = 0, 1$ components are also shown. The dataset is from Run 1449 to Run 1521. (to be continued)

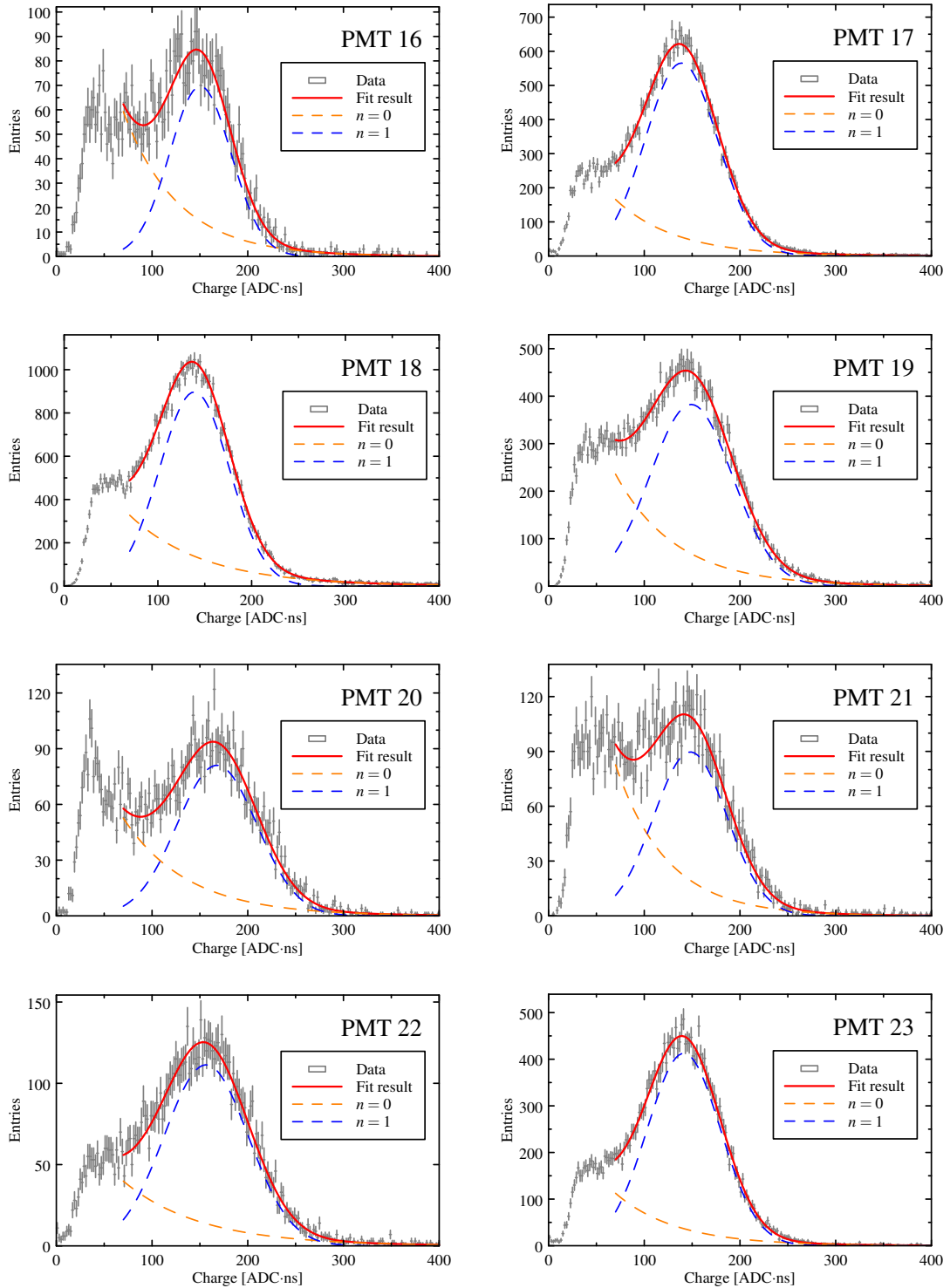


Figure 5.9 Fit to the dark noise of PMT #16 to PMT #23. The $n = 0, 1$ components are also shown. The dataset is from Run 1449 to Run 1521. (to be continued)

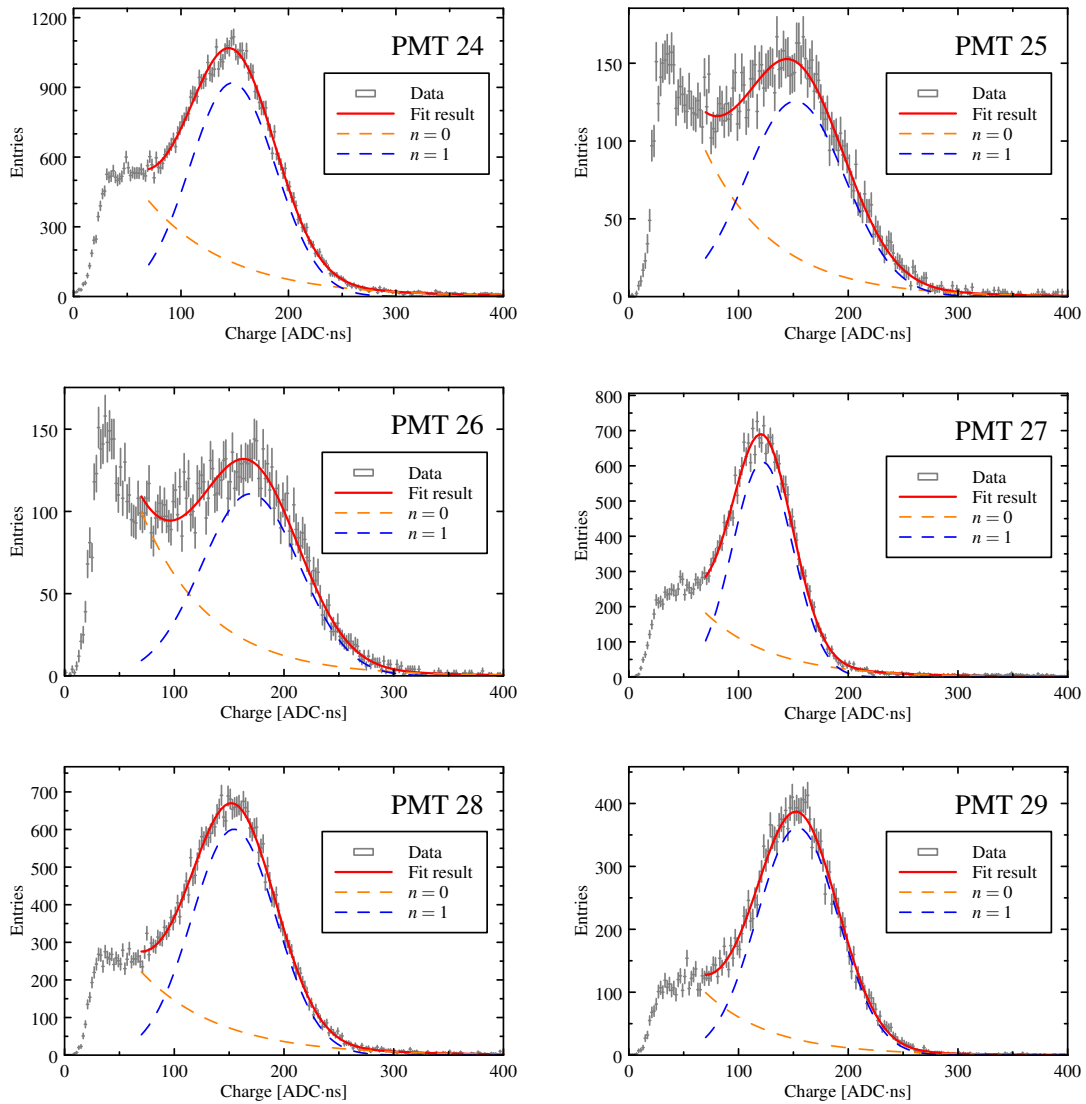


Figure 5.9 Fit to the dark noise of PMT #24 to PMT #29. The $n = 0, 1$ components are also shown. The dataset is from Run 1449 to Run 1521.

- ROOT fit status must be successful.
- $\chi^2/\text{ndf} < 5$.
- The gain Q_1 was within the fitting boundary.
- The σ_1 and Q_1 were legal, i.e., $\sigma_1 < Q_1$. Usually, it should be near 1/3 of the gain.

Figure 5.10 shows the gain fitting result of 30 PMTs on the dataset of Run 1449 to Run 1521. The gain of most PMTs was between 130 to 180 ADC·ns.

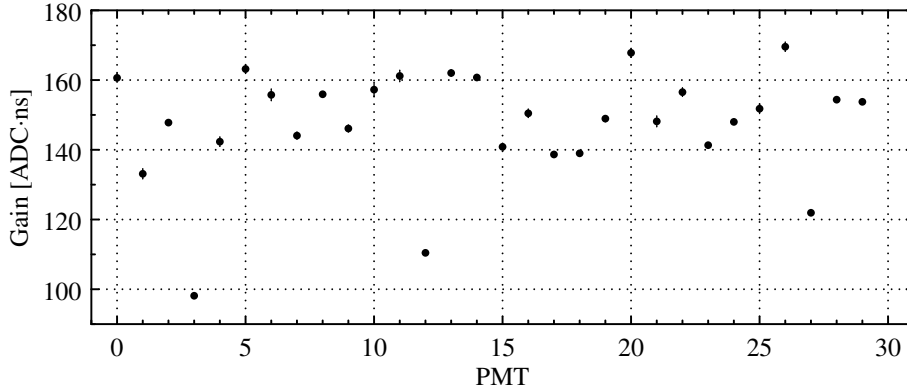


Figure 5.10 The gain fitting results of 30 PMTs for the dataset of Run 1449 to Run 1521. The fitting errors are also shown in the plot. The fitting errors are too small to visible on some data points.

5.2.5 RollingGain on the low energy events

Since the dark noise rate was low, we needed to run the gain calibration routine from every two weeks to one month for a 1% precision fitting result. If we wanted a more real-time calibration and monitored the PMT status, the single peak signal besides dark noise signals should be employed. This procedure is similar to a calibration using an LED light source. The event selection criteria were

- The peak height > 4 mV to avoid baseline fluctuation.
- Only one peak in [200, 400] (1029 ns window size) or [100, 300] (600 ns window size).
- The time to the previous trigger was above 20 μs .
- The waveform around the peak (peak time -20 ns to $+30$ ns) was summed up to calculate the charge. The waveform was also fitted by the parametrization of single PE waveform Eq. (5-3). The fit should be converged, and the fit result should satisfy $0.8 \text{ ns} < \sigma < 2.5 \text{ ns}$ and $1.5 \text{ ns} < \tau < 6 \text{ ns}$.

The fitting function of charge distribution is Eq. (5-35). Only $n = 0, 1, 2$ components

left due to the single peak cut. In an explicit form,

$$S(x) = N [w\alpha e^{-\alpha x} + \mu_1 S_1(x) + \mu_2 S_2(x)] \quad (5-39)$$

$$S_1(x) = \frac{1-w}{\sigma_1 \sqrt{2\pi}} \exp\left[-\frac{(x-Q_1)^2}{2\sigma_1^2}\right] + w \frac{\alpha}{2} \exp\left[-\alpha\left(x-Q_1-\frac{1}{2}\alpha\sigma_1^2\right)\right] \left[1 + \operatorname{erf}\left(\frac{x-Q_1-\alpha\sigma_1^2}{\sigma_1\sqrt{2}}\right)\right] \quad (5-40)$$

$$S_2(x) = \frac{1-w}{2\sigma_1\sqrt{\pi}} \exp\left[-\frac{(x-2Q_1)^2}{4\sigma_1^2}\right] + w \frac{\alpha}{2} \exp\left[-\alpha(x-2Q_1-\alpha\sigma_1^2)\right] \left[1 + \operatorname{erf}\left(\frac{x-2Q_1-2\alpha\sigma_1^2}{2\sigma_1}\right)\right] \quad (5-41)$$

Note that a simple Poisson could not describe the coefficient of $S_i(x)$ because it is only valid for monoenergetic events, but not for signal with different energies. There are 7 free parameters in parametrization: $N, Q_1, \sigma_1, w, \alpha, \mu_1, \mu_2$. Figure 5.11 demonstrates one of the fitting examples. χ^2/ndf shows that the model agrees with the data very well.

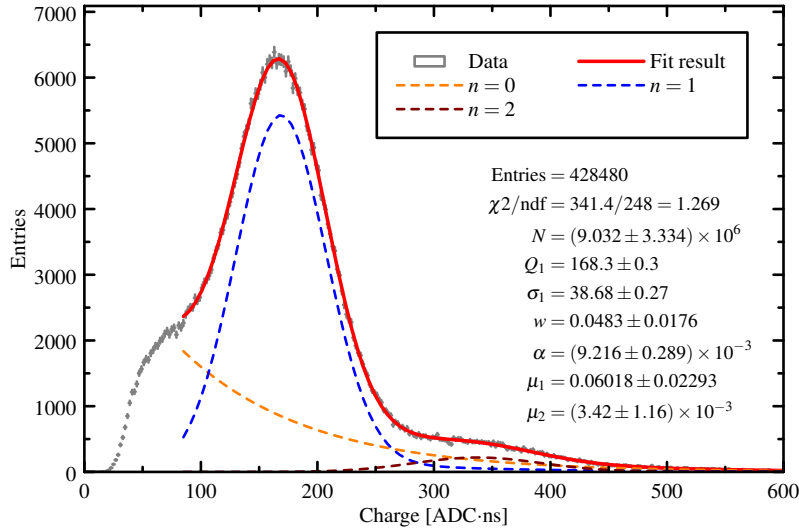


Figure 5.11 The gain fitting result of PMT #0 in the dataset of Run 1449. The $n = 0, 1, 2$ components are also shown.

The calibration result of the low energy event method was close to that of the dark noise method, as shown in Figure 5.12. We found that the result of the low energy event method was higher 1%~5% than that of the dark noise method systematically, but they had the same trend over time, as shown in Figure 5.13.

Refs^{[98][99]} pointed out that the calibration result of the LED method is higher than that of the dark noise method. The reason is controversial. Some researchers claim that a portion of dark noise PEs emission is from the non-first dynode, so the gain is less the LED method^[100]. Others' opinion is that the portion of non-first dynode emission is not large enough to affect the gain fit. Another explanation is the data-taking has a threshold in the LED or low energy events, so the charge is higher systematically.

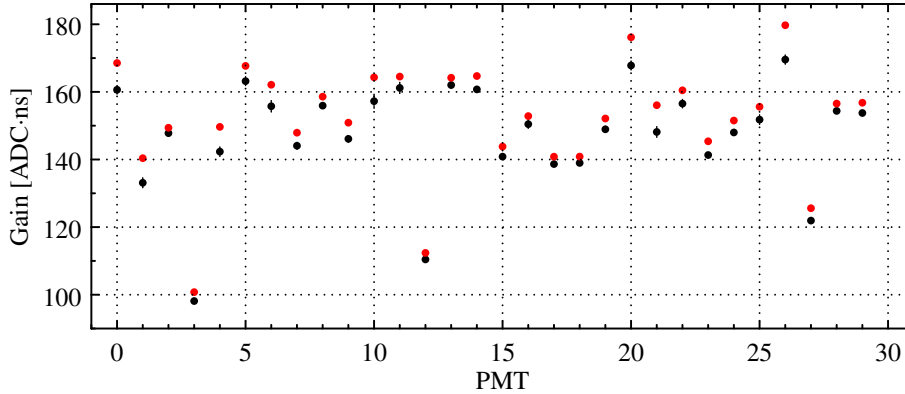


Figure 5.12 The calibration results of the low energy event method (red points) compared to the dark noise method (black points). The dataset is from Run 1449 to Run 1521. The fitting errors are also shown in the plot. Some of them are too small to visible on some data points.

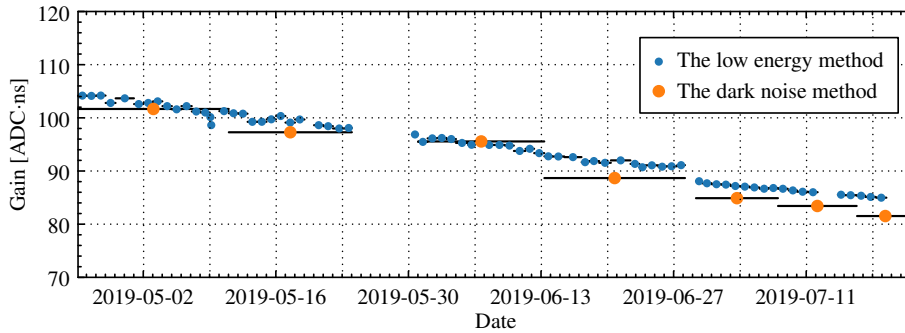


Figure 5.13 The calibration results of PMT #3 v.s. the date. The low energy event method and the dark noise method have the same trend.

The calibration based on low energy events could run every day. We observed the fluctuation of gain in a small period \sim one day. Figure 5.14 shows an example of the gain variance along with the date. Most PMTs are stable except PMT #3, #12, and #23.

5.3 Time calibration

Usually, the time calibration needs the assistance of an LED or laser light source. We used high energy physical events instead of an additional light source. Due to the

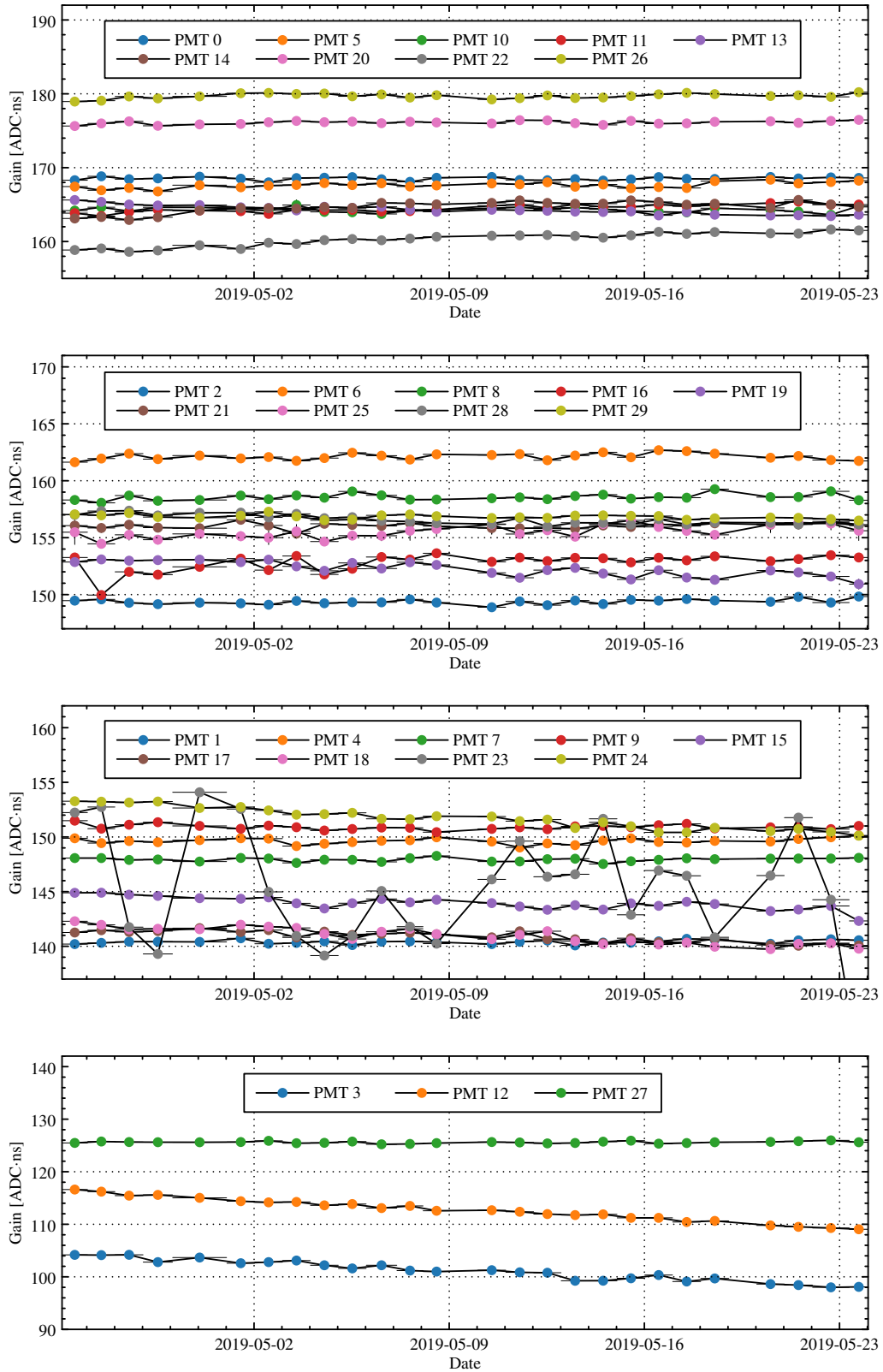


Figure 5.14 Gain v.s. date. The dataset is from Run 1449 to Run 1504.

extensive time constant of the slow liquid scintillator, the calibration is more complicated than the case of a conventional liquid scintillator.

5.3.0.1 PE arrival time

In a conventional TDC circuit, once a PMT pulse crosses the threshold, a timestamp is given and recorded as an edge by TDC. The time of the edge defines the arrival time of the pulse. However, as shown in Figure 5.15, the rising edge of a larger pulse can cross the thresholds earlier, yielding an earlier arrival time, which called the time slewing effect. In the 1-ton prototype detector, the FlashADC recorded the complete waveform. The arrival time was from the waveform offline study. The threshold was dynamic for the time slewing correction. The first peak was searched in the signal region. The time when the pulse just crossed the 10% of peak height defined the arrival time.

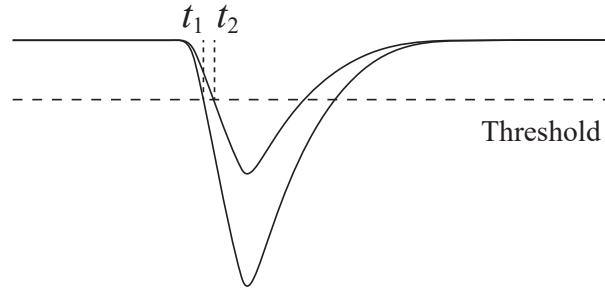


Figure 5.15 Schematic representation of the time slewing effect.

5.3.1 First PE time distribution

The first PE time of each channel was used for PMT time calibration. We studied the distribution of first PE time. The time profile of scintillation is approximate to an exponential distribution if we ignore the rise time constant,

$$S(t) = \frac{1}{\tau} e^{-t/\tau} \theta(t) \quad (5-42)$$

If the vertex is in the center of the detector, the light propagation time is the same for each PMT. The PE time distribution of each PMT is the scintillation time profile convoluted time resolution (a Gaussian function, standard deviation is σ), which can be approximated as

$$f(t) = \frac{1}{2\tau} \exp\left(\frac{\sigma^2}{2\tau^2} - \frac{t}{\tau}\right) \operatorname{erfc}\left(\frac{\sigma}{\sqrt{2}\tau} - \frac{t}{\sqrt{2}\sigma}\right) \quad (5-43)$$

When there are N PEs hitting on this PMT, the probability that the first PE time is t equals the probability that one PE is at t times the probability that $N - 1$ PE is after t . Therefore the distribution of the first PE time $g(t)$ is

$$g(t) = N f(t) \left(\int_t^{\infty} f(x) dx \right)^{N-1} \quad (5-44)$$

Carry out this integral and get

$$g(t) = N f(t) \left[\tau f(t) + \frac{1}{2} \operatorname{erfc} \left(\frac{t}{\sqrt{2}\sigma} \right) \right]^{N-1} \quad (5-45)$$

Sum over all the N components and consider the time offset δ_i (to be calibrated) of each PMT, we can obtain the first PE time distribution of PMT i ($i = 0, 1, \dots, M - 1$),

$$h_i(t) = \sum_{N=1}^{\infty} p_i(N) g(t - \delta_i) \quad (5-46)$$

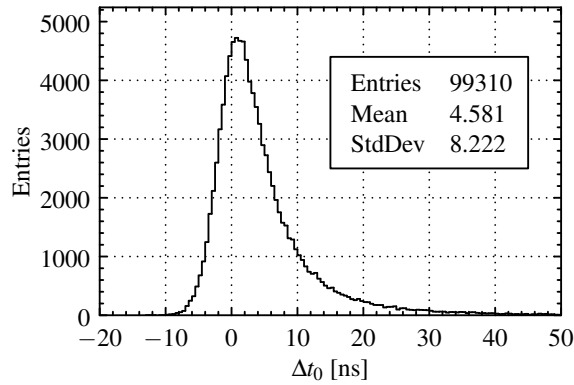
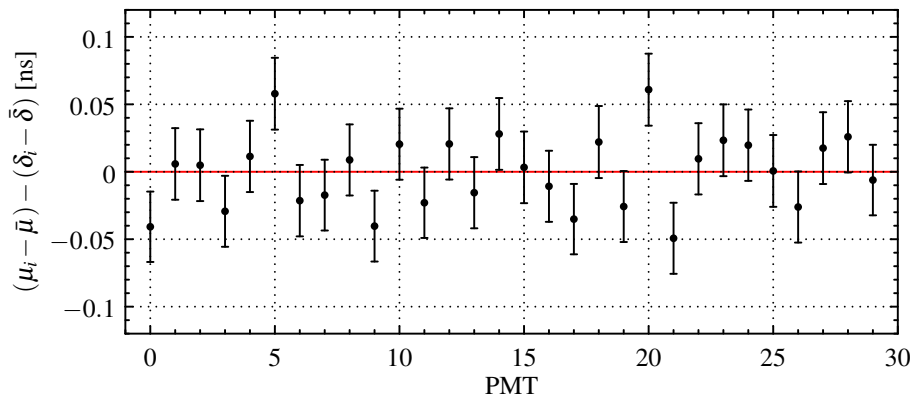
where $p_i(N)$ is the probability that there are N PEs hitting on PMT i . We only care about the relative value of t_i , because different events may be at different positions in the time window,

$$\Delta t_i = t_i - \bar{t} = t_i - \frac{1}{M} \sum_j t_j \quad (5-47)$$

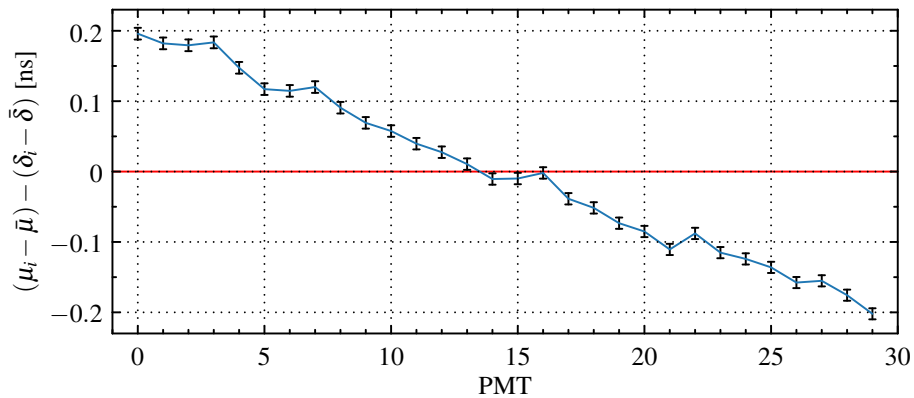
For the convenience of comparison, we used the zero-centered value $\delta_i - \bar{\delta}$, where $\bar{\delta}$ is the average of and δ_i . The time calibration result is invariant under the shift transformation. Eq. (5-46) is hard to fit because $p_i(N)$ is complicated. It is fortunate that t_i only affects the time offset of $h_i(t)$ and not change the function shape. Therefore, we tried to use the method of moments, i.e., calculate the mean value of Δt_i , which is notated as μ_i , instead of fitting Eq. (5-46) for δ_i . The zero-centered values of $\mu_i - \bar{\mu}$ are good enough to approximate $\delta_i - \bar{\delta}$ and could be verified by a toy simulation, as shown below.

We simulated PE time on 30 PMTs. The distribution was Eq (5-43), $\sigma = 2$ ns, $\tau = 25$ ns. The PE number on each PMT was a Poisson variable with a mean value of 5. The time offset of each PMT is sampled from a uniform distribution $[-5$ ns, 5 ns]. Figure 5.16 shows an example of Δt_i distribution.

Figure 5.17 shows the difference between $\mu_i - \bar{\mu}$ and $\delta_i - \bar{\delta}$, indicating that $\mu_i - \bar{\mu}$ is a good estimator for time calibration.


 Figure 5.16 The Δt distribution of PMT #0.

 Figure 5.17 The difference between $\mu_i - \bar{\mu}$ and $\delta_i - \bar{\delta}$ varies with the PMT ID

We also found that if the PE number distribution varies with the PMTs, the estimator $\mu_i - \bar{\mu}$ will have a bias. This problem occurred in the data because PMTs had different quantum efficiency. Some PMTs' PE numbers were slightly less than the others. We changed the Poisson mean value of each PMT in the previous toy simulation. Now the value is $(5 + 0.01i)$ for PMT i . The difference between $\mu_i - \bar{\mu}$ and $\delta_i - \bar{\delta}$ is shown as the blue line in Figure 5.18.


 Figure 5.18 The difference between $\mu_i - \bar{\mu}$ and $\delta_i - \bar{\delta}$ varies with the PMT ID, when PMTs had different PE number.

The calibrated first PE time for the PMT with less PEs was later than the true value, while that for the PMT with more PEs was earlier than the true value. This problem might be due to the large decay time constant of the slow liquid scintillator. The PEs are distributed over a wide range of time. Therefore the first PE time will be much earlier if there are more PEs on this PMT. This effect does not exist when the mean values of PEs for all the PMTs are identical. If not, the calibration result will have a bias. A PE number cut is useful to reduce the bias, as demonstrated in Figure 5.19.

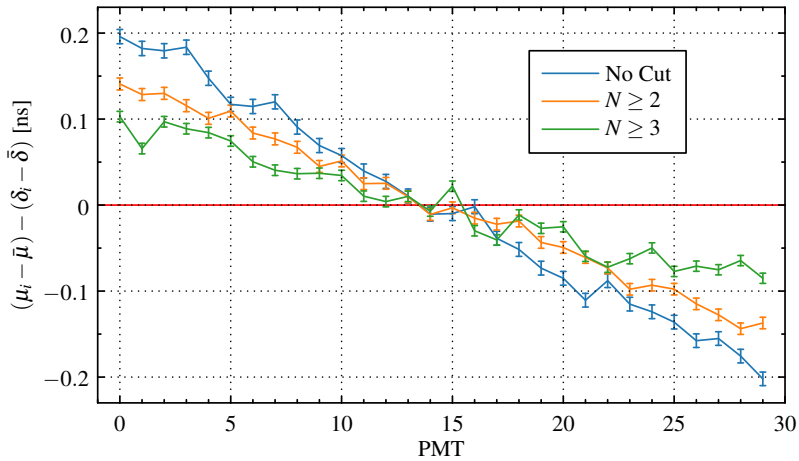


Figure 5.19 The difference between $\mu_i - \bar{\mu}$ and $\delta_i - \bar{\delta}$ varies with the PMT ID, when the PMTs have different PEs for each other. Different cuts were applied.

5.3.2 Event selection

After the good run selection, low-level cuts were applied to separate appropriate high energy events for the time calibration,

- All 30 channels were triggered.
- The pedestal and the fluctuation of the pedestal were in the normal range, to remove electronic noise.
- Total PE number was between 180 PEs and 1000 PEs, to select high energy and point-like events.
- The distance between the barycenter of PEs and the center of the detector was less than 200 mm. The barycenter $\hat{\mathbf{r}}$, which is an estimation of vertex position, is defined as

$$\hat{\mathbf{r}} = \frac{3}{2} \cdot \frac{\sum_{i=1}^N q_i \mathbf{r}_i}{\sum_{i=1}^N q_i} \quad (5-48)$$

where q_i is the number of PEs on PMT i , \mathbf{r}_i is the position of PMT i . The detail can

be found in Section 5.4.

The waveform around the first peak $[-25 \text{ ns}, 3 \text{ ns}]$ was fitted by a Gaussian function,

$$f = H \exp \left[-\frac{(t - t_0)^2}{2\sigma^2} \right] \quad (5-49)$$

The 10% peak position gave the arrival time t_i to estimate the first PE time. The rise-time of PMT i was subtracted by the time of flight,

$$t_{\text{TOF},i} = \frac{|\hat{\mathbf{r}} - \mathbf{r}_i|}{c/n} \quad (5-50)$$

where $n = 1.5$ is the refractive index. Then a series of high-level cuts were applied,

- The number of valid channels (passing all the cut criteria above) ≥ 20 .
- The fit should be converged.
- The fitted H was in the range of $[-300 \text{ ADC} \cdot \text{ns}, -5 \text{ ADC} \cdot \text{ns}]$.
- The fitted σ is in the range of $[1 \text{ ns}, 7 \text{ ns}]$.
- $\chi^2 < 200$.
- The arrival time was in the range of $[100 \text{ ns}, 300 \text{ ns}]$ to avoid dark noise and after-pulse.
- The number of PEs was larger than 6. Figure 5.20 shows the variation of the calibration result $\mu_i - \bar{\mu}$ along with the PE number cut. The result of small PE number PMTs (PMT 19, 13) decreased when increasing the cut value because the calibration result was larger than the actual value, vice versa for the large PE number PMTs (PMT 8, 21), as expected in Figure 5.19. Other PMTs had a similar pattern.

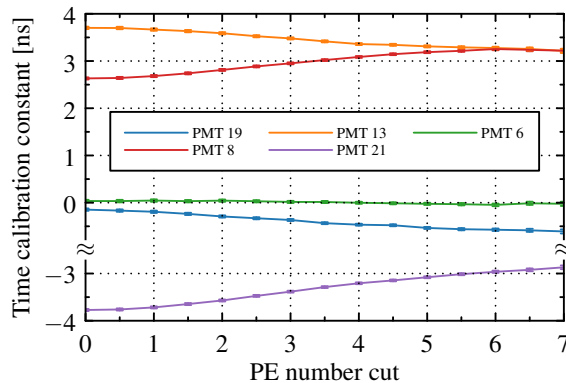


Figure 5.20 The calibration result $\mu_i - \bar{\mu}$ varies with the PE number cut. The plot is made by applying all the rest cuts except the one being studied. The dataset is from Run 1904 to 1910.

5.3.3 An example of calibration result

Figure 5.21 shows an example of $\Delta t_i = t_i - \bar{t}$ distribution, in which the zero-centered mean value of this distribution $\mu_i - \bar{\mu}$ gives the calibration result. The result of dataset Run 1904 to 1910 is shown in Figure 5.22.

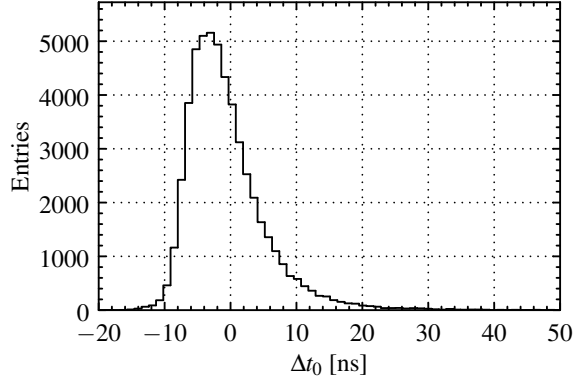


Figure 5.21 The $\Delta t_i = t_i - \bar{t}$ distribution for PMT #0. The dataset is from Run 1904 to 1910.

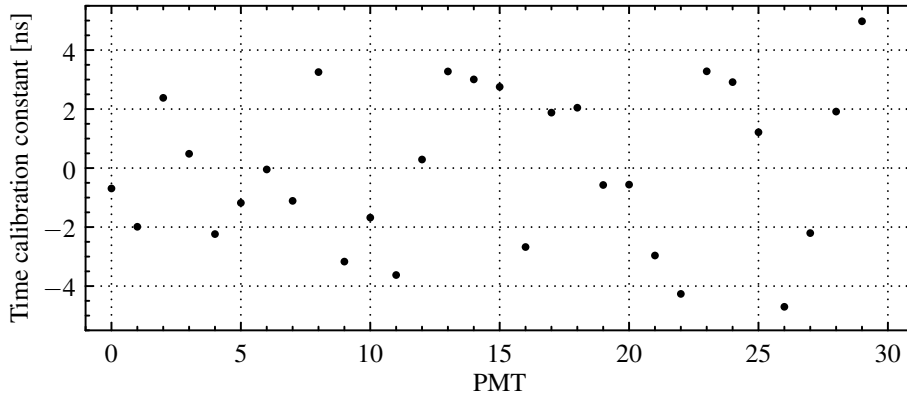


Figure 5.22 The calibration result $\mu_i - \bar{\mu}$ varies with the PMT ID for the data from Run 1904 to 1910. The error of mean value estimation is also shown in the plot. The error is small so it's invisible on some data points.

5.4 Vertex reconstruction

The vertex reconstruction is complicated because the optical condition is involved. One of the most straightforward vertex position reconstruction algorithm for a rough estimation is the charge-weighted average (or barycenter) method, which gives the vertex vector $\hat{\mathbf{r}}$ as

$$\hat{\mathbf{r}} = c \cdot \frac{\sum_{i=1}^N q_i \mathbf{r}_i}{\sum_{i=1}^N q_i} \quad (5-51)$$

where q_i is the number of PEs on PMT i , \mathbf{r}_i is the position of PMT i , c is the correction factor. The reconstruction gives the vertex from the charge-weighted average of PMT positions.

The correction factor c varies from different detectors. We can show that $c = 3/2$ for an ideal spherical detector. As shown in Figure 5.23, the radius of this detector is R , and the photocathode coverage is 100%. A vertex A is placed at $z = a$, emitting optical photons. The photons hit on the inner surface of the detector and generate photoelectrons. The total number of photoelectrons is Q .

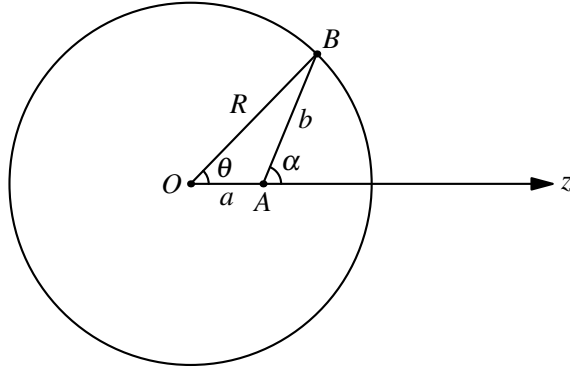


Figure 5.23 An ideal spherical detector. The vertex is placed at A .

The PE density of point $B(R, \theta, \phi)$ is

$$\sigma = Q \cdot \frac{d\Omega}{4\pi} \frac{1}{dS} = Q \cdot \frac{dS \cos(\alpha - \theta)}{4\pi b^2} \frac{1}{dS} = \frac{Q}{4\pi} \frac{\cos(\alpha - \theta)}{b^2} \quad (5-52)$$

Use the law of Sines and Cosines to represent b with the combination of a, θ, R , we obtain

$$\sigma = \frac{Q}{4\pi} \cdot \frac{R - a \cos \theta}{(a^2 + R^2 - 2aR \cos \theta)^{3/2}} \quad (5-53)$$

The reconstruction is to calculate the charge-weighted average of PMT positions,

$$\hat{\mathbf{r}} = \frac{c}{Q} \int \mathbf{r} \sigma dS \quad (5-54)$$

According to the symmetry, only the z component of the PMT position $r_z = R \cos \theta$ is not eliminated. The integral can be simplified to a scalar

$$\hat{r} = \frac{c}{Q} \int R \cos \theta \sigma dS = \frac{c}{Q} \iint R \cos \theta \sigma \sin \theta d\theta d\phi \quad (5-55)$$

Carry out this integral, we get

$$\hat{r} = \frac{2}{3} c a \quad (5-56)$$

Therefore the correction factor c is $3/2$.

Note that this method does not consider the optical attenuation effect. In the previous measurement, we have found that the attenuation length was about 10 m, which was much larger than the detector scale of 0.645 m. The optical attenuation effect was, therefore, negligible.

The total reflection near the acrylic vessel induced another bias. Figure 5.24 compares the truth value from the MC simulation and the reconstruction value for 1.461 MeV gamma ray events. The reconstruction is reliable for the events in the center of the detector. However, the bias is significant for $R > 500$ events and needs more studies for the reconstruction method.

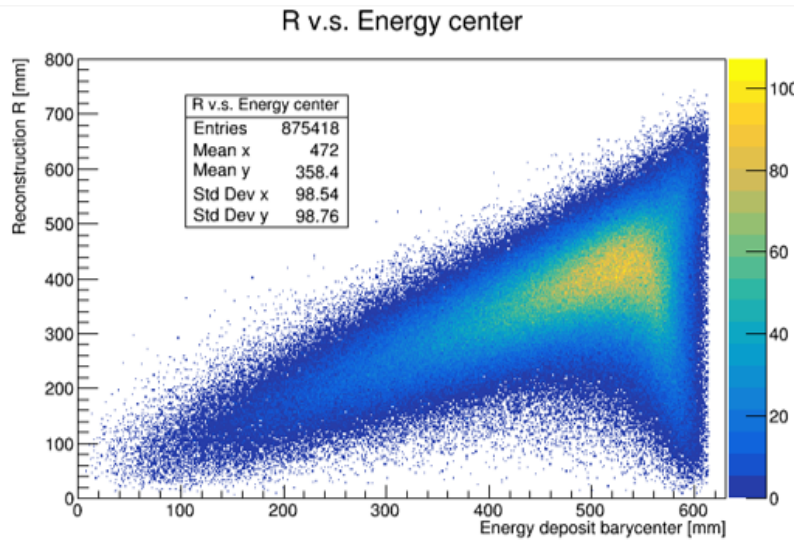


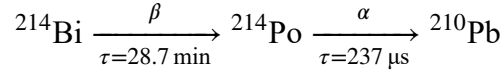
Figure 5.24 The comparison of the truth value from the MC simulation (x axis) and the reconstruction value (y axis) for 1.461 MeV gamma ray events.

5.5 Energy scale calibration

The energy scale calibration is to find how many PEs for a 1 MeV energy deposit in the detector. There are two calibration methods: 1) put a point-like artificial radioactive source in the detector, 2) use the uniform intrinsic radioactive background in the detector, such α decay in the decay chains. We used the latter method, which could provide a real-time calibration without radioactive sources or dedicated calibration runs.

Using an α decay background in the scintillator can give an approach for the energy scale calibration. ^{214}Bi cascade decay events can form a clean sample using coincidence

criteria as follows



A ${}^{214}\text{Bi}$ nucleus decays to ${}^{214}\text{Po}$ through β decay. Sequentially, the daughter ${}^{214}\text{Po}$ nucleus decays to ${}^{210}\text{Pb}$ through α decay. The ${}^{214}\text{Po}$'s half life is as short as $164 \mu\text{s}$. Therefore, the time of prompt β decay signal is close to that of the delayed α signal. The time difference between these two decays should obey an exponential distribution with $\tau = 164.3/\ln 2 = 237 \mu\text{s}$.

The water phase of the 1-ton prototype ended in July 2017, and the acrylic vessel was refilled with liquid scintillation later. During the water-liquid scintillator replacement operation, radon in the laboratory leaked into the detector. The half-life of ${}^{222}\text{Rn}$ is only 3.8 days, so the radon contamination peaked at the beginning of the LS phase. ${}^{214}\text{Bi}$ is the daughter of ${}^{222}\text{Rn}$ decay. The ${}^{214}\text{Bi}$ cascade decay events were abundant from Run 257 to Run 290. In this section, we search for ${}^{214}\text{Bi}$ candidates in this period to determine the cut criteria.

The first cut was to use a data-quality check to remove obvious noise. This run to be analyzed should be in the good run list. The pedestal and fluctuation of the pedestal should be close to the reference value.

A temporal coincidence cut selected the calibration sample. The time difference between prompt and delayed signal, notated as Δt , should be less than $1500 \mu\text{s}$. Figure 5.25 gives the Δt distribution of double coincidence events passing the data-quality check, showing an exponential behavior for the ${}^{214}\text{Bi}$ cascade decay events.

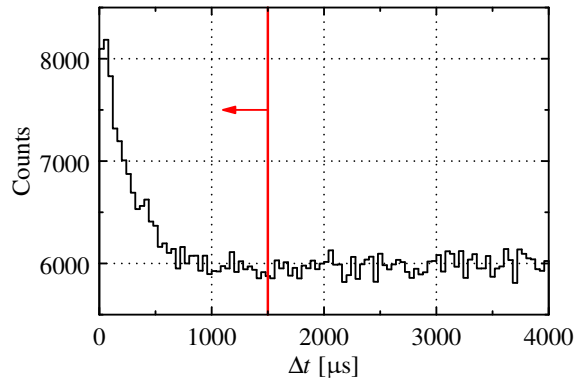


Figure 5.25 The time difference Δt distribution. The dataset is Run 257. Only data-quality check cut is applied.

Figure 5.26 shows the distribution of prompt and delayed PE numbers after the tem-

poral coincidence cut, with a weak peak on the left indicating the ^{214}Bi cascade decay events.

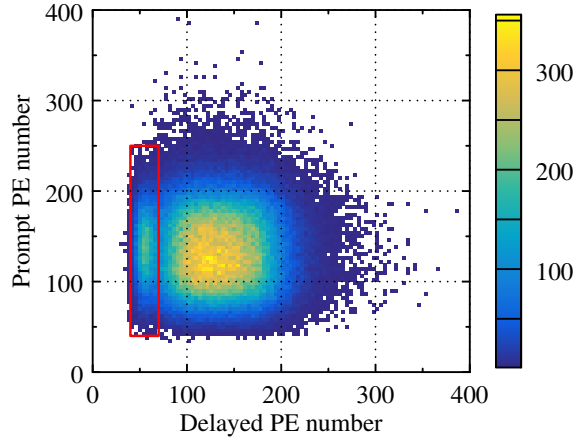


Figure 5.26 The distribution of prompt and delayed PE numbers after the temporal coincidence cut. The dataset is Run 257. ^{214}Bi cascade decay events are indicated in the red box.

Spatial coincidence cut can improve the signal-to-noise ratio. The daughter nucleus should be very close to the parent nucleus. The distance between the prompt vertex and delayed vertex, notated as d , should satisfy $d < 200$ mm. Figure 5.27 shows the distribution of prompt and delayed PE numbers after the spatial coincidence cut, with an improved signal-to-noise ratio.

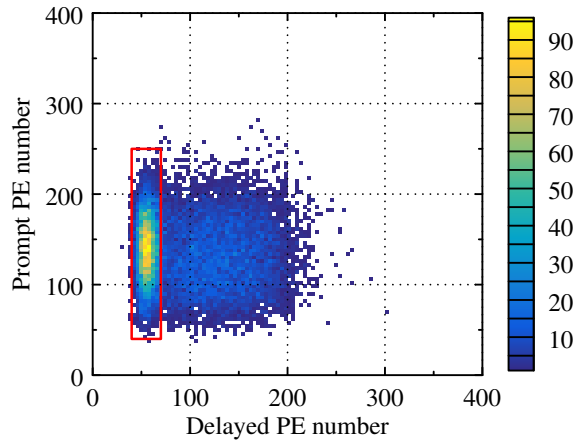


Figure 5.27 The distribution of prompt and delayed PE number after the temporal and spatial coincidence cut. The dataset is Run 257. ^{214}Bi cascade decay events are indicated in the red box.

Using the PE number cut removed the accidental coincidence background. The energy of the prompt electron is a continuous spectrum, and most of the electron is in the range of 1.5 ~ 3.5 MeV. The energy of delayed alpha is 7.687 MeV. After the quenching effect in the scintillator, the visible alpha energy ≈ 1 MeV. Figure 5.28 and Figure 5.29

show the PE number distribution of prompt and delayed signal after applying all the rest cuts, and lines indicating the cut criteria: $40 < n_{\text{prompt}} < 250$ and $40 < n_{\text{delayed}} < 70$.

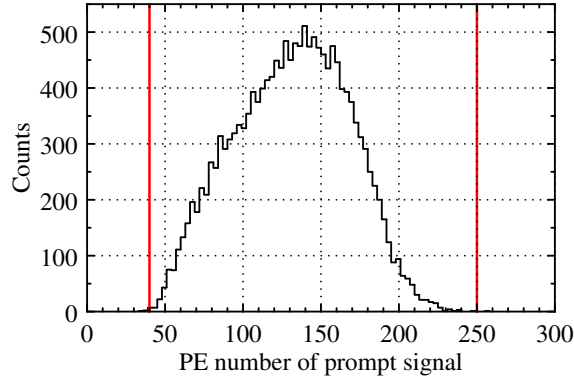


Figure 5.28 PE number distribution of prompt electron signal. The dataset is Run 257 to Run 290. The plot is made by applying all the rest cuts except the one being studied.

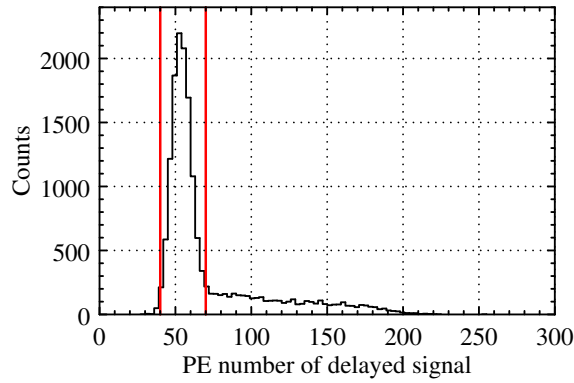


Figure 5.29 PE number distribution of the delayed alpha signal. The dataset is Run 257 to Run 290. The plot is made by applying all the rest cuts except the one being studied.

Figure 5.30 shows the Δt distribution after applying all cuts. The fitting function is an exponential distribution with background,

$$f(t) = B + Ne^{-t/\tau} \quad (5-57)$$

The fit result $\tau = (235.4 \pm 4.2) \mu\text{s}$ is consistent with the decay time constant of ^{214}Po $237 \mu\text{s}$, indicating that we have selected ^{214}Bi cascade decay events.

The 1-MeV visible energy deposit of the delayed alpha signal corresponds to a $50 \sim 60$ PE response in the slow scintillator, as shown in Figure 5.29. To figure out the precise value of the energy scale factor, we need more than one calibration source, such as ^{208}Tl and ^{212}Bi . The full energy scale calibration is still under study.

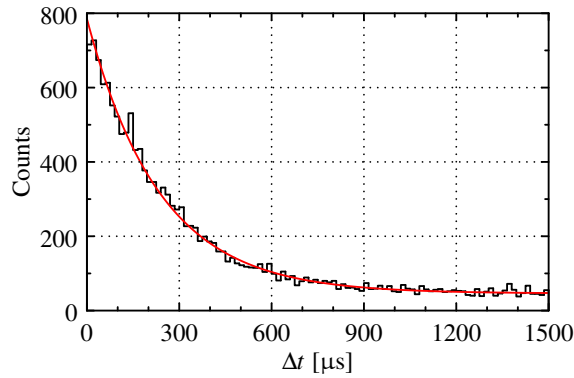


Figure 5.30 Δt distribution after applying all cuts. The dataset is Run 257 to Run 290.

5.6 Čerenkov light search

Although pure water neutrino experiments have a mature Čerenkov light search, there is no such a study in slow scintillators. Here we report our study.

5.6.1 Analysis method

We have separated the scintillation and Čerenkov light of high energy muon events of 20 L detector in Chapter 2. In this section, we try to search the evidence of Čerenkov light in low energy events of the 1-ton prototype. ^{214}Bi cascade decay events form excellent samples because the energy of prompted electron signal exceeds the Čerenkov threshold, and the delayed alpha signal does not. The comparison between alpha and beta signals can show evidence of Čerenkov light. The Čerenkov/scintillation PEs are separable in the time profile. Unfortunately, a time synchronization problem before Run 1680 ruined the time resolution of most data. After fixing this problem, more data are necessary to complete this study. Here we use the simulation data to study the evidence of Čerenkov photons.

Section 5.4 has already pointed out that the vertices around the detector center have a more reliable reconstruction performance. It is because the ^{214}Bi cascade decay events have a more uniform light emission. The light is not affected by total reflection on the acrylic vessel surface when it propagates from the acrylic vessel to the buffer water. If the vertex is far from the detector center, the incident angle of light exceeds the total reflection angle, resulting in a transmission loss, which disturbs the vertex reconstruction and time profile of photoelectrons. Therefore, a distance between the event vertex and the detector center should be less than 200 mm to get rid of this problem.

A waveform analysis approach is to fit the waveform and give the time of each pho-

toelectron. The template of a single photoelectron waveform is given by

$$f(t) = A_0 \cdot \frac{1}{2\tau} \exp\left(\frac{\sigma^2}{2\tau^2} - \frac{t}{\tau}\right) \operatorname{erfc}\left(\frac{\sigma}{\sqrt{2\tau}} - \frac{t}{\sqrt{2\sigma}}\right) \quad (5-58)$$

where A_0 is the single PE charge, σ and τ are the shape parameters. A complete waveform is the superposition of several photoelectrons waveforms,

$$W(t; n, A_i, T_i) = \sum_{i=1}^n A_i f(t - T_i) \quad (5-59)$$

assuming there are n PEs in this waveform, A_i and T_i are the charge and time of PE i , respectively. For simplicity, the shape parameters σ and τ were fixed in this fit.

There are $(2n + 1)$ parameters to be fitted for a waveform: n, A_i, T_i ($i = 1, 2, \dots, n$). Considering the waveform acquired from FlashADC is a discrete digital time signal, let $\mathbf{V} = (V_0, V_1, \dots, V_m)$ is the waveform of real data, $\mathbf{W} = (W(0), W(1), \dots, W(m))$ is the fit function. The probability (or likelihood function) of the waveform to be \mathbf{V} under the assumption of $W(t; n, A_i, T_i)$ is given by

$$\mathcal{L}(\mathbf{V}|n, A_i, T_i) = \prod_j \operatorname{Gauss}[V_j - W(j), \sigma] \cdot \frac{\mu^n e^{-\mu}}{n!} \quad (5-60)$$

The first term stands for the Gaussian noise of baseline, and the second term is the Poisson assumption of PE number, where μ is the predicted PE number from PMT gain calibration.

The Minimization of negative log-likelihood,

$$-\log \mathcal{L} \propto \frac{1}{2\sigma^2} \sum_j [V_j - W(j; n, A_i, T_i)]^2 + n \log \mu - \mu - \log n! \quad (5-61)$$

gives the fit result n, A_i, T_i . Figure 5.31 shows an example of fit. The PE time has been subtracted by the time of flight for the next analysis.

5.6.2 Statistical separation between lights

The study of Čerenkov light separation from the scintillation light in the 1-ton prototype is more complicated than that of cosmic-ray muon events in the 20 L detector in Chapter 2. Since there was no calibration source, for example, an electron beam, we did not know the electron direction and the PMTs fired by Čerenkov photons. Due to the limited PMT coverage, we could only conduct a statistical approach without the directional information.

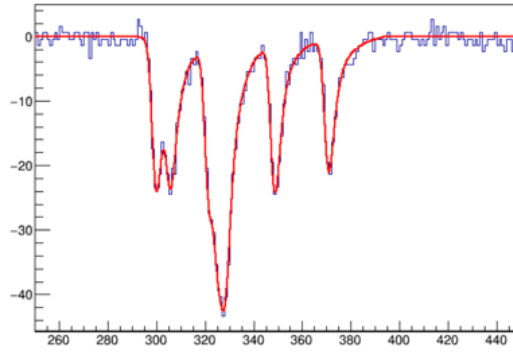


Figure 5.31 An waveform fit example.

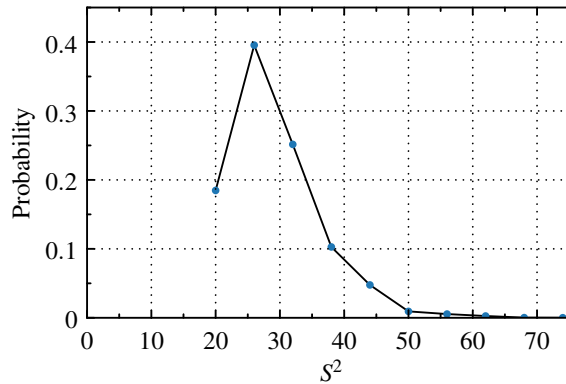
We defined an estimator, using the number of PEs to describe the light uniformity on the 30 PMTs. This estimator is

$$S^2 = \sum_{i=0}^{29} \frac{(q_i - \bar{q})^2}{\bar{q}} \quad (5-62)$$

where q_i is the number of PEs for PMT i , and $\sum_{i=0}^{29} q_i = N$, q_i obeys a multinomial distribution, $\bar{q} = \frac{1}{30} \sum_{i=0}^{29} q_i = N/30$ is the average number of PEs for each PMT. Eq. (5-62) can be written in an explicit form,

$$S^2 = \frac{30}{N} \sum_{i=0}^{29} q_i^2 - N \quad (5-63)$$

We performed Monte Carlo simulations to study the properties of S^2 . In the scintillation case, q_i is distributed uniformly on the 30 PMTs. Figure 5.32 shows the distribution of S^2 of a simulation result for $N = 10$. Because N and q_i are integers, the distribution of S^2 is discrete.


 Figure 5.32 The distribution of S^2 in the uniform case. Made by a toy Monte-Carlo simulation.

we also did a detector simulation to study the S^2 distribution for electron events.

The typical energy of prompt electron signal is ~ 2 MeV or ~ 120 PEs. We simulated 2 MeV isotropic electrons in the detector center. The simulation result shows that there are about four detectable Čerenkov PEs in the 1-ton prototype. Although the Čerenkov-to-scintillation ratio is only 1 : 30, the slow liquid scintillator has a long decay time constant, spreading the 120 PEs in an extensive period and resulting in a large ratio for the first several PEs.

We added a 1 ns Gaussian smearing on the PE time to simulate the uncertainty on the time of flight correction and PMT time calibration. Figure 5.33 shows the average Čerenkov-to-scintillation ratio for the first N PEs before/after the smearing. Among the first 10 PEs, the Čerenkov-to-scintillation ratio is ~ 0.25 . Also shown is the simulation result for a conventional liquid scintillator (LAB+3 g/L PPO+15 mg/L bis-MSB) without smearing. The corresponding ratio is only 0.1 in the first 10 PEs.

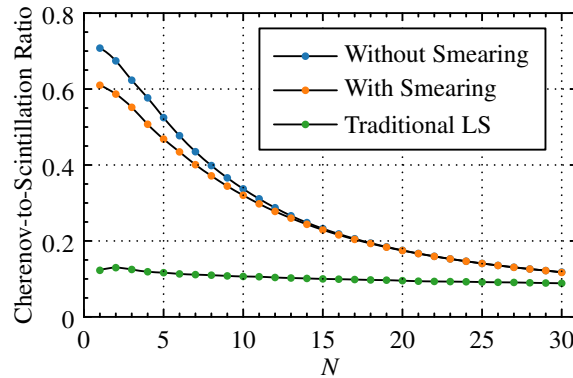


Figure 5.33 The average Čerenkov-to-scintillation ratio for the first N PEs in 2 MeV electron samples.

Since the first 10 PEs carry much more Čerenkov light information, we did a further study by sorting the PEs in sequence. Figure 5.34 shows the χ^2 distribution of the first 10 PEs, 11th~20th PE and 21th~30th PE. We can see that in the scintillation time range (11th~20th PE and 21th~30th PE), the S^2 distribution is close to the uniformly distributed situation, while in the time range containing Čerenkov light (first 10 PEs) the distribution is different.

For the delayed alpha events which do not emit Čerenkov light, we expect a uniform scintillation PE distribution on the total 30 PMTs. Figure 5.35 shows the S^2 distribution for 7.68 MeV alpha events in the detector center. There is no difference in the S^2 distributions among the three group PEs.

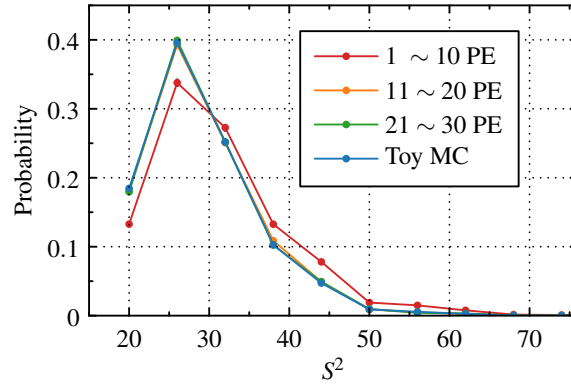


Figure 5.34 The distribution of S^2 for 2 MeV electron events. The error bar is too small to be visible in this plot.

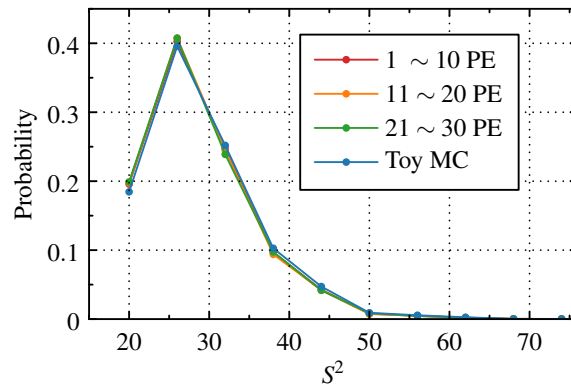


Figure 5.35 The distribution of S^2 for 7.68 MeV alpha events. The error bar is too small to be visible in this plot.

5.7 Summary

In this chapter, we discuss the performance of the 1-ton prototype. We developed a set of analysis methods to calibrate the detector without an external LED or radioactive source, also providing indicators of the detector running status. We simulated ^{214}Bi cascade decay events for the Čerenkov light search. The distribution of S^2 showed the evidence of Čerenkov light.

Chapter 6 Muon Flux Measurement at CJPL

With the data collected by the 1-ton prototype detector and the simulation framework, we performed a study of cosmic-ray background at CJPL-I, which can have a significant impact on the solar neutrino study.

6.1 Simulation of underground muon spectrum and spatial profile

We run a Geant4-based simulation of muon penetration in the mountain rocks to predict the underground muon spectrum.

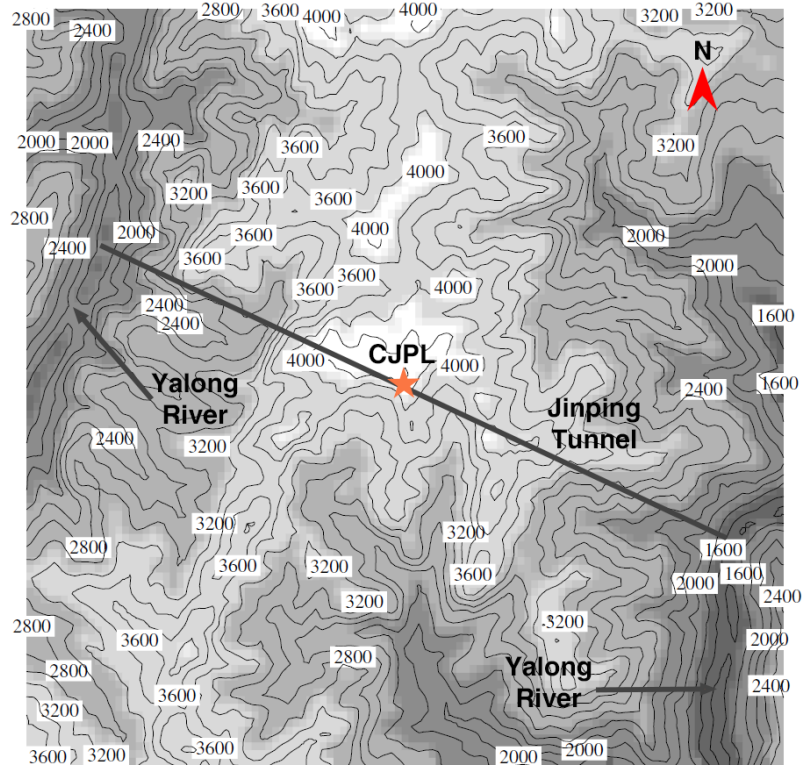
6.1.1 Import the terrain data to Geant4

CJPL has a mountain overburden, and the peak of Jinping mountain is about 4000 m. The elevation of the experiment hall is about 1600 m. We obtained the mountain terrain data from the NASA SRTM3 dataset^[101], as shown in Figure 6.1 for the contour map. We selected 6315 points inside a 9 km radius circle centered at CJPL to ensure that the track length of $\cos \theta > 0.25$ muons is intact.

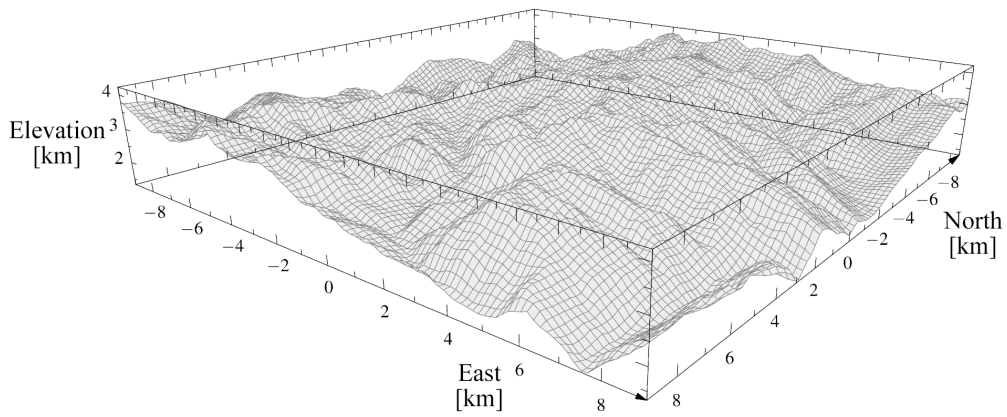
First, we queried the elevation data of 6315 locations near the experiment hall (inside a radius 9 km circle area). Although the terrain data has a steep cut at $R = 9$ km, the track length of $\cos \theta > 0.25$ muons is intact, which is enough for the underground muon simulation.

We applied a Delaunay triangulation on these discrete points to assemble a mesh. Delaunay triangulation is an algorithm to divide discrete points into a set of triangles with the restriction that each triangle side is entirely shared by two adjacent triangles, as shown in Figure 6.2. Mathematics software such as MATLAB and Mathematica provides a standard routine for Delaunay triangulation.

These meshes were assembled to a `G4TessellatedSolid` object in Geant4, as shown in Figure 6.3. The rock density is 2.8 g/cm^3 , so the water equivalent depth is 6720 m for 2400 m rock. The composition of the rock in the simulation adopted the abundance of elements in Earth's crust (percentage by weight)^[102]: oxygen (46.1%), silicon (28.2%), aluminum (8.2%), and iron (5.6%). We added a 5% variation of rock density in the simulation to model the influence of rock density uncertainty.



(a) The contour map near CJPL



(b) The 3D model of Jinping Mountain.

Figure 6.1 Terrain map near CJPL, as given by the SRTM3.

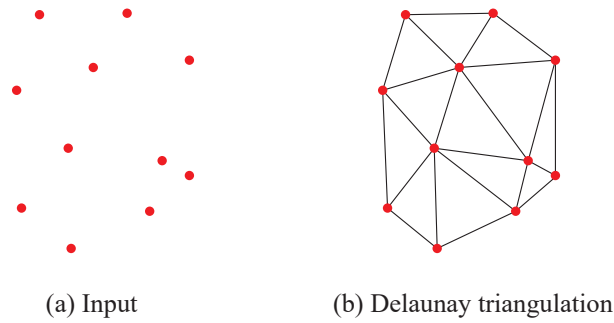


Figure 6.2 An example of two-dimensional Delaunay triangulation.

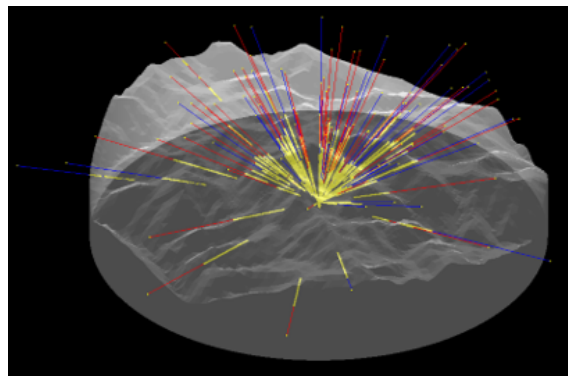


Figure 6.3 The 3D solid entity of mountain imported in Geant4.

To study the cosmic-ray muon penetration in the rock, we enabled the standard electromagnetic and muon-nucleus physics processes in Geant4.

6.1.2 Muon generator

To simulate the cosmic-ray muons, we wrote a physics generator for Geant4.

6.1.2.1 Muon spectrum in the atmosphere

In this chapter, “muon direction” stands for the direction which muon comes from, i.e., the opposite of the muon momentum vector, represented by zenith angle θ and azimuth angle ϕ . For example, a vertical muon from the sky to the ground has a zenith angle of $\theta = 0$, or $\cos \theta = 1$. Due to the property of charged lepton, the dominant process is minimum ionization. The muon track in the rocks is almost a straight line. We could thus treat that there was no difference between the initial position of a muon with direction (θ, ϕ) and the detected (θ, ϕ) .

Gaisser’s formula^[103] describes the cosmic-ray muon flux and spectrum at the sea-

level,

$$\frac{dN}{dEd\Omega} \approx \frac{I_0}{\text{cm}^2 \cdot \text{s} \cdot \text{sr} \cdot \text{GeV}} \cdot \left(\frac{E}{\text{GeV}} \right)^{-\gamma} \cdot \left(\frac{1}{1 + \frac{1.1E \cos \theta}{115\text{GeV}}} + \frac{0.054}{1 + \frac{1.1E \cos \theta}{850\text{GeV}}} \right) \quad (6-1)$$

where E is the muon kinetic energy, θ is the zenith angle, I_0 is a normalization constant, $\gamma = 2.7$ is the muon spectral index.

Eq. (6-1) is divergent at low energy and inaccurate at large zenith angles. Ref^[74] proposed a modified Gaisser's formula by parametrization,

$$G(E, \theta, \phi) \equiv \frac{dN}{dEd\Omega} = \frac{I_0}{\text{cm}^2 \cdot \text{s} \cdot \text{sr} \cdot \text{GeV}} \cdot \left(\frac{E^*}{\text{GeV}} \right)^{-\gamma} \cdot \left(\frac{1}{1 + \frac{1.1E \cos \theta^*}{115\text{GeV}}} + \frac{0.054}{1 + \frac{1.1E \cos \theta^*}{850\text{GeV}}} \right) \quad (6-2)$$

where

$$I_0 = 0.14, \quad E^* = E \left[1 + \frac{3.64 \text{ GeV}}{E \cdot (\cos \theta^*)^{1.29}} \right]$$

$$\cos \theta^* = \sqrt{\frac{\cos^2 \theta + P_1^2 + P_2(\cos \theta)^{P_3} + P_4(\cos \theta)^{P_5}}{1 + P_1^2 + P_2 + P_4}},$$

$$P_1 = 0.102573, \quad P_2 = -0.068287, \quad P_3 = 0.958633,$$

$$P_4 = 0.0407253, \quad P_5 = 0.817285,$$

The muon kinetic energy in Eq. (6-2) spreads in many orders of magnitude, from MeV to TeV. The spectrum detail in the part of low energy will be lost if using the ROOT routine `TF2::GetRandom2` for sampling. It is more feasible to sample from the logarithmic form of Eq. (6-2), i.e., sample $u = \log E$ from $\tilde{G}(u)$ instead of sampling E directly from $G(E)$. The new function $\tilde{G}(u)$ becomes

$$\tilde{G}(u) = G(E) \left| \frac{dE}{du} \right| = G(e^u) \cdot e^u \quad (6-3)$$

Eq. (6-1) is a typical spectrum estimation at sea-level and is not precise for low energy and large zenith angle. Meanwhile, the altitude effect should be considered because

the initial muons in the simulation were generated in the high elevation ($\sim 4,000$ m). Ref.^[104] indicated that the differential flux of high energy (> 40 GeV) and small zenith angle muons depends barely on altitude. The minimum energy required for the muons to reach the experiment hall is approximately 3 TeV. The cosine of the zenith angles are larger than 0.4 for most of these muons, as discussed in the next section. Figure 6.4 shows the initial kinetic energy and cosine zenith angle distribution of the survival muons. Therefore, the inaccuracy of Eq. (6-1) and the altitude effect do not affect the underground muon spectrum simulation.

6.1.2.2 Minimal initial energy of underground muons

The simulation efficiency is quite low because only a few high energy and small zenith angle muons can reach the underground laboratory. We can only generate high energy muons to increase efficiency. To figure out the threshold for underground muons entering the laboratory, we should study the muon energy loss in the rock.

We can write the energy loss rate for muons^[103] as

$$\frac{dE}{dX} = -\alpha - \frac{E}{\xi} \quad (6-4)$$

where $\alpha \approx 2 \text{ MeV}/(\text{g} \cdot \text{cm}^{-2})$ is the ionization loss, E/ξ is the discrete energy loss (bremsstrahlung, pair production, etc.), $\xi \approx 2.5 \times 10^6 \text{ g/cm}^2$. The ionization energy loss rate for relativistic muons has a broad minimum below 1 GeV (or *minimum ionizing*) and rises slowly at higher energy. An approximate numerical formula for ionization loss of muons in rock^[103] is

$$\alpha = \frac{dE_{\text{ion}}}{dX} \approx - \left(1.9 + 0.08 \ln \frac{E}{m_{\mu}} \right) \quad (6-5)$$

If we treat α as a constant, the general solution of Eq. (6-4) is

$$\langle E(X) \rangle = (E_0 + \epsilon) e^{-X/\xi} - \epsilon \quad (6-6)$$

where $\langle E(X) \rangle$ is to be interpreted as the mean energy of a beam of muons of the initial energy E_0 after penetrating a depth X of material^[103], $\epsilon \equiv \alpha\xi$ is the turning point of discrete and continuous energy loss domination. The minimum energy required of a muon at the surface to reach slant depth X could be obtained by letting the left side of Eq. (6-6) equals zero,

$$E_0^{\text{min}} = \epsilon (e^{X/\xi} - 1) \quad (6-7)$$

For the 2400 m rock overburden at CJPL, the minimum energy of the vertical going primary muons is

$$E_0^{\min} = \epsilon (e^{x/\xi} - 1) = 500 \text{ GeV} \times \left[\exp \left(\frac{2400 \text{ m} \times 2.8 \text{ g/cm}^3}{2.5 \times 10^5 \text{ g/cm}^2} \right) - 1 \right] = 6851 \text{ GeV}$$

This number is in the TeV order of magnitude. For muons traveling in a slant depth, the threshold is higher. The energy loss in a material is a stochastic process, and even a few muons below this energy can reach the underground laboratory. Simulation is needed to find a more precise threshold. The simulation result in Figure 6.4 shows that the muon generator's energy and zenith angle constraint can be set to

$$E > 2200 \text{ GeV}, \quad \cos \theta > \frac{2}{\left(\log_{10} \frac{E}{\text{GeV}} - 2 \right)^{3.5}} + 0.15 \quad (6-8)$$

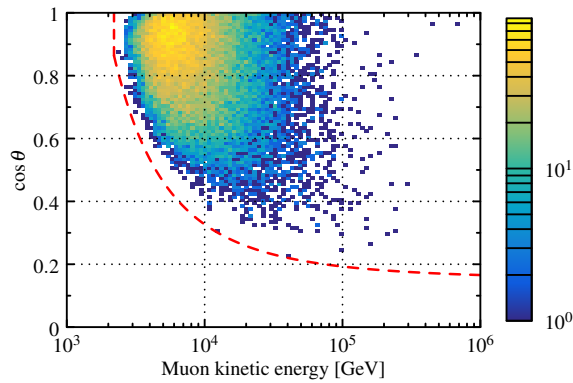


Figure 6.4 Initial kinetic energy and cosine zenith angle distribution for the muons reaching the experiment hall. Red line is Eq. (6-8).

6.1.3 Simulation result

The simulation result the kinetic energy and angular distribution of survival underground muons, as shown in Figure 6.5 and 6.6.

6.2 Detector simulation

6.2.1 Muon rate of a volume

All the flux discussed in the previous sections corresponds to the number of events passing through a horizontal surface. As shown in Figure 6.7, if we try to simulate the detector efficiency, we should create a box to cover the detector and generate muons on five surfaces (exclude the bottom surface).

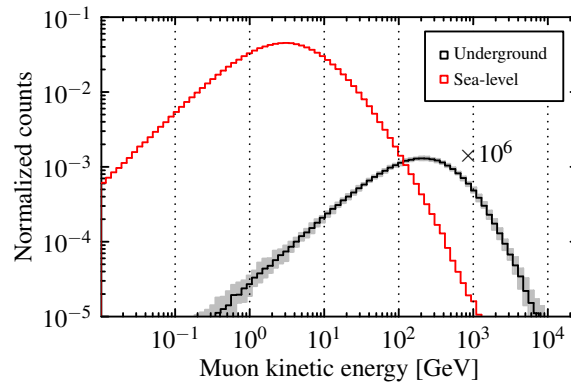


Figure 6.5 Simulated underground muon kinetic energy. The mean value is 340 GeV. The gray band shows the 1σ uncertainty induced by rock density and detector location.

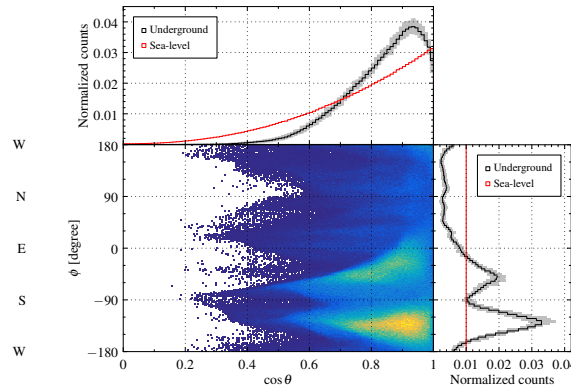


Figure 6.6 Simulation result of underground muon direction (θ, ϕ) . The gray band shows the 1σ uncertainty induced by rock density and detector location.

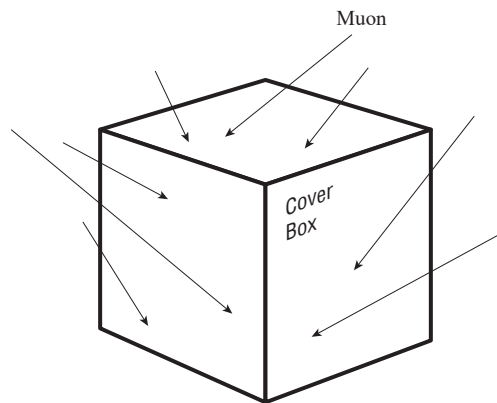


Figure 6.7 Cover box of a detector. Muons should be generated on the surfaces of the box.

6.2.1.1 Projection area of a plane

The muon rate passing through a plane A is equivalent to the muon rate on its projection plane, i.e., the gray area in Fig. 6.8. We should try to calculate the projection area on XOY plane of a plane A with the muon beam direction (θ, ϕ) . Assuming the normal direction of A is (α, β) , e.g., the normal vector is $(\sin \alpha \cos \beta, \sin \alpha \sin \beta, \cos \alpha)^T$.

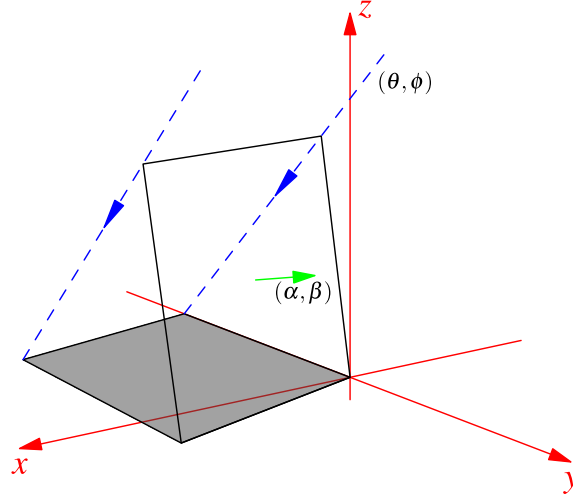


Figure 6.8 Project area (gray) of a surface.

Plane A could be treated as a rotation result of XOY plane. The normal vector is rotated from $\mathbf{a} = (0, 0, 1)^T$ to $\mathbf{b} = (\sin \alpha \cos \beta, \sin \alpha \sin \beta, \cos \alpha)^T$. The rotation matrix is given by Rodrigues' rotation formula, which is an efficient algorithm for rotating a vector in space, given a normalized axis \mathbf{k} and angle of rotation Θ . The rotation matrix is given by

$$R = I + K \sin \Theta + K^2(1 - \cos \Theta) \quad (6-9)$$

where K is the skew-symmetric *cross-product matrix* of \mathbf{k} ,

$$K = \begin{pmatrix} 0 & -k_z & k_y \\ k_z & 0 & -k_x \\ -k_y & k_x & 0 \end{pmatrix} \quad (6-10)$$

The cross-product matrix converts cross product to matrix vector multiplication, i.e., for any vector \mathbf{v}

$$\mathbf{k} \times \mathbf{v} = K \mathbf{v} \quad (6-11)$$

In our situation, the axis \mathbf{k} is given by

$$\mathbf{k} = \frac{\mathbf{a} \times \mathbf{b}}{\|\mathbf{a} \times \mathbf{b}\|} = \begin{pmatrix} -\sin \beta \\ \cos \beta \\ 0 \end{pmatrix} \quad (6-12)$$

and the angle Θ is given by

$$\cos \Theta = \mathbf{a} \cdot \mathbf{b} = \cos \alpha, \quad \sin \Theta = \|\mathbf{a} \times \mathbf{b}\| = \sin \alpha \quad (6-13)$$

Therefore the rotation matrix is

$$R = \begin{pmatrix} (\cos \alpha - 1) \cos^2 \beta + 1 & (\cos \alpha - 1) \sin \beta \cos \beta & \sin \alpha \cos \beta \\ (\cos \alpha - 1) \sin \beta \cos \beta & (\cos \alpha - 1) \sin^2 \beta + 1 & \sin \alpha \sin \beta \\ -\sin \alpha \cos \beta & -\sin \alpha \sin \beta & \cos \alpha \end{pmatrix} \quad (6-14)$$

Then plane A is projected to the XOY plane. The projection matrix P is

$$P = \begin{pmatrix} 1 & 0 & -\tan \theta \cos \phi \\ 0 & 1 & -\tan \theta \sin \phi \\ 0 & 0 & 0 \end{pmatrix} \quad (6-15)$$

Assuming a unit square on XOY plane, we have

$$\mathbf{A}_1(0, 0, 0)^T \rightarrow \mathbf{A}_2(1, 0, 0)^T \rightarrow \mathbf{A}_3(1, 1, 0)^T \rightarrow \mathbf{A}_4(0, 1, 0)^T$$

the area is $S_0 = 1$. After the rotation and projection, these four vertices are

$$\mathbf{A}'_i = P R \mathbf{A}_i$$

$$\mathbf{A}'_1 = P R \begin{pmatrix} 0 \\ 0 \\ 0 \end{pmatrix} = \begin{pmatrix} 0 \\ 0 \\ 0 \end{pmatrix}$$

$$\mathbf{A}'_2 = P R \begin{pmatrix} 1 \\ 0 \\ 0 \end{pmatrix} = \begin{pmatrix} \sin \alpha \cos \beta \tan \theta \cos \phi + (\cos \alpha - 1) \cos^2 \beta + 1 \\ \sin \alpha \cos \beta \tan \theta \sin \phi + (\cos \alpha - 1) \sin \beta \cos \beta \\ 0 \end{pmatrix}$$

$$\mathbf{A}'_3 = PR \begin{pmatrix} 1 \\ 1 \\ 0 \end{pmatrix} = \begin{pmatrix} \cos \beta((\cos \alpha - 1) \sin \beta + \sin \alpha \tan \theta \cos \phi) + \\ \sin \alpha \sin \beta \tan \theta \cos \phi + (\cos \alpha - 1) \cos^2 \beta + 1 \\ \sin \alpha \sin \beta \tan \theta \sin \phi + \cos \beta((\cos \alpha - 1) \sin \beta + \\ \sin \alpha \tan \theta \sin \phi) + (\cos \alpha - 1) \sin^2 \beta + 1 \\ 0 \end{pmatrix}$$

$$\mathbf{A}'_4 = PR \begin{pmatrix} 0 \\ 1 \\ 0 \end{pmatrix} = \begin{pmatrix} \sin \beta((\cos \alpha - 1) \cos \beta + \sin \alpha \tan \theta \cos \phi) \\ \sin \alpha \sin \beta \tan \theta \sin \phi + (\cos \alpha - 1) \sin^2 \beta + 1 \\ 0 \end{pmatrix}$$

Finally the projection area is

$$S_p = |\sin \alpha \tan \theta \cos(\beta - \phi) + \cos \alpha| \quad (6-16)$$

6.2.1.2 Muon rate of a box or sphere

Assuming that the muon spectrum is $G(E, \theta, \phi)$. Integrate over E , and we get the angular distribution $f(\theta, \phi)$,

$$f(\theta, \phi) = \int_0^{\infty} G(E, \theta, \phi) dE \quad (6-17)$$

Therefore the projection area of plane A is

$$S = \int_{\phi=0}^{2\pi} \int_{\theta=0}^{\frac{\pi}{2}} |\sin \alpha \tan \theta \cos(\beta - \phi) + \cos \alpha| f(\theta, \phi) d \cos \theta d\phi \quad (6-18)$$

The number of muons with $(\cos \theta, \phi)$ changes from $f(\theta, \phi) d \cos \theta d\phi$ to $f(\theta, \phi) S_p d \cos \theta d\phi$. Therefore the muon spectrum on plane A is

$$g(E, \theta, \phi) = G(E, \theta, \phi) |\sin \alpha \tan \theta \cos(\beta - \phi) + \cos \alpha| \quad (6-19)$$

For a box volume with length, width, and height (L, W, H) , the top surface, $\alpha = 0$, $S_p = 1$, this surface has a projection area of

$$S_1 = WL \int_{\phi=0}^{2\pi} \int_{\theta=0}^{\frac{\pi}{2}} f(\theta, \phi) d \cos \theta d\phi \quad (6-20)$$

The muon spectrum on this surface is

$$g_1(E, \theta, \phi) = G(E, \theta, \phi) \quad (6-21)$$

For the four lateral surfaces, $\alpha = \pi/2$. Only when the angle between the muon direction and the normal direction is obtuse, the muon will hit on the surface, or the opposite surface will block the muons. Write down the projection area and spectrum,

$$S_2 = HL \int_{\phi=-\frac{\pi}{2}}^{\phi=\frac{\pi}{2}} \int_{\theta=0}^{\theta=\pi} \tan \theta \cos \phi f(\theta, \phi) d \cos \theta d\phi, \quad (6-22)$$

$$g_2(E, \theta, \phi) = G(E, \theta, \phi) \tan \theta \cos \phi, \quad -\frac{\pi}{2} < \phi < \frac{\pi}{2} \quad (6-23)$$

$$S_3 = -HL \int_{\phi=\frac{\pi}{2}}^{\phi=\frac{3\pi}{2}} \int_{\theta=0}^{\theta=\pi} \tan \theta \cos \phi f(\theta, \phi) d \cos \theta d\phi, \quad (6-24)$$

$$g_3(E, \theta, \phi) = -G(E, \theta, \phi) \tan \theta \cos \phi, \quad \frac{\pi}{2} < \phi < \frac{3\pi}{2} \quad (6-25)$$

$$S_4 = HW \int_{\phi=0}^{\phi=\pi} \int_{\theta=0}^{\theta=\pi} \tan \theta \sin \phi f(\theta, \phi) d \cos \theta d\phi, \quad (6-26)$$

$$g_4(E, \theta, \phi) = G(E, \theta, \phi) \tan \theta \sin \phi, \quad 0 < \phi < \pi \quad (6-27)$$

$$S_5 = -HW \int_{\phi=\pi}^{\phi=2\pi} \int_{\theta=0}^{\theta=\pi} \tan \theta \sin \phi f(\theta, \phi) d \cos \theta d\phi, \quad (6-28)$$

$$g_5(E, \theta, \phi) = -G(E, \theta, \phi) \tan \theta \sin \phi, \quad \pi < \phi < 2\pi \quad (6-29)$$

Here $g_i(\theta, \phi)$ haven't been normalized. Fortunately, there is no need to normalize if we use this function to get random numbers by `TH3::GetRandom()`.

The projection area of the box is

$$S_{\text{box}} = \sum_{i=1}^5 S_i \quad (6-30)$$

The muon rate of this box is integral muon flux (in $\text{cm}^{-2} \cdot \text{s}^{-1}$) times the projection area.

For a sphere volume with radius r , we can easily write down the projection area (an ellipse) for a (θ, ϕ) muon beam due to the spherical symmetry,

$$S = \frac{\pi r^2}{\cos \theta} \quad (6-31)$$

so that

$$S_{\text{sphere}} = \pi r^2 \int_{\phi=0}^{2\pi} \int_{\theta=0}^{\frac{\pi}{2}} \frac{f(\theta, \phi)}{\cos \theta} d \cos \theta d\phi \quad (6-32)$$

or muon rate

$$R_{\text{sphere}} = \pi r^2 \int_{E=0}^{\infty} \int_{\phi=0}^{2\pi} \int_{\theta=0}^{\frac{\pi}{2}} \frac{G(E, \theta, \phi)}{\cos \theta} dE d \cos \theta d\phi \quad (6-33)$$

At sea-level surface $f(\theta, \phi) \approx \frac{3}{2\pi} \cos^2 \theta$, these integrals can be carried out,

$$S_{\text{box}} = WL + \frac{2}{\pi} H(L + W), \quad S_{\text{cube}} = \left(1 + \frac{4}{\pi}\right) a^2 = 2.273a^2, \quad S_{\text{sphere}} = \frac{3}{2} \pi r^2$$

6.2.2 Detector simulation

Figure 6.9 shows the geometry setup with rocks included to simulate the muon showers. Muons were generated on five faces of the 8 m×6 m×5 m rock box.

These following steps were taken in the muon generator:

(i) Before the simulation, we calculated the probability of muon generated on surface S_i

$$r_i = \frac{S_i}{S_{\text{box}}} \quad (6-34)$$

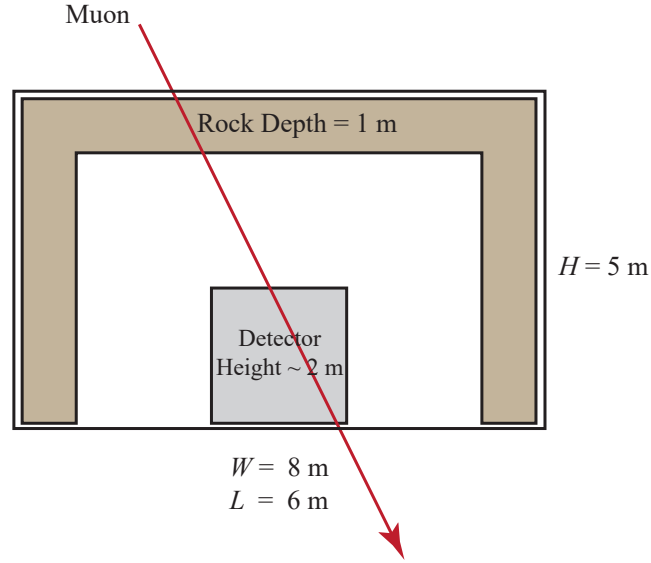


Figure 6.9 Front view of simulation geometry setup.

On the surface S_i , the number of muons in (θ, ϕ) direction was proportional to the projected area $S_{pi}(\theta, \phi)$, so the muon spectrum on surface S_i was given by

$$g_i(E_k, \theta, \phi) = S_{pi}(\theta, \phi) f(E_k, \theta, \phi) \quad (6-35)$$

(ii) Randomly choose which surface the muon will be generated on depending on r_i .

(iii) Generate a muon on the selected surface, the kinetic energy and direction were sampled from $g_i(E_k, \theta, \phi)$.

Repeat the routine for N times and the number of triggers passing the event selection in Sec. 6.3 was M . The global efficiency ϵ was estimated by M/N , which could be decomposed by geometry factor ϵ_g , detection efficiency ϵ_d and shower factor ϵ_s ,

$$\epsilon = \epsilon_g \cdot \epsilon_d + \epsilon_s \quad (6-36)$$

$$\epsilon_g = \frac{N_p}{N}, \quad \epsilon_d = \frac{M_1}{N_p}, \quad \epsilon_s = \frac{M_2}{N} \quad (6-37)$$

where N_p is the number of muons passing through the scintillator, M_1 is the number of muons passing through the scintillator and passing the event selection, M_2 is the number of muons not passing through the scintillator but passing the event selection (shower events), we have $M = M_1 + M_2$.

The measured muon flux ϕ can be calculated as

$$\phi = \frac{R_\mu}{S_{\text{box}}} = \frac{R_{\text{trig}}/\epsilon}{\sum_{i=1}^5 S_i} \equiv \frac{R_{\text{trig}}}{S_{\text{eff}}} \quad (6-38)$$

where R_μ is the muon rate of the box cover, S_{box} is the projection area of the 8 m×6 m×5 m box cover, R_{trig} is the rate of muon candidates passing the event selection that is going to be discussed in Sec. 6.3 from the data, $S_{\text{eff}} \equiv \epsilon \sum_{i=1}^5 S_i$ is defined as the effective cross-section. The simulation result showed that $\epsilon = 1.70\%$, $\epsilon_g = 2.02\%$, $\epsilon_d = 82.7\%$, $\epsilon_s = 0.04\%$, $S_{\text{box}} = 78.7 \text{ m}^2$, $S_{\text{eff}} = 1.34 \text{ m}^2$. The effective cross-section S_{eff} is close to the cross-section of the liquid scintillator sphere, which is 1.31 m^2 .

The geometry factor ϵ_g is small because the experimental hall is much larger than the detector and ϵ_g can be estimated analytically by

$$\epsilon_g \sim \frac{\pi r^2}{WL} = \frac{\pi \times 0.645^2}{8 \times 6} = 2.7\% \quad (6-39)$$

which has the same order of magnitude with the simulation result.

6.3 Event selection

The data set is from Run 257 to Run 1706, before installing the nitrogen system. The LS properties are very different after nitrogen injection. We observed a larger light yield and a longer time constant. The data after nitrogen injection need to be analyzed carefully in the future. A list of all cuts for event selection is shown in Table 6.1. These quantities are divided into two parts: data quality check and muon candidates selection.

Table 6.1 Summary of cuts for muon candidates selection.

Type	Cut
Data quality check	Good run Trigger rate, baseline and baseline fluctuation
Muon candidates selection	Number of photoelectrons > 6000 $r_{\text{max}} < 0.15$

We first required that runs should be flagged as good runs, i.e., neither pedestal calibration nor detector maintenance. Data quality check parameters for identifying apparent noise were the trigger rate, baseline, and baseline fluctuation of a waveform. A data file should not have these quantities deviated from the reference values by three standard de-

viations.

We then required a minimum number of photoelectrons (PEs), corresponding to approximately 100 MeV energy deposits or 50 cm track length in the scintillator. When passing through the detector’s edge, a muon deposits less energy, which became indistinguishable with that from the radioactive background, shower muon, or noise events. Therefore, this cut discarded low-energy events to get a high purity sample.

We finally removed the flasher events, which were highly-charged light-emitting events, possibly from PMT bases’ discharging. Examining all the high energy deposit events’ waveforms, we found that some of them always had a single PMT with a much higher charge than the others, while a muon event was of a more uniform charge distribution. We defined a ratio of maximum PE number to total PE number in one event, notated as r_{\max} , should not be greater than 0.15 to identify the flasher events.

Event display examples of muon candidates, flasher events, and electronics noise events are shown in Figure 6.10, 6.11, and 6.12.

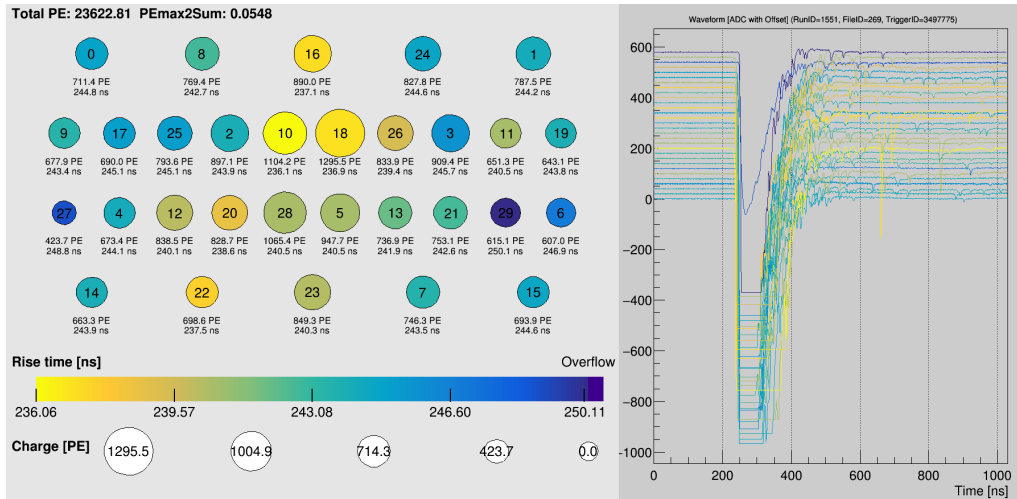


Figure 6.10 An example of muon candidates.

Figure 6.13 shows a two-dimensional distribution and one-dimensional projections of PE number and r_{\max} , indicating that the flasher events and the electronic noise events correspond to the clusters with larger r_{\max} . We also plotted the simulation result and one-dimensional projections for better comparison. In the end, 264 muon candidates passed the selection criteria.

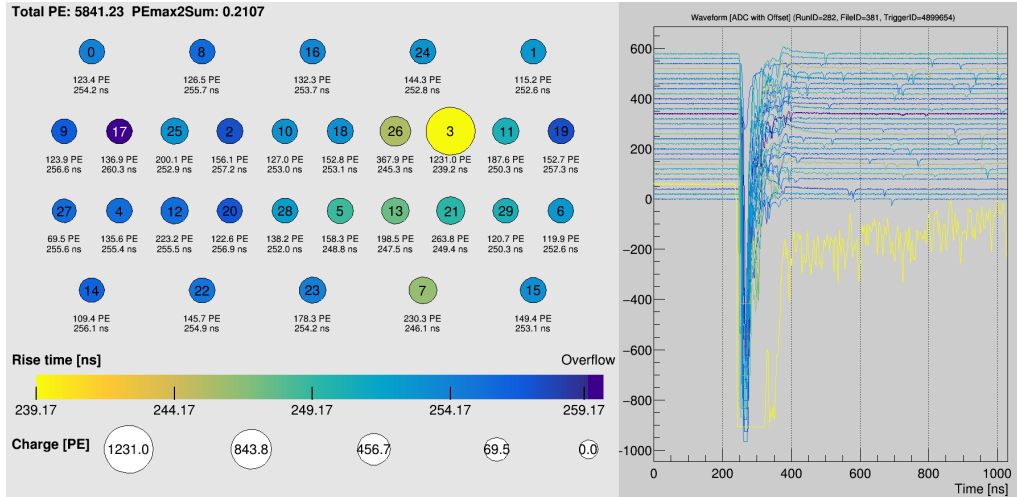


Figure 6.11 An example of flasher events.

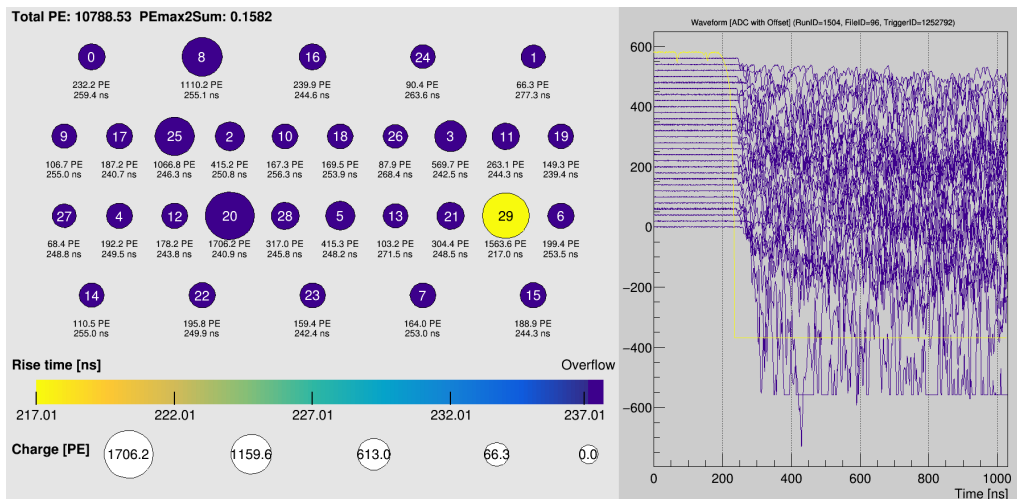


Figure 6.12 An example of electronics events.

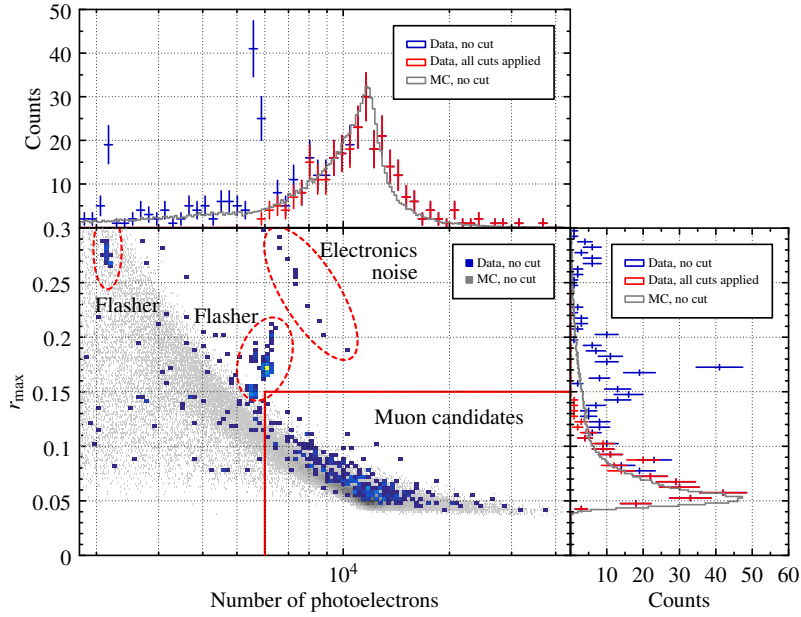


Figure 6.13 The scattered plot and one-dimensional projections of r_{\max} and PE number distribution from the data. The grey area in the two-dimensional distribution is the simulation result. The peak larger than 0.15 in the r_{\max} distribution represents flasher events.

6.4 Direction reconstruction

We used a template-based method to do the reconstruction. Each template was tagged with the muon direction $\mathbf{p}_i = (\cos \theta, \phi)$ and the entry point on the acrylic vessel $(\cos \alpha, \beta)$, as shown in Figure 6.14. When a muon's direction sampled from a uniform distribution, its entry point on the vessel surface was also sampled uniformly on the hemisphere facing the muon direction.

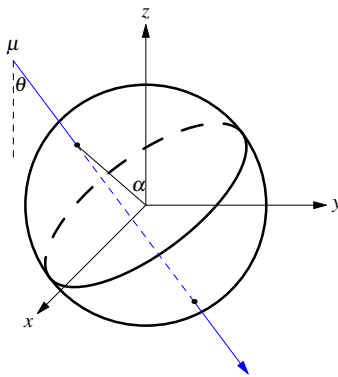


Figure 6.14 Muon generator in the PMT trigger time pattern template. The muon direction $(\cos \theta, \phi)$ and entry point $(\cos \alpha, \beta)$ were sampled uniformly.

About 250k template events passed the event selection criteria described in Section 6.3. We subtracted the mean value $\frac{1}{30} \sum_{j=0}^{29} t_{ji}$ from the PMT arrival time pattern vector of template i : $\mathbf{T}_i = (t_{0i}, t_{1i}, \dots, t_{29i})$ for zero centering. For the data vector

$\mathbf{T} = (t_0, t_1, \dots, t_{29})$, we searched for the k nearest neighbors with the Euclidean distance,

$$d_i = |\mathbf{T}_i - \mathbf{T}| = \sqrt{\sum_{j=0}^{29} (t_{ji} - t_j)^2} \quad (6-40)$$

The hyper-parameter k is an arbitrary integer to be chosen later. Then the reconstruction muon direction \mathbf{P} was calculated by the weighted average of the k nearest neighbors,

$$\mathbf{P} = \frac{\sum_{i=1}^k \frac{1}{d_i} \mathbf{p}_i}{\sum_{i=1}^k \frac{1}{d_i}} \quad (6-41)$$

We generated a test sample (also uniform muons) to evaluate the reconstruction method's performance and determined the hyper-parameter k . The smearing induced by the detector response was added in the test sample to simulate the uncertainty induced by the electronic hardware and the time calibration. Figure 6.15 shows that the average included angle between the truth and the reconstructed directions $\Delta\Theta$ varies with the hyper-parameter k and becomes stable at $k = 50$ and above. Therefore, we chose $k = 50$ for the reconstruction. Figure 6.16 shows the included angle's distribution with a peak value of 10 degrees and a average of 32 degrees. The long tail was due to the limited time resolution of electronic hardware and PMTs.

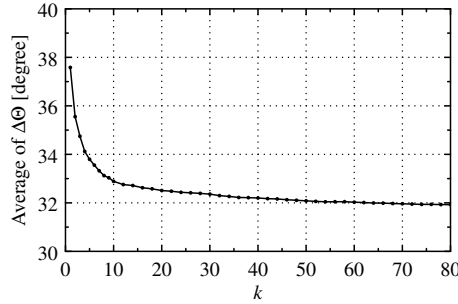


Figure 6.15 The average included angle $\Delta\Theta$ between the truth and reconstructed directions varies with the hyper-parameter k .

Figure 6.17 shows the $\cos\theta$ and ϕ distributions for both the data and the simulation. Both were consistent. The uneven structure observed the ϕ distribution indicates the different cosmic-ray leakage due to the mountain structure above CJPL-I.

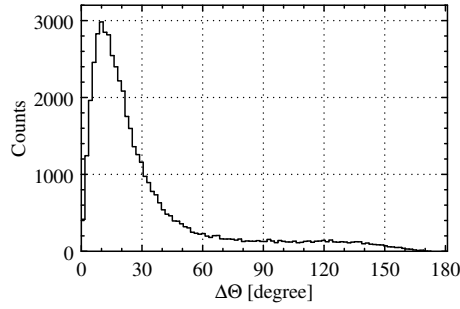


Figure 6.16 The included angle $\Delta\Theta$ between the truth and the reconstructed directions for $k = 50$.

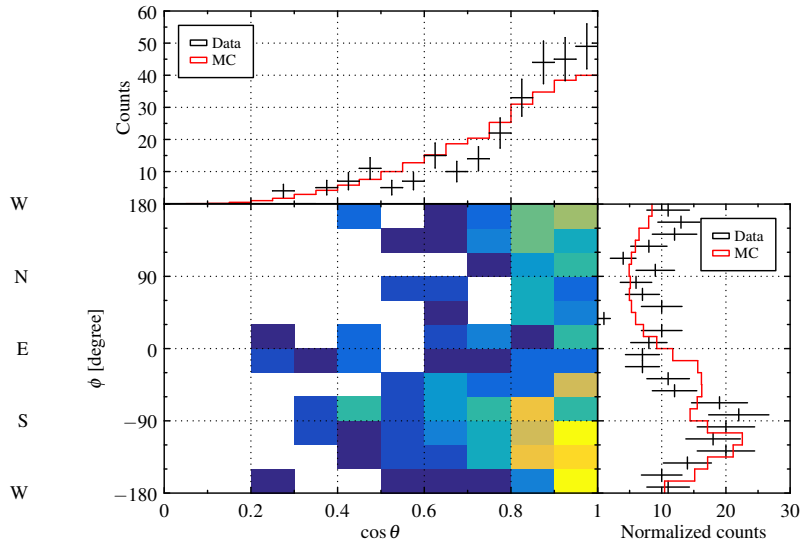


Figure 6.17 The reconstructed $\cos \theta$ and ϕ for the selected muon candidates. Also plotted are the marginal distributions for these two angles for the data (black) and the simulation (red).

6.5 Flux and angular distribution result

The measured muon flux ϕ was calculated by

$$f_{\mu} = \frac{N_{\mu}}{T S_{\text{eff}}} \quad (6-42)$$

where N_{μ} is the number of muon candidates, T is the live time, S_{eff} is the effective area.

6.5.1 Live time

The data included in this analysis were collected from July 31, 2017, to July 12, 2019. Each normal run lasted about one day. Only the goods run files were analyzed. The total live time of the data set is $T = 5.575 \times 10^7$ s, or 645.2 days.

6.5.2 Uncertainties

Table 6.2 summarizes the systematic uncertainties, which mainly come from two parts: (1) the PE number calculation in the data and (2) the active area calculation in the Monte-Carlo simulation. A quadrature sum of the individual components gives the total systematic uncertainty.

Table 6.2 Summary of uncertainties for the muon flux measurement.

Source	Parameter uncertainty	Flux measurement uncertainty
PMT gain calibration	$\pm 2.0\%$	$\pm 0.6\%$
PE yield	$\pm 1.6\%$	$\pm 0.5\%$
Acrylic vessel radius	± 5 mm	$\pm 1.6\%$
Lead shielding depth	± 5 cm	$\pm 0.6\%^*$
Rock depth	± 0.5 m	$\pm 0.8\%^*$
Muon spectrum	-	$\pm 0.7\%^*$
Total systematic	-	$\pm 2.1\%$
Statistics	-	$\pm 6.2\%$

* Dominant by the statistics uncertainty of Monte-Carlo.

The conversion from the charge to the number of PEs was through a PMT gain factor. A run-by-run PMT calibration corrected the gain drift and introduced a 2.0% systematic uncertainty, corresponding to a 0.6% efficiency variation for the 6000 PE cut.

The uncertainty of active area calculation came from the parameters in the simulation's input. We compared the data and simulation's PE distribution and tuned the scintillation light yield to ensure consistency between the data and simulation. The evaluation of systematic uncertainty for the level of consistency was from studying the Person's χ^2 as given below,

$$\chi^2 = \sum_{\text{each bin}} \frac{(n_{\text{data}} - n_{\text{sim}})^2}{n_{\text{data}}} \quad (6-43)$$

The systematic uncertainty of PE yield in the simulation took the variation at $\chi_{\text{min}}^2 + 1$.

Two hemispheres glued the acrylic vessel filled with the slow liquid scintillator, and the machining accuracy was 5 mm, contributing a 1.6% systematic uncertainty for the active area.

The muon shower in the rock and lead shielding also contributed to the active area. We placed 1 m depth of rock in the simulation. To verify whether the depth is enough, we

added/subtracted 0.5 m rock in different simulations to observe the variation and found that the active area was not sensitive to rock depth. Since the lead wall thickness was not even due to the different lead brick arrangement. We changed the thickness by ± 5 cm, a typical size of a lead brick, in the simulations, and found little variation in the active area. Limited by the statistical uncertainty of Monte-Carlo, the above studies gave 0.6% and 0.8% systematic uncertainty for the muon shower effect.

The muon spectrum could affect the active area slightly. We scanned different muon spectra in Section 6.1. Thanks to the detector's spherical symmetry, the muon spectrum's uncertainty was also small and dominated by the statistical uncertainty of Monte-Carlo.

6.5.3 Muon flux measurement result

A total of 264 muon candidates passing all selection cuts are reconstructed for the 645.2-day dataset. The average muon candidate rate of each month is shown in Figure 6.18. Figure 6.18 shows an even distribution for the monthly average muon candidate rate, as expected. The total measured cosmic-ray muon flux was $(3.53 \pm 0.22(\text{stat.}) \pm 0.07(\text{sys.})) \times 10^{-10} \text{ cm}^{-2} \text{ s}^{-1}$. The vertical intensity in $0.95 < \cos \theta < 1$ was $(2.09 \pm 0.30) \times 10^{-10} \text{ cm}^{-2} \text{ s}^{-1} \text{ sr}^{-1}$, in agreement with the previous measurement^[38].

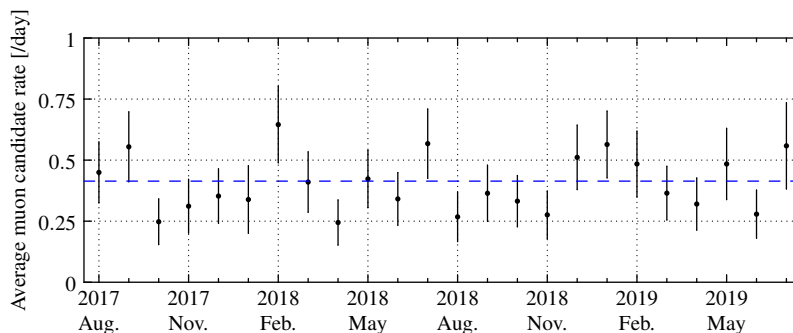


Figure 6.18 Cosmic-ray muon rate measured by the 1-ton prototype at CJPL-I, as a function of time. The data are shown in monthly bins.

Figure 6.19(a) shows the vertical intensity of muons at WIPP^[105], Soudan^[106], Boulby^[107], Sudbury^[108], Kamioka^[109], Gran Sasso^[110], Fréjus^[111], and Jinping as a function of vertical overburden. Also plotted is the prediction by a parametrized formula, given by Ref.^[112],

$$I(h) = I_1 e^{-h/\lambda_1} + I_2 e^{-h/\lambda_2} \quad (6-44)$$

where $I(h)$ is the differential muon intensity corresponding to the slant depth h ,

$I_1, I_2, \lambda_1, \lambda_2$ are parameters in Ref. [112]. The measurement result in this work is consistent with Eq. (6-44).

Figure 6.19(b) summarized the total muon flux measured at different underground sites. WIPP, Soudan, Boulby, and Sudbury are the labs situated down mine shafts, while Kamioka, Gran Sasso, Fréjus, and Jinping are below mountains. We also simulated the muon flux at different depths for the laboratories down mine shafts by Geant4. The simulation result is consistent with the data.

The total muon flux of a lab situated below a mountain can be treated as a multiplier times the down mine shaft case with the same vertical depth because the mountain case has less rock shielding. The multipliers are 3.7 (Kamioka), 5.2 (Gran Sasso), 3.9 (Fréjus) and 2.9 (Jinping). We assumed that the mountains on the Earth have similar structure so that the multipliers would not vary too much. We fitted the four mountain overburden labs (blued dashed line in Figure 6.19(b)) and the overall multiplier was (4.0 ± 1.9) .

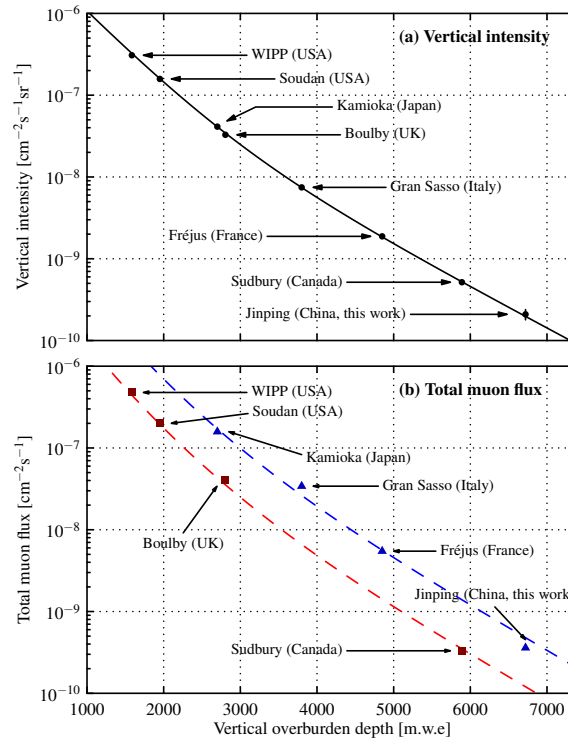


Figure 6.19 Measurements of the vertical intensity (a) and total muon flux (b) at different underground sites. The red dashed line in (b) is the simulation result for flat overburden case. The blue dashed line in (b) is the fit for the overall multiplier.

6.6 Summary

We used a simulation model to estimate the underground muon kinetic energy and angular distribution. Besides muon flux, the direction reconstruction gave the measurement of underground muon angular distribution. Comparing with the previous measurement^[38] and simulation of muon penetration in the mountains, we found that non-vertically going muons also play a role in the total muon flux at a mountain overburden underground laboratory. This study provides a reference for the site selection of neutrino experiments.

Chapter 7 Conclusions and Outlook

7.1 Conclusions

Neutrinos are unique probes to study the interior of the Sun and the Earth, connecting key issues of particle physics, geophysics, astrophysics, and cosmology. This thesis focuses on the R&D study on the MeV-scale neutrino experiment, a challenge in providing both direction and energy measurements. Slow liquid scintillator has demonstrated a longer fluorescent emission time, giving prominence to the small prompt Čerenkov light component with directional information of charged particle. It can thus provide extra capacities to reconstruct the particle direction, identify different particles, and suppress the background. Four primary studies in this thesis are as follows: (1) measure properties of LAB based slow liquid scintillator, (2) develop a general simulation package, (3) construct the 1-ton prototype neutrino detector based on the slow liquid scintillator, and (4) use the detector to measure the muon flux at CJPLI.

The cocktails of LAB with PPO and bis-MSB solvents are potential slow liquid scintillator candidates. Although the high concentration solutions (up to 3 g/L PPO and 15 mg/L bis-MSB) have been widely applied in neutrino experiments, the low concentration solutions (down to ~ 10 mg/L PPO) show very different properties, which can be useful for specific purposes. Low concentration of PPO and bis-MSB in LAB cannot only serve as a wavelength shifter to reduce the absorption and re-emission of short wavelength Čerenkov light but also can tune the decay time constant for fluorescent light from 10 ns to 100 ns level. Therefore, the prompt Čerenkov signal can be identified from the potential scintillation light by the pulse-shape analysis. The inverse relationship between the decay time constant and the light yield enables us to find a balance between the direction and energy resolutions. We can generalize this model to other cocktails with similar fluorescence mechanism. Other properties such as attenuation length and emission spectrum are also important parameters for the large scale detector design in the future.

The simulation package is essential for the detector design and optimization. The geometry definition is flexible so that the simulation code can accommodate to different scale detectors. The generator and streamed trigger system dynamically emulate the radioactive background and electronics trigger mechanisms. Now the package has been applied for the R&D study of the neutrino experiment in CJPL, including detector effi-

ciency estimation in ^{214}Bi contamination and muon flux measurement; background level study of kiloton scale detector; reconstruction algorithm study of 1-ton prototype and kiloton scale detector.

Although the 1-ton prototype is small and compact, it has most components in a large scale neutrino detector and provides experience for building kiloton detectors in the future. It has been running for three years until now. After several updates and maintenance, we have a better understanding of the detector.

We built a Monte-Carlo model to simulate the muon transportation in the mountain rocks. From a 700-day dataset, we measured the total muon flux at CJPL-I to be $(3.55 \pm 0.20(\text{stat.})_{-0.25}^{+0.17}(\text{sys.})) \times 10^{-10} \text{ cm}^{-2}\text{s}^{-1}$. This result is very close to the one in the SNO lab. By reconstructing the angular distribution and utilizing satellite images to model the mountain terrain, we identified the main direction of cosmic ray leakage at CJPL-I. The measurement results are consistent with the simulation results. We also compared underground laboratories below mountains and down mine shafts in terms of cosmic-ray shielding. This study helps to design the active and passive shielding of cosmic-ray background for low background neutrino experiments.

7.2 Outlook

LAB is one of the liquid scintillators widely used in neutrino experiments. Slow liquid scintillators with other formulas are also worth exploring. The re-emission and attenuation properties need to be measured and modeled further. In a small detector such as the 20 L detector, or the 1-ton prototype, the two-components model of attenuation length can well describe the attenuation behavior. However, a large scale neutrino detector does need a more precise measurement on the optical properties, since the re-emission and attenuation can also affect the Čerenkov light yield, which is vital to the direction reconstruction.

The vertex reconstruction and particle identification algorithms are still under study. We anticipate a perfect method to reconstruct the position, energy, and direction simultaneously, especially for low-energy events. Particle identification is another application of the slow liquid scintillator. The pattern recognition of Čerenkov photoelectrons is a critical issue. The techniques in computer vision, such as spherical CNNs (Convolutional Neural Networks), may provide a new perspective. In a large scale detector with a resolution of 500 PE/MeV, the separation of several Čerenkov photoelectrons in the first tens

of photoelectrons registered in the PMTs is a challenge, but is more feasible than that in a conventional liquid scintillator detector.

We expect many other physical analyses in the 1-ton prototype, including the search of fast neutrons, ^{212}Bi decay signals, Čerenkov light. The ^{214}Bi cascade decay events are an excellent sample to search Čerenkov light because the energy of prompted electron signal exceeds the Čerenkov threshold, while the delayed alpha signal does not. The comparison between alpha and beta signals can show the evidence of Čerenkov light. This analysis needs a precise time resolution of the first several photoelectrons. We are looking forwards to the improvement in the subsequent analysis.

Reference

- [1] Amaldi E. From the discovery of the neutron to the discovery of nuclear fission[J]. Phys. Rept., 1984, 111:1-332.
- [2] Aguilar-Arevalo A A, et al. Evidence for neutrino oscillations from the observation of $\bar{\nu}_e$ appearance in a $\bar{\nu}_\mu$ beam[J]. Phys. Rev., 2001, D64:112007.
- [3] Aguilar-Arevalo A A, et al. A Search for Electron Neutrino Appearance at the $\Delta m^2 \sim 1 \text{ eV}^2$ Scale[J]. Phys. Rev. Lett., 2007, 98:231801.
- [4] Aguilar-Arevalo A A, et al. Event Excess in the MiniBooNE Search for $\bar{\nu}_\mu \rightarrow \bar{\nu}_e$ Oscillations [J]. Phys. Rev. Lett., 2010, 105:181801.
- [5] Tanabashi M, et al. Review of particle physics[J]. Phys. Rev. D, 2018, 98:030001.
- [6] An F P, et al. Measurement of electron antineutrino oscillation based on 1230 days of operation of the daya bay experiment[J]. Phys. Rev. D, 2017, 95:072006.
- [7] Abe K, et al. Evidence of electron neutrino appearance in a muon neutrino beam[J]. Phys. Rev. D, 2013, 88:032002.
- [8] Mikheyev S P, Smirnov A Yu. Resonance Amplification of Oscillations in Matter and Spectroscopy of Solar Neutrinos[J]. Sov. J. Nucl. Phys., 1985, 42:913-917.
- [9] Wolfenstein L. Neutrino oscillations in matter[J]. Phys. Rev. D, 1978, 17:2369-2374.
- [10] Langacker P, Leveille J P, Sheiman J. On the detection of cosmological neutrinos by coherent scattering[J]. Phys. Rev. D, 1983, 27:1228-1242.
- [11] Fertl M. Review of absolute neutrino mass measurements[J]. Hyperfine Interact., 2018, 239(1): 52.
- [12] Capozzi F, Di Valentino E, Lisi E, et al. Global constraints on absolute neutrino masses and their ordering[J]. Phys. Rev., 2017, D95(9):096014.
- [13] An F, et al. Neutrino physics with JUNO[J]. Journal of Physics G: Nuclear and Particle Physics, 2016, 43(3):030401.
- [14] Abe K, et al. Neutrino oscillation physics potential of the T2K experiment[J]. Progress of Theoretical and Experimental Physics, 2015, 2015(4).
- [15] Ternes C A, Gariazzo S, Hajjar R, et al. Neutrino mass ordering at dune: An extra ν bonus[J]. Phys. Rev. D, 2019, 100:093004.
- [16] Haxton W C, Hamish Robertson R, Serenelli A M. Solar neutrinos: status and prospects[J]. Annual Review of Astronomy and Astrophysics, 2013, 51:21-61.
- [17] Serenelli A M, Basu S, Ferguson J W, et al. New solar composition: The problem with solar models revisited[J]. The Astrophysical Journal, 2009, 705(2):123-127.
- [18] Serenelli A M, Haxton W C, Peña-Garay C. Solar models with accretion. i. application to the solar abundance problem[J]. The Astrophysical Journal, 2011, 743(1):24.
- [19] Serenelli A, Peña Garay C, Haxton W C. Using the standard solar model to constrain solar composition and nuclear reaction s factors[J]. Phys. Rev. D, 2013, 87:043001.

- [20] de Holanda P C, Smirnov A Y. Homestake result, sterile neutrinos, and low energy solar neutrino experiments[J]. *Phys. Rev. D*, 2004, 69:113002.
- [21] Bonventre R, LaTorre A, Klein J R, et al. Nonstandard models, solar neutrinos, and large θ_{13} [J]. *Phys. Rev. D*, 2013, 88:053010.
- [22] Friedland A, Lunardini C, Peña-Garay C. Solar neutrinos as probes of neutrino–matter interactions[J]. *Physics Letters B*, 2004, 594(3):347 - 354.
- [23] Maltoni M, Smirnov A Y. Solar neutrinos and neutrino physics[J]. *Eur. Phys. J. A*, 2016, 52 (87).
- [24] Davies J, Davies D R. Earth’s surface heat flux[J]. *Solid Earth*, 2010, 1:5-24.
- [25] Šrámek O, et al. Geophysical and geochemical constraints on geoneutrino fluxes from earth’s mantle[J]. *Earth and Planetary Science Letters*, 2013, 361:356 - 366.
- [26] Araki T, et al. Experimental investigation of geologically produced antineutrinos with kamland [J]. *Nature*, 2005, 436(7050):499-503.
- [27] Agostini M, et al. Spectroscopy of geoneutrinos from 2056 days of borexino data[J]. *Phys. Rev. D*, 2015, 92:031101.
- [28] Malek M, et al. Search for supernova relic neutrinos at super-kamiokande[J]. *Phys. Rev. Lett.*, 2003, 90:061101.
- [29] Bays K, et al. Supernova relic neutrino search at super-kamiokande[J]. *Phys. Rev. D*, 2012, 85: 052007.
- [30] Zhang H, et al. Supernova Relic Neutrino Search with Neutron Tagging at Super-Kamiokande-IV[J]. *Astropart. Phys.*, 2015, 60:41-46.
- [31] Gando A, othersi. Search for extraterrestrial antineutrino sources with the kamland detector [J/OL]. *The Astrophysical Journal*, 2012, 745(2):193. <https://doi.org/10.1088%2F0004-637x%2F745%2F2%2F193>.
- [32] Bellini G, et al. Study of solar and other unknown anti-neutrino fluxes with borexino at lngs[J]. *Physics Letters B*, 2011, 696(3):191 - 196.
- [33] Aharmim B, et al. A search for neutrinos from the SolarhepReaction and the diffuse supernova neutrino background with the sudbury neutrino observatory[J]. *The Astrophysical Journal*, 2006, 653(2):1545-1551.
- [34] Askins M, et al. Theia: An advanced optical neutrino detector[Z]. [S.l.: s.n.], 2019.
- [35] Bellini G, et al. Final results of borexino phase-i on low-energy solar neutrino spectroscopy[J]. *Phys. Rev. D*, 2014, 89:112007.
- [36] Cheng J, et al. The china jinping underground laboratory and its early science[J]. *Annual Review of Nuclear and Particle Science*, 2017, 67(1):231-251.
- [37] Beacom J F, et al. Physics prospects of the jinping neutrino experiment[J]. *Chinese physics C*, 2017, 41(2):023002.
- [38] Wu Y C, et al. Measurement of cosmic ray flux in the china JinPing underground laboratory[J]. *Chinese Physics C*, 2013, 37(8):086001.
- [39] Yue Q, et al. Limits on light weakly interacting massive particles from the cdex-1 experiment with a *p*-type point-contact germanium detector at the china jinping underground laboratory[J]. *Phys. Rev. D*, 2014, 90:091701.

- [40] Xiao M, et al. First dark matter search results from the pandax-i experiment[J]. *Science China Physics, Mechanics and Astronomy*, 2014, 57.
- [41] Wang Z, et al. Design and analysis of a 1-ton prototype of the jinping neutrino experiment[J]. *Nuclear Instruments and Methods in Physics Research Section A*, 2017, 855:81-87.
- [42] Kang K J, et al. Introduction to the CDEX experiment[J]. *Front. Phys.(Beijing)*, 2013, 8:412-437.
- [43] Duncan F, Noble A J, Sinclair D. The construction and anticipated science of SNOLAB[J]. *Ann. Rev. Nucl. Part. Sci.*, 2010, 60:163-180.
- [44] Arpesella C, et al. A Low background counting facility at Laboratori Nazionali del Gran Sasso [C]//*Applied Radiation and Isotopes: volume 47*. [S.l.: s.n.], 1996: 991-996.
- [45] Zhang C. Precision measurement of neutrino oscillation parameters and investigation of nuclear georeactor hypothesis with kamland[D]. the USA: California Institute of Technology, 2011.
- [46] International Atomic Energy Agency. Home page[EB/OL]. 2015. <http://www.iaea.org/>.
- [47] Parke S J. Nonadiabatic level crossing in resonant neutrino oscillations[J]. *Phys. Rev. Lett.*, 1986, 57:1275-1278.
- [48] Haxton W C. Adiabatic conversion of solar neutrinos[J]. *Phys. Rev. Lett.*, 1986, 57:1271-1274.
- [49] Bellini G, et al. Measurement of the solar ^8B neutrino rate with a liquid scintillator target and 3 mev energy threshold in the borexino detector[J]. *Phys. Rev. D*, 2010, 82:033006.
- [50] Abe K, et al. Solar neutrino results in super-kamiokande-iii[J]. *Phys. Rev. D*, 2011, 83:052010.
- [51] Aharmim B, et al. Combined analysis of all three phases of solar neutrino data from the sudbury neutrino observatory[J]. *Phys. Rev. C*, 2013, 88:025501.
- [52] Beacom J F. The diffuse supernova neutrino background[J]. *Annual Review of Nuclear and Particle Science*, 2010, 60(1):439-462.
- [53] Wei H, Wang Z, Chen S. Discovery potential for supernova relic neutrinos with slow liquid scintillator detectors[J]. *Physics Letters B*, 2017, 769:255-261.
- [54] Alonso J, et al. Advanced scintillator detector concept (asdc): A concept paper on the physics potential of water-based liquid scintillator[J]. *arXiv preprint arXiv:1409.5864*, 2014.
- [55] Yeh M, et al. A new water-based liquid scintillator and potential applications[J]. *Nucl. Instrum. Methods A*, 2011, 660(1):51 - 56.
- [56] Reeder R A, et al. Dilute scintillators for large volume tracking detectors[J]. *Nuclear Instruments and Methods in Physics Research A*, 1993, 353:353-366.
- [57] Caravaca J, et al. Experiment to demonstrate separation of cherenkov and scintillation signals [J]. *Phys. Rev. C*, 2017, 95:055801.
- [58] Guo Z, Yeh M, Zhang R, et al. Slow liquid scintillator candidates for mev-scale neutrino experiments[J]. *Astroparticle Physics*, 2019, 109:33 - 40.
- [59] Bonventre R, Orebi G G D. Sensitivity of a low threshold directional detector to cno-cycle solar neutrinos[J]. *European Physical Journal C*, 2018, 78(6):435-.
- [60] Wang Z, Chen S. Observing the Potassium Geoneutrinos with Liquid Scintillator Cherenkov Neutrino Detectors[J]. *Chin. Phys.*, 2020, C44(3):033001.
- [61] Aberle C, et al. Measuring directionality in double-beta decay and neutrino interactions with kiloton-scale scintillation detectors[J]. *JINST*, 2014, 9:P06012.

- [62] Fukuda Y. ZICOS - New project for neutrinoless double beta decay experiment using zirconium complex in liquid scintillator[J]. *J. Phys. Conf. Ser.*, 2016, 718(6):062019.
- [63] Elagin A, et al. Separating double-beta decay events from solar neutrino interactions in a kiloton-scale liquid scintillator detector by fast timing[J]. *Nucl. Instrum. Methods A*, 2017, 849:102-111.
- [64] Ciuffoli E, Evslin J, Zhao F. Neutrino physics with accelerator driven subcritical reactors[J]. *Journal of High Energy Physics*, 2016, 2016(1):4.
- [65] Ciuffoli E, Evslin J, Zhang X. The leptonic cp phase from muon decay at rest with two detectors [J]. *Journal of High Energy Physics*, 2014, 2014(12):51.
- [66] Wang Z, Chen S. Hunting potassium geoneutrinos with liquid scintillator cherenkov neutrino detectors[J]. *Chinese Physics C*, 2020, 44(3):033001.
- [67] Li M, et al. Separation of scintillation and cherenkov lights in linear alkyl benzene[J]. *Nucl. Instrum. Methods A*, 2016, 830:303-308.
- [68] Caravaca J, et al. Cherenkov and scintillation light separation in organic liquid scintillators[J]. arXiv preprint arXiv:1610.02011, 2016.
- [69] Adams B, et al. Measurements of the gain, time resolution, and spatial resolution of a 20×20 cm² mcp-based picosecond photo-detector[J]. *Nuclear Instruments and Methods in Physics Research A*, 2013, 732:392-C396.
- [70] Yeh M, Garnov A, Hahn R. Gadolinium-loaded liquid scintillator for high-precision measurements of antineutrino oscillations and the mixing angle, θ_{13} [J]. *Nuclear Instruments and Methods in Physics Research A*, 2007, 578(1):329 - 339.
- [71] Ding Y, et al. A new gadolinium-loaded liquid scintillator for reactor neutrino detection[J]. *Nuclear Instruments and Methods in Physics Research A*, 2008, 584(1):238 - 243.
- [72] Agostinelli S, et al. Geant4 - a simulation toolkit[J]. *Nucl. Instrum. Methods A*, 2003, 506(3): 250 - 303.
- [73] Allison J, et al. Geant4 developments and applications[J]. *IEEE Transactions on Nuclear Science*, 2006, 53(1):270-278.
- [74] 关梦云. 大亚湾反应堆中微子实验的本底研究和模型研制[博士学位论文]. 北京: 中国科学院高能物理研究所, 2006.
- [75] Birks J B. *The theory and practice of scintillation counting*[M]. [S.l.]: Pergamon, 1964.
- [76] Aberle C, Buck C, Hartmann F X, et al. Light output of double chooz scintillators for low energy electrons[J]. *Journal of Instrumentation*, 2011, 6(11):P11006-P11006.
- [77] Goett J, et al. Optical attenuation measurements in metal-loaded liquid scintillators with a long-pathlength photometer[J]. *Nuclear Instruments and Methods in Physics Research Section A: Accelerators, Spectrometers, Detectors and Associated Equipment*, 2011, 637:47.
- [78] Xiao H L, et al. Study of absorption and re-emission processes in a ternary liquid scintillation system[J]. *Chinese Physics C - CHIN PHYS C*, 2010, 34:1724-1728.
- [79] Tseung H W C, Tolich N. Ellipsometric measurements of the refractive indices of linear alkylbenzene and EJ-301 scintillators from 210 to 1000 nm[J/OL]. *Physica Scripta*, 2011, 84(3): 035701. <https://doi.org/10.1088%2F0031-8949%2F84%2F03%2F035701>.
- [80] O’Keeffe H M, O’Sullivan E, Chen M C. Scintillation decay time and pulse shape discrimination in oxygenated and deoxygenated solutions of linear alkylbenzene for the SNO+ experiment[J]. *Nucl. Instrum. Meth.*, 2011, A640:119-122.

- [81] Aberle C, Buck C, Hartmann F X, et al. Light yield and energy transfer in a new gd-loaded liquid scintillator[J]. *Chemical Physics Letters*, 2011, 516(4-6):257-262.
- [82] Marrodán U T, et al. Fluorescence decay-time constants in organic liquid scintillators[J]. *Review of Scientific Instruments*, 2009, 80(4):091302.
- [83] Aharmim B, et al. Measurement of the cosmic ray and neutrino-induced muon flux at the sudbury neutrino observatory[J]. *Physical Review D*, 2009, 80:012001.
- [84] Huang P, et al. Study of attenuation length of linear alkyl benzene as ls solvent[J]. *JINST*, 2010, 5:P08007.
- [85] Yu G Y, et al. Some new progress on the light absorption properties of linear alkyl benzene solvent[J]. *Chinese physics C*, 2016, 40(1):016002.
- [86] Hamamatsu Photonics. Home page[EB/OL]. 2019. <https://www.hamamatsu.com/>.
- [87] Zhou X, et al. Rayleigh scattering of linear alkylbenzene in large liquid scintillator detectors[J]. *Rev. Sci. Instrum.*, 2015, 86:073310.
- [88] Zhou X, et al. Spectroscopic study of light scattering in linear alkylbenzene for liquid scintillator neutrino detectors[J]. *Eur. Phys. J.*, 2015, C75:545.
- [89] Gao L, et al. Attenuation length measurements of a liquid scintillator with labview and reliability evaluation of the device[J]. *Chinese Physics C*, 2013, 37:076001.
- [90] Chen M C. The sno liquid scintillator project[J]. *Nuclear Physics B (Proceedings Supplements)*, 2005, 145(145):65-68.
- [91] Senix Corporation. Home page[EB/OL]. 2019. <http://senix.com/>.
- [92] CAEN Company. Caen v2718 product page[EB/OL]. 2019. <https://www.caen.it/products/v2718/>.
- [93] CAEN Company. Caen v1751 product page[EB/OL]. 2019. <https://www.caen.it/products/v1751/>.
- [94] CAEN Company. Caen v1495 product page[EB/OL]. 2019. <https://www.caen.it/products/v1495/>.
- [95] CAEN Company. Caendigitizer library[EB/OL]. 2019. <https://www.caen.it/products/caendigitizer-library/>.
- [96] Savitzky A, Golay M J E. Smoothing and differentiation of data by simplified least squares procedures.[J]. *Analytical Chemistry*, 1964, 36(8):1627-1639.
- [97] Bellamy E, et al. Absolute calibration and monitoring of a spectrometric channel using a photomultiplier[J]. *Nuclear Instruments and Methods in Physics Research Section A: Accelerators, Spectrometers, Detectors and Associated Equipment*, 1994, 339(3):468 - 476.
- [98] 钟玮丽. 大亚湾中心探测器模型和 ΔM_{31}^2 测量精度的研究[博士学位论文]. 北京: 中国科学院高能物理研究所, 2008.
- [99] 于泽源. 大亚湾中微子实验刻度重建及中微子丢失研究[博士学位论文]. 北京: 中国科学院大学, 2013.
- [100] 孟祥承, 杨长根, 王志民, 等. 光电倍增管的光电子幅度谱测试研究[J]. *核电子学与探测技术*, 2005, 25(6):594-600.
- [101] Farr T G, Rosen P A, Caro E, et al. The shuttle radar topography mission[J]. *Reviews of Geophysics*, 2007, 45.

- [102] Lide D R. Crc handbook of chemistry and physics: volume 97[M]. [S.l.]: CRC press, 2016.
- [103] Gaisser T K. Cosmic rays and particle physics[M]. [S.l.]: Cambridge University Press, 1990.
- [104] Cecchini S, Sioli M. Cosmic ray muon physics[C]/Non-accelerator particle astrophysics. Proceedings, 5th ICTP School, Trieste, Italy, June 29-July 10, 1998. [S.l.: s.n.], 1998: 201-217.
- [105] Esch E I, Bowles T, Hime A, et al. The cosmic ray muon flux at wipp[J]. Nuclear Instruments and Methods in Physics Research Section A, 2005, 538(1-3):516-525.
- [106] Kamat S. Extending the sensitivity to the detection of wimp dark matter with an improved understanding of the limiting neutron backgrounds[D]. [S.l.]: Case Western Reserve University, 2005.
- [107] Robinson M, Kudryavtsev V, Lüscher R, et al. Measurements of muon flux at 1070m vertical depth in the Boulby underground laboratory[J]. Nuclear Instruments and Methods in Physics Research Section A, 2003, 511(3):347-353.
- [108] Aharmim B, Ahmed S, Andersen T, et al. Measurement of the cosmic ray and neutrino-induced muon flux at the Sudbury Neutrino Observatory[J]. Physical Review D, 2009, 80(1):012001.
- [109] Eguchi K, Enomoto S, Furuno K, et al. First results from KamLAND: evidence for reactor antineutrino disappearance[J]. Physical Review Letters, 2003, 90(2):021802.
- [110] Bellini G, Benziger J, Bick D, et al. Cosmic-muon flux and annual modulation in Borexino at 3800 m water-equivalent depth[J]. Journal of Cosmology and Astroparticle Physics, 2012, 2012(05):015.
- [111] Berger C, et al. Experimental study of muon bundles observed in the Fréjus detector[J]. Phys. Rev. D, 1989, 40:2163-2171.
- [112] Mei D, Hime A. Muon-induced background study for underground laboratories[J]. Phys. Rev., 2006, D73:053004.

Acknowledgments

I wish to express my sincere appreciation to my supervisor Prof. Shaomin Chen (陈少敏), Assoc. Prof. Zhe Wang (王喆), and Assoc. Prof. Benda Xu (续本达). They guided me through each stage of my PhD study, introduced me to the field of neutrino physics, provided me a deep insight into the physical universe, and taught me the methodology of scientific researches. Their detailed and patient comments helped me accomplished my thesis.

I'm grateful to the enlightenments and suggestions from Prof. Yuanning Gao (高原宁), Assoc. Prof. Zhenwei Yang (杨振伟), Assoc. Prof. Xianglei Zhu (朱相雷), Assoc. Prof. Qian Liu (刘倩), Prof. Ming Qi (祁鸣) during my PhD life. I would also thank my friends in the Jinping Collaboration and the Center for High Energy Physics, Tsinghua University: Liupan An (安刘攀), Lars Bathe-Peters, Chen Chen (陈晨), Mouri Chouaki, Wei Dou (窦威), Chenxi Gu (辜晨曦), Lei Guo (郭磊), Jinjing Li (李进京), Xuesong Liu (刘雪淞), Xuwei Liu (刘学伟), Guang Luo (罗光), Wentai Luo (骆文泰), Zan Ren (任赞), Wenhui Shao (邵文辉), Linyan Wan (万林焱), Hanyu Wei (魏瀚宇), Jianqiang Wang (王剑桥), Mengzhen Wang (王梦臻), Yi Wang (王轶), Zihan Wang (王子涵), Yiyang Wu (武益阳), Ao Xu (许傲), Li Xu (许立), Tong Xu (徐彤), Weiran Xu (徐蔚然), Di Yang (杨迪), Yuzi Yang (杨玉梓), Aiqiang Zhang (张爱强), Ling Zhang (张凌), Rui Zhang (张瑞), Shunan Zhang (张舒楠), Yiming Zhang (张一鸣), Lin Zhao (赵林).

Finally, I feel like expressing my great respect and gratitude to my parents. Without their infinite understanding and selfless support, I could not make my achievement.

Declaration

本人郑重声明：所呈交的学位论文，是本人在导师指导下，独立进行研究工作所取得的成果。尽我所知，除文中已经注明引用的内容外，本学位论文的研究成果不包含任何他人享有著作权的内容。对本论文所涉及的研究工作做出贡献的其他个人和集体，均已在文中以明确方式标明。

签 名： 郭子溢 日 期： 2020年7月21日

Resume, Publications and Research Achievements

个人简历

1992年4月17日出生于天津市。

2010年9月考入清华大学工程物理系工程物理专业，2014年7月本科毕业并获得工学学士学位。

2014年9月免试进入清华大学工程物理系攻读物理学博士学位至今。

发表的学术论文

- [1] Z. Guo, et al. Slow liquid scintillator candidates for MeV-scale neutrino experiments. *Astroparticle Physics*, 2019, 109:33-40.
- [2] Z. Guo, Z. Wang, for the Jinping Neutrino Experiment research group, Slow Liquid Scintillator for Scintillation and Cherenkov Light Separation, *Proceedings of International Conference on Technology and Instrumentation in Particle Physics 2017, Springer Proceedings in Physics*, 2018, 213:173-177.
- [3] M. Li, Z. Guo, et al. Separation of scintillation and Cherenkov lights in linear alkyl benzene. *Nuclear Instruments and Methods in Physics Research A*, 2016, 830:303-308.
- [4] Z. Wang, Y. Wang, Z. Wang, S. Chen, X. Du, T. Zhang, Z. Guo, H. Yuan, Design and analysis of a 1-ton prototype of the Jinping Neutrino Experiment, *Nuclear Instruments and Methods in Physics Research A*, 2017, 855:81-87.
- [5] G. Hussain, Z. Zeng, C. Yao, M. Li, Z. Guo, L. G. Z. Wang, S. Chen, Assay of low-background stainless steel by smelting for the neutrino experiment at Jinping, *Nuclear Instruments and Methods in Physics Research A*, 2018, 881:65-71.